THE UNIVERSITY OF CHICAGO

COLLOIDAL MERCURY CHALCOGENIDE QUANTUM DOTS, INTRABAND TRANSITIONS AND INFRARED DETECTION

A DISSERTATION SUBMITTED TO

THE FACULTY OF THE DIVISION OF THE PHYSICAL SCIENCES

IN CANDIDACY FOR THE DEGREE OF

DOCTOR OF PHILOSOPHY

DEPARTMENT OF CHEMISTRY

BY

ZHIYOU DENG

CHICAGO, ILLINOIS

MARCH 2017

I dedicate this thesis to my beloved parents and sisters.

Table of Contents

List of Figures

List of Abbreviations

ATR	attenuated total reflection
CQD	colloidal quantum dot
DDAB	didodecyldimethylammonium bromide
ddt	dodecanethiol
FTIR	Fourier transform infrared spectroscopy
HDA	hexadecylamine
HDT	hexanedithiol
IR	infrared
FWHM	full-width at half maximum
LWIR	long-wave infrared (8-12 μm wavelengths)
MCT	mercury cadmium telluride
MWIR	mid-wave infrared (3-5 μm wavelengths)
NHE	normal hydrogen electrode
NIR	near infrared
OAm	oleylamine
O.D.	optical density
ODA	octadecylamine
ODE	octadecene
QCL	quantum cascade laser
QDIP	quantum dot infrared photodetectors

QWIP	quantum well infrared photodetectors
SILAR	successive ion layer adhesion and reaction
SWIR	short-wave infrared (< 2.5 μm wavelengths)
T2SL	type II strained superlattices
TCE	tetrachloroethylene
TEM	transmission electron microscopy
$(TMS)_2S$	bis(trimethylsilyl) sulfide
TOP	tri-n-octylphosphine
TOPO	tri-n-octylphosphine oxide
XPS	x-ray photoelectron spectroscopy
XRD	x-ray diffraction

Acknowledgements

Looking back at my years in the PGS lab while writing my thesis, I am very grateful to Professor Philippe Guyot-Sionnest for his guide and help. I am glad that I could participate and contribute to the study of intraband transitions, which started 18 years ago. During this process, I have learned a lot from Philippe. He is the first person in the lab who showed me how to synthesize quantum dots. More importantly, it is his personality and his way of thinking that influence me the most. Everyone in the Chemistry Department (and probably Physics as well) knows Philippe is a very hardworking person, but not everyone has the opportunity to see how he really loves what he does. It is a great honor for me to work with such a passionate scientist. It is not uncommon that I am amazed at his insight into complex problems and his approach to them with clear logic and fundamental knowledge of physics and chemistry.

The PGS lab has made many pioneering and impactful contributions to the field of quantum dots. I think most people working in the lab are proud of that; I know I am when I see how other researchers praise the work in our lab when I attend academic meetings. By the way, Philippe is good at making great discoveries at low cost, as some grant reviewer once said "The PGS lab gets you the best bang for your buck", per our colleague EW. So, I think someday our lab will make IR photodetectors at low cost as well, which may be just around the corner.

I also want to express my great gratitude to the support from the faculty in the Department, especially Professor Talapin and Professor Engel on my defense committee. My conversations with them are always inspiring for me and sometimes make me think from a new perspective about my research. Professor Tian also helps me a lot during my time here.

I am thankful to all the members of the lab for their help: Sean Keuleyan, Kwang Jeong, EW Malachosky, Heng Liu, Wei Qin, Guohua Shen, Matt Ackerman, and Menglu Chen. Especially Sean and Kwang, they had been taught me a lot of experimental skills. I am also thankful to Hao Zhang, Yuanyuan Wang, and Igor Fedin in the Talapin group. The many discussions with them about inorganic ligand exchange and general quantum dot research are very informative and helpful.

Of course, I am grateful for the support from my family and friends, without whose support life would be much harder. It is with their encouragement and unending love that I overcame many difficulties and challenges in the past six years at here. They made who I am today. Thanks.

Abstract

After more than 30 years of research on colloidal quantum dots (CQDs), interband transitions have been extensively studied, while intraband transitions— excitations between energy levels within the same band — are underexplored and have not found any application yet. However, intraband transitions have a huge advantage in the application in infrared region (low energy): because the intraband transitions are not limited to narrow bandgap materials, more semiconductor and semimetal materials become potential candidates for infrared application.

In this thesis, I will report our progress in i) the synthesis of HgS, HgSe, and HgSe/CdS core/shell CQDs; ii) their optical and electronic properties and their sensitivity to the CQD surface; and iii) intraband transitions and infrared photodetection with them.

For the first time, we have successfully achieved intraband infrared photodetection in the mid-infrared region (between 3-5 microns), using intraband transitions of air-stable n-doped HgS and HgSe CQDs. Precise control of the doping level is essential to minimize the noise current and to increase the device performance. We also found that the doping level can be influenced by changing the surface condition of the CQDs and the surface gating could be used as a new method to tune the doping level of CQDs. To reduce nonradiative relaxation and improve thermal stability, we also made HgSe/CdS CQDs and studied the shell's effect on the property of the HgSe QDs. It is demonstrated that the shell could enhance the intraband PL and protect the core QDs during annealing process at 200 C°.

Chapter 1 Introduction

Five important senses help we human beings survive and develop on the planet: sight, hearing, taste, smell, and touch. It is with these functions that we are able to sense the environment around us and to grow knowledge after we synthesize all the information we get. As a result, the limitation of our senses defines the natural boundary of human capability to extract information about the physical world.

Our sight ability had always been limited to the visible light until the discovery of the infrared (IR) by William Herschel in 1800,[1-2] and since then we started to investigate steadily and deeply into the infrared and to pursue ways to see it, which is beyond the natural limit of our human eyes. After more than 200 years of efforts, we have achieved abundant knowledge about infrared and developed various infrared detectors.

As the name suggests, infrared is electromagnetic radiation with longer wavelengths than the red edge of the visible spectrum at 700 nanometers. The infrared spectrum is usually divided into several sections based on the wavelength, and the following is a typical division: near-IR (800 nm to 2.5 μm), mid-IR (2.5 μm to 20 μm), and the far-IR (above 20 μm, including THz).[3] In the mid-IR range, there are two transparency windows of the atmosphere (Figure 1-1), 3–5 μm and 8–12 μm, which avoid the absorption of the earth's atmosphere, mostly from of CO_2 and H_2O. These two bands are called mid-wave IR (MWIR) and long-wave IR (LWIR), respectively, and they are the targeting ranges for infrared thermal imaging.[4]

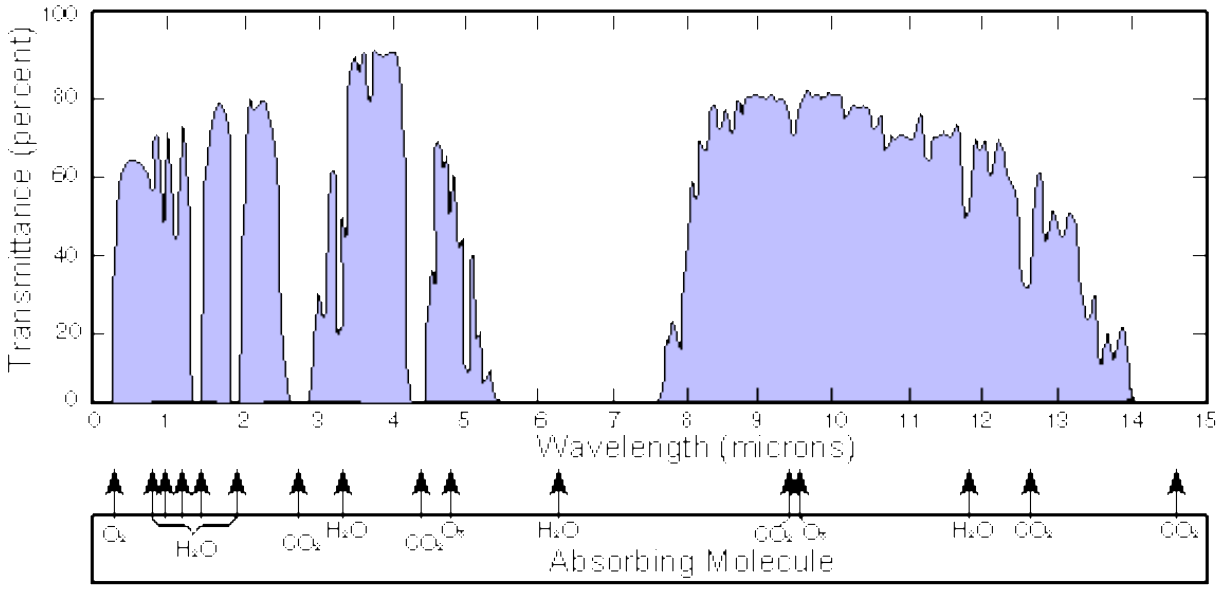

Figure 1-1 Atmospheric transmittance in part of the infrared region.

1.1 Infrared Applications and Technologies

Most of the IR detectors could be classified in two major types of infrared technology according to the principle it works: thermal detectors and photon detectors.[2] Thermal detector works when it absorbs incident radiation and its temperature changes, resulting further in some physical property changes, which is used to generate an electrical output. The signal does not depend upon the photonic nature of the incident radiation, since thermal effects are wavelength independent. Thermal detectors generally suffer from slow response and low detectivity, limiting their use in non-critical applications. However, sophisticated applications in civilian or military applications (e.g. self-driving vehicles and heat-seeking missiles) require better performance: faster response and higher sensitivity, which can only be provided by photon detectors, or photodetectors.

In photon detectors the radiation is absorbed within the material by interaction with electrons.[2] As the electronic energy distribution changes, electrical output signal is measured. So, the photon

detectors show a selective wavelength dependence of response per unit incident radiation power and they generally have a very fast response.

1.1.1 MCT: The Dominant IR Photodetector

The current leading IR photodetector is HgCdTe, also known as MCT for mercury cadmium telluride, which has been the dominant IR technology in the past 50 years.[5] This ternary alloy has an energy bandgap that can be tailored over the 1–30 μm range, covering the mid-IR, therefore it can be optimized for both MWIR and LWIR. Its bandgap is tuned by changing its composition, roughly linear between CdTe and HgTe, whose bandgaps are 1.5 eV and -0.3 eV, respectively.[6] MCT also has a large optical coefficient that enables high quantum efficiency. However, it has many drawbacks, including high cost and requirement of cooling among others. The fabrication is expensive because the growing process usually requires an exactly lattice-matched CdZnTe substrate and epitaxial growth. In addition, at high Hg compositions for long wavelengths, uniformity becomes an issue due to the weak bond between Hg and Te, which makes the lithography more difficult.

Therefore, even though MCT-based imaging chips could provide high quality imaging devices with megapixel cameras, their use is limited to high end military, astronomy or scientific applications due to high costs, typically in excess of $50,000 for a full imaging system. Alternative IR technologies have been actively investigated in the past 50 years.

1.1.2 Alternative IR Technologies

Quantum engineering of intraband transitions with epitaxially grown wide bandgap materials has successfully developed alternative IR technologies. One example is quantum-well infrared photodetector (QWIP), which uses intersubband (or intraband) optical transitions in quantum wells

as the photodetection mechanism.[7] QWIPs are made of a stack of thin doped semiconductor layers, a few nanometers thick, with different chemical compositions (e.g. GaAs/AlGaAs).[8] They are designed in a way that an excitation of an electron (hole) from the ground state in the conduction (valence) band to the first excited state in the same band which is close to the top of barrier. Therefore, when a voltage bias is applied across the detector, photoelectron could escape the well and be collected, generating a photocurrent through the detector. In 1987, Levine *et al* [9] demonstrated the first QWIP based on intersubband absorption between two bound quantum-well states and achieved a large peak responsivity of R=0.52 A/W at 10.8 um. With respect to MCT detectors, GaAs/AlGaAs QWIPs have many advantages: excellent uniformity over large surfaces, high yield and low cost because of the use of standard manufacturing techniques based on mature GaAs growth and processing technologies. These great advantages attract researchers to put significant efforts on the QWIP development and commercialization, making it a strong competitor against MCT, especially in the LWIR detection market. However, QWIPs still suffers from lower quantum efficiency and requires lower operating temperature (~70K).

An extension of the QWIP research leads to quantum-dot infrared photodetector (QDIP), which also uses intersubband transitions and operates in a similar mechanism. In a QDIP, quantum dot is used and the carriers are confined in all three dimensions (3D), instead of only in 1D in the case of QW. In theory, QDIPs could outperform QWIPs because of their inherent sensitivity to normal incidence radiation and reduced phonon scattering due to larger energy separations.[10-11] In 1988, Pan et al developed the first QDIP.[12] Thereafter, significant progress has been made on QDIPs, but they still have problems of low quantum efficiency due to the small area fill factor of QDs and the limited number of QD layers. In addition, the large non-uniformity and broadening of the self-

assembled QDs reduces the peak optical absorption and increase dark current, making it difficult to achieve the theoretically predicted performance.

Type II strained superlattice (T2SL) is another alternative technology. T2SL is a system of repeating sequence of thin layers of different materials such as InAs/GaSb with a type-II band alignment[13] that employs the optical transition between electron and hole minibands in the conduction and valence band, respectively, which are formed due to the overlap of electron (hole) wave functions between adjacent InAs (GaSb) layers. Its operating wavelength can be tuned from 3 μm to 32 μm by varying thickness of one or two T2SL constituent layers.[14-15] Because the electrons and holes are confined to two different layers, it is supposed to suppresses Auger recombination mechanisms and thereby enhance carrier lifetime, and increase operating temperatures in comparison to HgCdTe. However, the promise of Auger suppression has not yet to be observed in practical device material. At present time, the measured carrier lifetime is below 100 ns and is limited by Shockley−Read mechanism in both MWIR and LWIR compositions. Delicate design of barrier architecture is critical to improve its performance. Even though this promising technology is still developing and requires complex material heterostructures, there has been some first commercialized products available on the market.

1.2 Infrared Colloidal Quantum Dots

As mentioned in the preceding section, epitaxially grown IR materials have many advantages. For example, epitaxially grown quantum dots have promised higher temperature operation of infrared detectors[10, 16] due to the long carrier lifetime associated with their discrete density of states.[17] However, the epitaxial quantum dots have suffered from high fabrication cost. Colloidal

quantum dots (CQDs) could provide alternative solutions to the IR technology. Actually, they have showed promise as low cost alternative materials in the IR regime.[18-20]

Colloidal quantum dots are solution-processable semiconductor nanoparticles typically capped with organic ligands. Beginning in the early 1980s, CQDs were first studied by Ekimov *et al*[21] and Efros *et al*[22] as relatively monodisperse semiconductor nanocrystal precipitates in transparent glassy matrix. Shortly after that Brus *et al*[23] developed the synthesis of CQDs in liquid phase. Since then, the research on CQDs has seen tremendous momentum and growth[24-26] because of their various interesting advantages, including tunable optical properties via size tuning,[27] narrow size distributions, controllable surface chemistry, and solution-processability, which means low cost for CQDs device fabrication. The majority of the research has been focused on binary nanocrystal like II–VI, IV–VI, and III–V semiconductors such as CdE (E = S, Se, Te), PbE, and InP and InAs. In particular, CdSe CQDs in the visible spectrum have been studied most extensively.

The interest in colloidal quantum dots has also extended to the near-infrared regime with growing research on lead chalcogenides[18, 28-32] such as PbSe. Because most of the research use the interband transitions of the CQDs, it requires semiconductor materials with a relatively small band gap. PbSe has a bulk bandgap of 0.28 eV and in principle it could cover MWIR shorter than 4.4 μm. So far, PbSe CQDs have been only reported with absorption shorter than 3.6 μm at room temperature.[33] For longer wavelength infrared, smaller bandgap materials have to be sought. Therefore, the zero-bandgap HgTe would be an ideal candidate and the past two decades has seen growing research on HgTe. Around the year of 2000, Rogach *et al* made the first HgTe CQDs in aqueous reactions and showed broad absorption and PL in the visible and near-IR.[34-36] In 2006, Kovalenko *et al* synthesized small HgTe particles active in the near-IR with fairly narrow spectral features.[37] Particles with a diameter up to 10 nm were made and they showed absorption up to 3

μm and PL to 3.5 μm. However, because larger HgTe CQDs required a postsynthetic heat-induced Ostwald ripening, the size distributions broadened. In 2011, Keuleyan *et al* improved the HgTe CQD synthesis and for the first time showed photoconductivity beyond 5 μm with drop-cast thin films of HgTe CQDs on electrode. They are stable under ambient conditions and their detectivities are fairly high. Then they improved the synthesis with larger sizes and better monodispersivity. HgTe CQDs with sizes up to 15 nm were made, and they could even reach to 20 nm if using regrowth method. The corresponding room temperature photoluminescence and absorption edge reach into the long-wave infrared, past 8 μm. As a result, photoconductive response wavelength was pushed up to 12 μm using HgTe CQD[38] upon cooling to liquid nitrogen temperature (Figure 1-2).

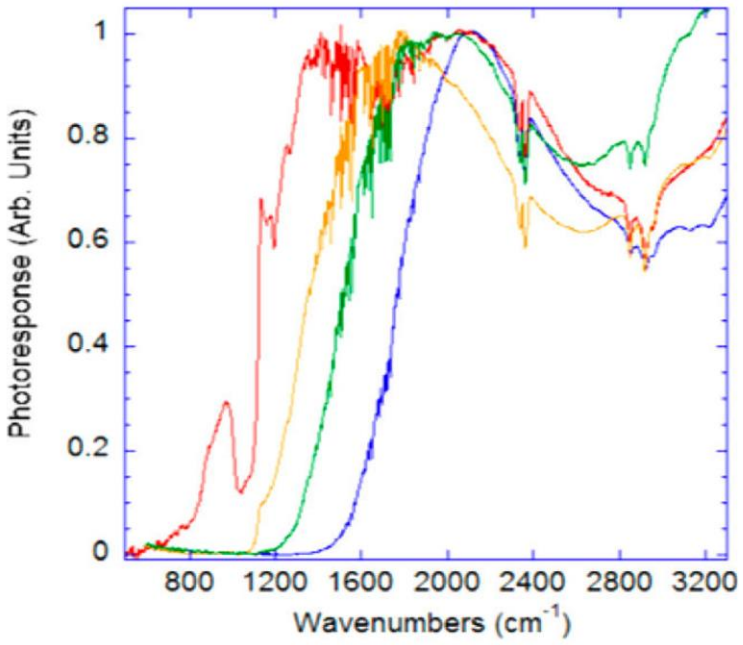

Figure 1-2 Photocurrent response of thin films of HgTe CQDs at 80 K. Adapted from reference 38.

Great progress has been made in the research of HgTe CQD in spite of the difficulties with it (such as its sensitivity to oxidation[39] because of the weak bond between Hg and Te due to the low

electronegativity of Te). Recently, through the collaboration of the Guyot-Sionnest lab and Sivananthan labs, an IR video was taken at 120 fps. The chip was made by drop-casting and cross linking 5 μm cut-off HgTe CQDs on a standard silicon ROIC.

1.3 Intraband Transitions and Doping in Quantum Dots

In the preceding section of infrared colloidal quantum dots, all the mentioned IR materials are restricted to narrow bandgap materials because they use interband transitions for infrared response. Actually, for the last three decades CQDs have been exclusively used for their interband transitions[24]. However, the size-tunable infrared response of the CQDs can also be obtained by using intraband or intersubband transitions, which are the transitions of carriers within the same band. In principle, if we could take advantage of the intraband transitions, any wide bandgap semiconductor CQD can be used for IR applications, including the nontoxic materials such as ZnO and many other CQDs with well-developed colloidal synthesis such as cadmium and lead chalcogenides.

In contrast to the scarcity of research on intraband transitions in CQDs, they have been used with great success in epitaxially grown nanostructures.[40] Indeed, a whole new perspective was possible when quantum wells of wide band gap semiconductor were shown to exhibit intense infrared transitions which could be controlled by the thickness.[41] As we have discussed in section 1.1.2, quantum well infrared detectors based on the wide gaps GaAs/AlGaAs were among the first devices to use these intersubband transitions[9] and QWIPs are now a commercial alternative to the traditional MCT detectors. Of even greater impact, the quantum cascade lasers (QCL), first demonstrated two decades ago,[42] used precise engineering of the intersubband energies and relaxation rates. This major achievement has spurred tremendous activity in semiconductor

physics and device development, and QCLs are now the most widely used tunable mid-IR laser source.

The use of intraband transition in CQDs could lead to many novel opportunities, but there are several challenges. Early on, the ultrafast excitonic relaxation of CQDs[43-44] seemed to preclude any application of higher excitonic states although there are now reports of multi-excitons production in photovoltaic devices.[45-46] Another problem is the organic ligands on CQDs, which create surface states and can affect the intraband states and their relaxation.[47] In addition, to observe the intraband transitions requires electrical doping, which is difficult with CQDs.[48-50] In the past, intraband transitions in CQDs were only observed transiently or in inert conditions. In the late 1990s, Hines and Shim *et al* reported well-defined size-tunable infrared transition spectra in CdSe CQDs after photoexcitation (Figure 1-3).[51-52] Then in 2000, Shim *et al* reported the first n-type nanocrystals using electron transfer from sodium biphenyl to the lowest unoccupied quantum-confined orbital of CdSe CQDs[53], which were dried and degassed first. They observed the appearance of infrared absorption spectra and concurrent optical bleach of the excitonic transitions as shown in Figure 1-4.

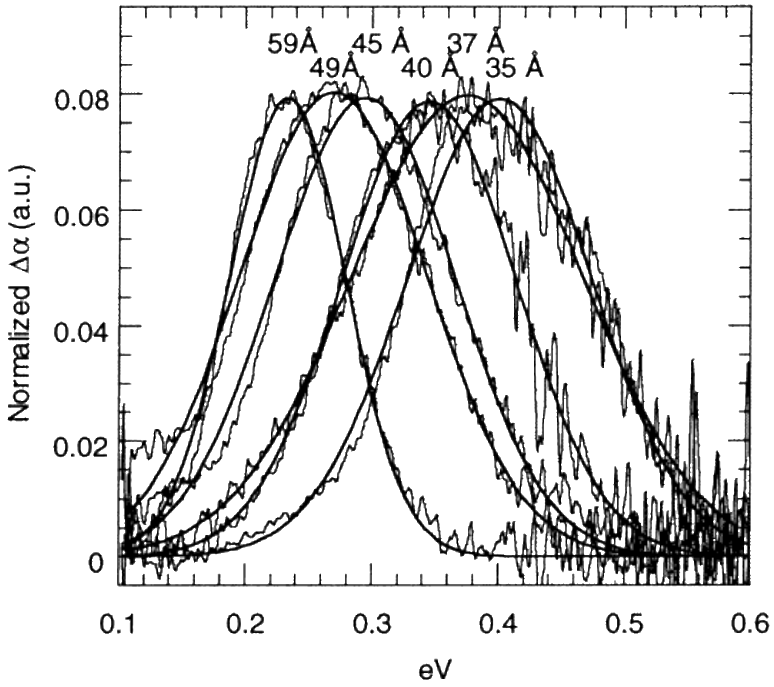

Figure 1-3 Transient intraband absorption of visible light-induced CdSe CQDs of indicated diameters using transient FTIR. Reprinted with permission from reference 52. Copyright 2000 American Chemical Society.

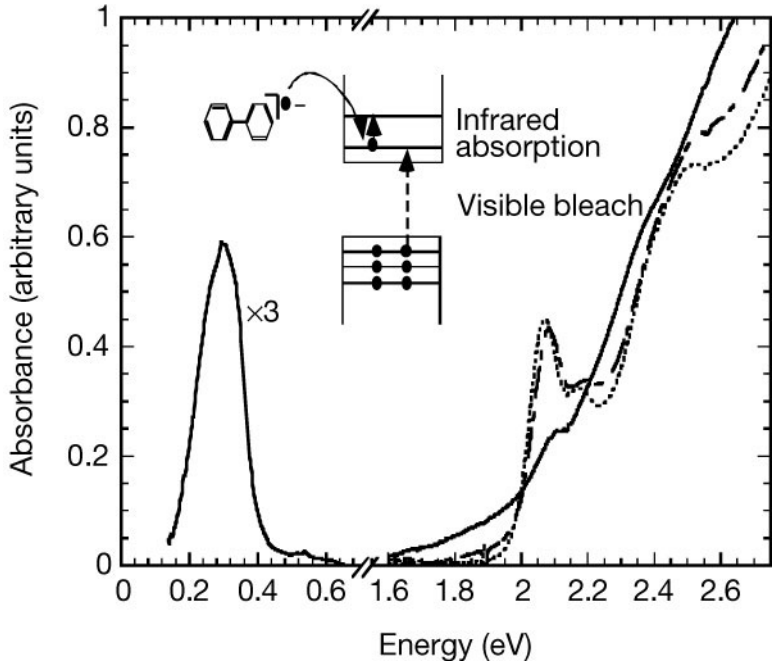

Figure 1-4 Spectra of CdSe nanocrystals before (dotted line), immediately after (solid line), and one day after (dashed line) the addition of sodium biphenyl. It is obvious to see the appearance

of infrared absorption spectra at 0.3 eV and concurrent bleach of the excitonic transitions from 2.0 to 2.2 eV. Reprinted with permission from ref 53.

Intraband transitions have also been observed by charge transfer by applying an electrochemical potential[54-55], reported by Wang *et al* in the early 2000s. No intraband transitions have been reported by the conventional impurity doping because of difficulty to incorporate impurity in small nanocrystals[56], and thermal ionization of the impurities, which provides free carriers, is hindered by strong confinement. All the successful doping and observation of intraband transitions have been achieved either transiently or in inert conditions. However, while it is very useful to investigate the CQDs electronic properties, it is not enough for the use in further intraband application, which requires stable doping of wide bandgap CQDs in the strong confinement regime. That situation was changed when the air-stable n-doped HgS[57] and HgSe[58] were synthesized by our lab in 2014.

The challenge of using intraband is from the difficulty of the doping and the lifetime of the 1Pe states. There is much interest in controlling the doping of colloidal quantum dots for applications such as light emitting devices, solar cells, photodetectors or electronics.[24] Impurity doping[48-49] as in bulk, or charge transfer doping[53] are the main approaches. Most applications do not need the Fermi level to be moved into the quantum dot interior states and raising it up or down within the gap is sufficient to create p-n junctions, albeit the optimum junction may require the largest excursion of the Fermi level. There is also interest in using colloidal quantum dot for infrared applications. Competing with small gap infrared materials, there should be a possibility of using the intraband transitions of established wide gap semiconductors. To use the intraband transitions, it then becomes imperative to have carriers occupy the quantum dot states, which is again a doping problem. However, for any quantum dot in the strongly confined regime, moving the Fermi level

so extensively has not yet been achieved by impurity doping, as evidenced by the lack of the intraband transitions, while it has been achieved by charge transfer only in inert conditions.

Chapter 2 HgS Colloidal Quantum Dots

Mercury chalcogenides have been studied due to their narrow bandgap, which is a requisite for infrared, especially the mid-IR application. During the research on HgTe colloidal quantum dots in our group, we started to study HgS for its potential optoelectronic properties in infrared. HgS exists in two forms at room temperature: the red hexagonal α-HgS, cinnabar, and the black zinc blende β-HgS, metacinnabar. While α-HgS is the stable bulk form at room temperature, chemical precipitation methods usually yield β-HgS.

Our report on β-HgS shows a first case of strongly confined quantum dots where carriers are stably in the lowest conduction band state under ambient conditions. The doping is controlled by the surface and explained by a rigid shift of the quantum states with respect to the environment.

Much of content in this chapter has been published in reference 57.

2.1 Synthesis of HgS CQDs

HgS CQDs were synthesized as early as in 1992 when Eychmuller *et al* [59] studied the photoluminescence of CdS nanocrystals in aqueous solution treated with $HgCl_2$. As they added increasing amount of $HgCl_2$ they noticed both the absorption and luminescence spectra extended from green to the red and near-infrared. They explained the observation by proposing that β-HgS (zinc blende) particles or islands were formed on the surface of CdS and created a CdS-HgS sandwich structure, where the valence band of HgS is above that of CdS and the conduction band of HgS is below that of CdS. As a consequence, after an electron-hole pair was formed after the

absorption of a photon, the electron and the hole are transferred to the HgS part of the sandwich colloid, where the electron and hole can recombine radiatively by emitting a photon of a wavelength determined by the bandgap of the HgS.

In 2002, Higginson and coworkers[60] synthesized HgS CQDs using the reverse micelle method to address the difficulties of controlling Hg(II) reactivity by organic ligand binding strengths. They used surfactant bis(2-ethylhexyl) sulfosuccinate (AOT) in cylcohexane to separate mercury(II) acetate and bis(trimethylsilyl)sulfide ($(TMS)_2S$) in different phases. Monodisperse HgS CQDs with 1-5 nm diameter were made and they showed tunable narrow absorption and PL between 500 and 800 nm. As with most Hg chalcogenide particles, they were seen to ripen and red-shift over time but this growth could be prevented by the addition of Cd or Zn, also increasing the PL QY (presumably forming a core-shell structure).

Colloidal HgS was also synthesized by Keuleyan in our lab indirectly.[61] In an attempt to grow a HgS shell on HgTe CQDs, he noticed that the absorption red-shifted and broadened, and a distinct absorption below 2000 cm^{-1} appeared after injection of the $(TMS)_2S$ into the HgTe CQD solution, as indicated in Figure 2-1. Over time, the HgTe absorption feature further broadens and red-shifts, but the new feature in below 2000 cm^{-1} remains unchanged. The TEM images clearly revealed two types of particles in the sample: the typical aggregated, elongated HgTe particles, and spherical, polydisperse HgS, with a mean diameter of 6.5 nm and a standard deviation of 1.6 nm (25%). Then he tried sulfur powder in oleylamine as the sulfur precursor, using a method similar to that of Joo *et al* for Pb, Zn, Cd, and Mn sulfide particles[62]. However, this S source gives irregular particle shapes. Equivalent sulfur powder and $HgCl_2$ miexed with octadecylamine reacted as soon as the ODA melted, also resulting in irregular shapes of HgS.

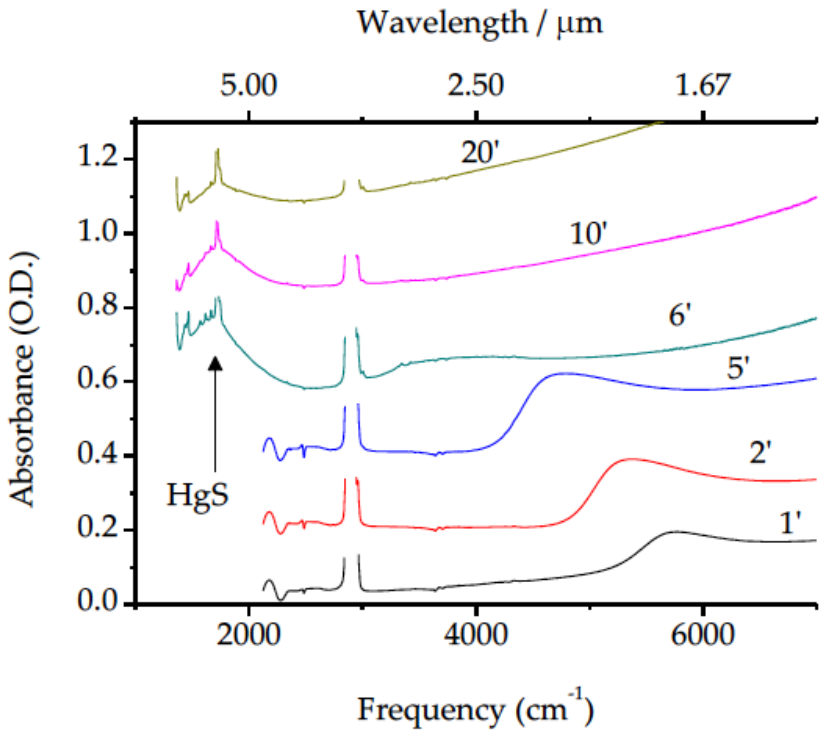

Figure 2-1 Absorption spectra of HgTe samples taken at different growth time. $(TMS)_2S$ was injected after 5 minutes and the formation of HgS is indicated by the absorption near 1500 cm^{-1}. The C-H absorption band near 2900 cm^{-1} is removed for clarity. HgTe samples before $(TMS)_2S$ injection show only ligand vibrational absorptions below 2000 cm^{-1}.

A novel improved synthesis of spherical HgS CQDs with better size and shape control was developed later based on the colloidal synthesis of HgTe nanocrystals.[63] In the HgTe synthesis, Te in tri-n-octylphosphine (TOPTe) is used as the tellurium precursor. However, simply replacing Te with S gives no reaction. This is attributed to the stronger P=E (E = S, Se, Te) bond in the order of S > Se > Te, which only cleaves in the case of TOPTe. Instead, we found three other sulfur precursors which yield spherical particles: thioacetamide, bis(trimethylsilyl) sulfide $(TMS)_2S$, and $(NH_4)_2S$ with generally larger mean particle size in that order. In a typical synthesis of HgS CQDs, 81 mg of mercury(II) chloride ($HgCl_2$) and 10 mL of oleylamine were loaded into a 50 mL round bottom flask. The $HgCl_2$ and oleylamine solution was heated under vacuum at 120 °C for one hour and then was cooled to 30°C under Ar. 0.3 mL of 1 M freshly prepared thioacetamide in oleylamine

was quickly injected and the solution instantly turned black, indicating the fast formation of HgS. No significant growth was observed over time between 30 minutes and one hour. This method produced samples typically having an exciton absorption feature near 10000 cm^{-1} (1 μm) with an absorption onset near 8000-9000 cm^{-1}. The reaction was stopped by transferring to a solution of two volume equivalents of 10 % (volume) dodecanethiol and 1 % trioctylphosphine in tetrachloroethylene (TCE). After precipitation with ethanol as a non-solvent, they are cleaned multiple times with ethanol before dissolving in TCE or toluene for characterization.

They are roughly spherical as shown in Figure 2-2 room temperature but chemical precipitation methods yield β-HgS as shown in Figure 2-3.

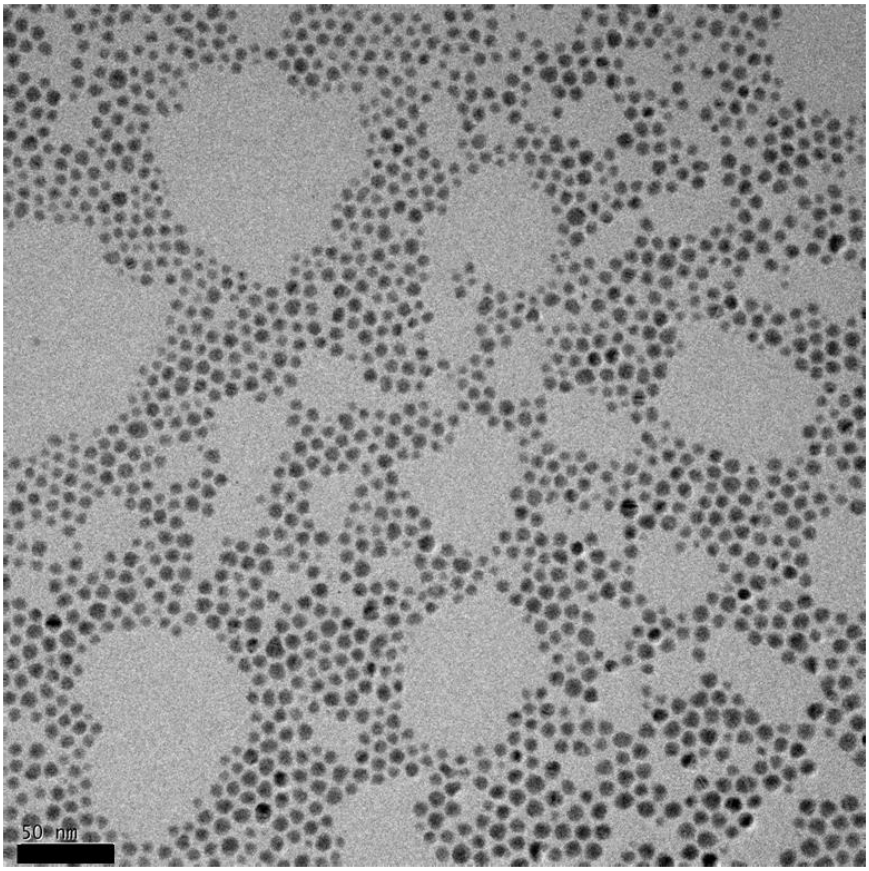

Figure 2-2 The average size is 6.4 nm and the standard deviation is 1.3 nm. Scale bar is 50 nm.

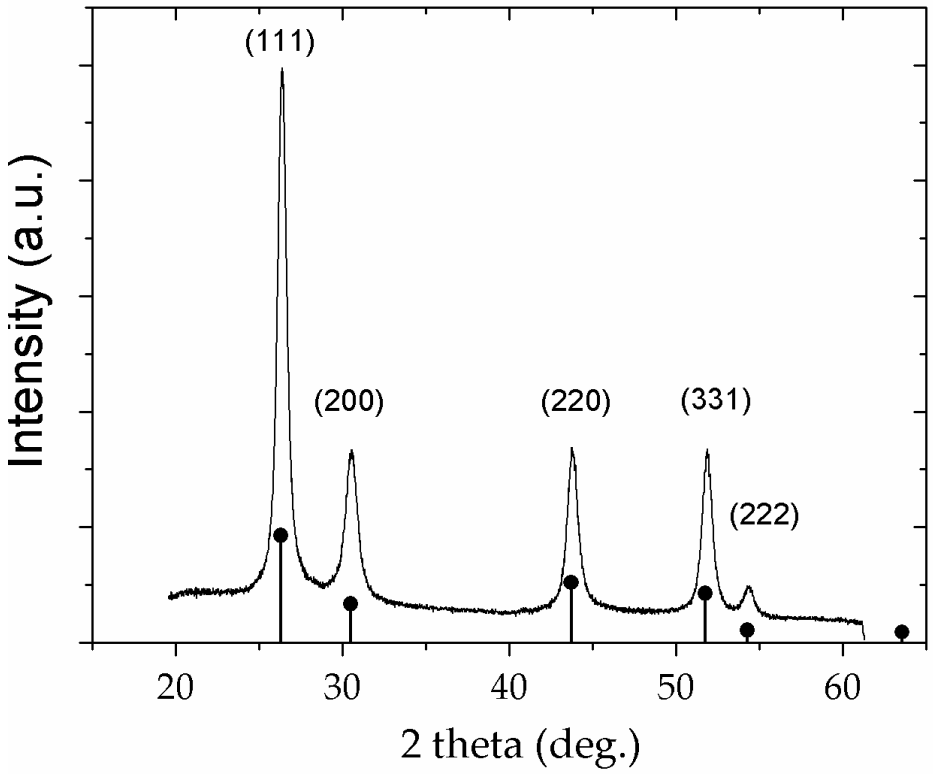

Figure 2-3 *X-ray diffraction spectrum. Bulk β-HgS peak positions are indicated.*

2.2 Optical Property and Its Sensitivity to Surface

In an attempt to regrow the HgS CQDs with the atomic layer deposition (ALD)[64-65] method, we discovered very fascinating optical properties of the HgS CQDs: the absorption changes towards alternating S^{2-} and Hg^{2+} addition.

2.2.1 Experimental

The layer-by-layer growth was done by alternating sulfur and mercury reagents. For the sulfur treatment, 1 mL of formamide, 50 μL of oleylamine and 150 μL of 0.1 M $(NH_4)_2S$ were added to 1 mL of colloidal HgS solution in TCE (the optical density of the HgS solution is about 0.1 at the interband shoulder). This mixture was stirred for about 5 minutes, and then the HgS dots were washed twice with formamide to remove extra $(NH_4)_2S$. For the mercury step, 1 mL of formamide

and 150 uL of 0.1 M $HgCl_2$ (or Hg acetate, which provides the same result) solution in formamide were added to 1 mL of sulfur-rich HgS CQD solution. This mixture was stirred for about 5 minutes before being washed with formamide. Then the HgS solution was ready for the FTIR and other measurements.

For the inductively coupled plasma (ICP) measurement, the HgS CQDs were dried and dissolved in 1% v/v HNO_3 and 1% HCl aqueous solution and analyzed using ICP optical emission spectrometer (Agilent 700 series).

2.2.2 Results and Discussion

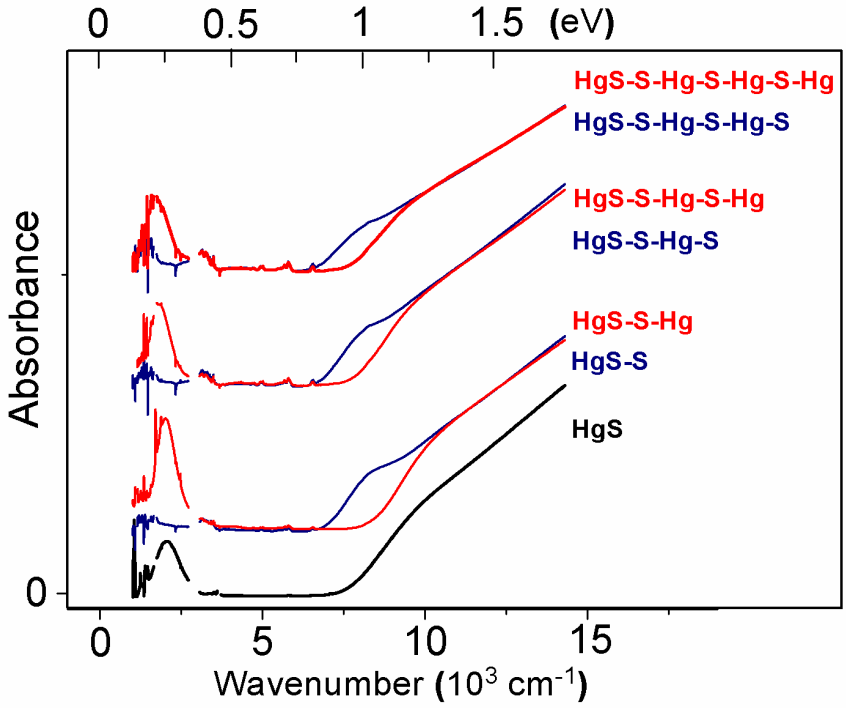

Figure 2-4 *Spectra of ~ 5 nm HgS CQDs with alternating S^{2-} and Hg^{2+} layer by layer growth. The HgS (black) corresponds to the untreated dots, and S (blue) and Hg (red) represents the S^{2-} and Hg^{2+} surface treatments, respectively. Vibrational absorptions were removed for clarity.*

Figure 2-4 shows the absorption spectra of HgS nanocrystals before (black curve) and after (red and blue) the surface treatment. The particle size is about 5 nm in diameter and the spectra were measured in TCE solution under ambient conditions. As the black spectrum shows, for the as-prepared HgS CQDs, there is a strong mid-IR absorption around 2000 cm^{-1}, which is very well isolated from the NIR edge at ~ 9000 cm^{-1}. After applying a layer by layer growth[65] on the HgS CQDs with Hg^{2+} and S^{2-}, the particles grew larger, monolayer by monolayer, as shown by the redshift of the absorption, but at the same time, the spectra changed completely. The sulfide red-shifts the NIR edge and removes the mid-IR absorption, while the Hg^{2+} blue-shifts the NIR edge and induces the mid-IR absorption. The transfer of oscillator strength between the NIR edge and the mid-IR absorption is quantitative, systematic and irrespective of the order of surface exposure to the ions. ICP optical emission spectrometry confirms changes in the composition of the Hg treated and S treated HgS CQDs: The Hg treated dots have 30% more Hg than S, while the S treated dots have almost equivalent amount of Hg and S.

Almost all HgS particles (with the exception of some of the smallest) show similar spectral features, which resemble spectra of n-doped CdSe nanocrystals after charge transfer as we discussed in section 1.3. Other similar spectral features have also been observed for CdS, ZnO, PbSe, and HgTe quantum dots,[53, 66-67] but all these CQDs only showed the distinct and isolated spectral feature after charge transfer. Another relevant example is seen in work done in our group by Dr. H. Liu on electrochemical charging of HgTe.[68] Therefore, we proposed that the β-HgS CQDs can be stably doped in ambient conditions such that they exhibit a stable intraband absorption in the mid-IR, which has never observed before. We also proposed that the doping can be controlled by the surface condition of the nanocrystals. Our hypothesis will be discussed and confirmed with experiments in the following sections.

2.3 Electrochemistry Experiments

Since HgS has not been studied much as a colloidal quantum dot, we used spectroelectrochemistry to (i) determine the sign of the carrier, (ii) verify the quantum confinement of the nanocrystals, (iii) determine the bandgap, and (iv) the mechanism of doping.

2.3.1 Experimental

Film preparation

HgS CQD films were prepared via multiple layer deposition. HgS CQDs (~20 mg/mL) in hexane/octane (9:1) solution and 1% hexanedithiol (HDT) in methanol were used for film preparation. The film was drop-cast onto a polished Pt disk working electrode (R=3.5mm) and then immersed in HDT methanol solution to replace the dodecanethiol bound to the CQDs.

Spectroelectrochemistry

For the spectroelectrocemical studies, the hexanedithiol crosslinked HgS CQD film was dried for 1 hour under vacuum and placed into a spectroelectrochemical cell. The electrochemical cell is comprised of three electrodes: A Ag pseudo reference electrode, Pt working electrode and Pt counter electrode. Tetrabutylammonium perchlorate (TBAP, 0.1 M) in propylene carbonate was injected into the electrochemical cell inside the glovebox. The electrochemical cell was placed inside of the FTIR, the Pt electrode was lightly pressed against a CaF_2 window and the infrared light reflected from the Pt working electrode was collected by an MCT detector.

Cyclic voltammetry

Hexanedithiol capped HgS CQD film were deposited on an interdigitated electrode (Abtech Scientific, 50 periods of 5mm long 10μm spaced electrodes) and immersed into 0.1 M tetrabutylammonium perchlorate (TBAP) in propylene carbonate. A Ag pseudo reference and Pt

counter wire electrode were used for the cyclic voltammetry using a bipotentiostat. A function generator was used to scan the range of interest at a scan rate of 0.05 V/s scan rate.

Conductivity measurement

The conductance between the two working electrodes with 4.5 mV bias is measured with a TBAP propylene carbonate solution was used for the reference. Interdigitated electrode (Abtech Scienctific) was utilized to measure the conductance of HgS CQDs and a Pt wire was used for the counter electrode and the reference electrode was either a Ag/AgCl pseudo reference or a ferrocene/ferrocenium reference.

Resting potential measurement

A Pt wire was dipped into HgS CQD (10mg/mL) solution and crosslinked with ethanedithiol in methanol. For the film, after ethanedithiol crosslinking, the resting potential was ~ -50 mV. The film was then taken out, rinsed and dipped 10 s in a $HgCl_2$/formamide solution. After rinsing with ethanol and drying with N_2 gas, the resting potential was measured again, and showed a value of ~ +250 mV. The sample was then taken out, rinsed and dipped in a $(NH_4)_2S$/formamide solution, and the resting potential returned to a value close to 0 V. Tetrabutylammonium perchlorate in formamide (0.1 M) was used as an electrolyte. A Ag/AgCl pseudo reference was used.

k·p model prediction

A two-band k·p model with a Hamiltonian $H=\begin{pmatrix} 0 & Ak \\ Ak & -E_G \end{pmatrix}$ gives the non parabolic energy dispersion $E = \frac{-E_G}{2} + \sqrt{\left(\frac{E_G}{2}\right)^2 + A^2k^2}$ for the conduction band. This equation can be inverted to give $k^2 = \frac{1}{A}\left[\left(E + \frac{E_G}{2}\right)^2 - \left(\frac{E_G}{2}\right)^2\right]$. The heavy hole band is assumed dispersion-less. In a spherical box of radius R, the $1S_e$ state has $k_{1S} = \pi/R$, and the $1P_e$ state has $k_{1P} = 4.49/R$. This gives the intraband energy $E_y = E_{1Pe} - E_{1Se}$. The interband energy is given by $E_x = E_G + E_{1Se}$. The equation

fitting the data is then $E_y = \frac{E_G}{2} - E_x + \sqrt{\left(\frac{E_G}{2}\right)^2 + \left(\frac{4.49}{\pi}\right)^2 \left[\left(E_x - \frac{E_G}{2}\right)^2 - \left(\frac{E_G}{2}\right)^2\right]}$. The Kane parameter implicit in A in the k·p Hamiltonian is not in the fitting equation and the only parameter is the gap E_G. The model neglects the valence band dispersion and Coulomb interactions.

Calculation of Redox Potential

The redox decomposition of a semiconductor can be estimated by its relevant surface reactions, as pointed out by Gerischer.[69] For HgS, the surface may undergo reduction (a) $(HgS)_n + 2e^- \rightarrow (HgS)_{n-1}$ Hg + S^{2-} (solvent) or oxidation (b) $(HgS)_n + 2h^+ \rightarrow (HgS)_{n-1}S + Hg^{2+}$ (solvent). The standard energy of formation of HgS is ΔG_f^0= -43 kJ/mol. The standard reduction potentials of S/S^{2-} is E^0 = -0.51 V and for Hg^{2+}/Hg, E^0 = +0.85 V, both for aqueous solutions. Therefore, the potential for (a) is then $E_{red} = E^0_S + \Delta G_f^0/2F$ = -0.73 V, and the potential for (b) is $E_{ox} = E^0_{Hg} - \Delta G_f^0/2F$ = +1.07 V (in respect to NHE reference), where F is the Faraday constant. HgS is unstable to oxidation if holes are present at a potential more positive than +1.01 V and unstable to reduction at a potential more negative than -0.73V. If reactions can stabilize the ions in solutions, the range of potential will be smaller. For example, polysulfide formations or acidic conditions to form HS^- or H_2S would make the reduction easier. Similarly, the formation of stable soluble complexes with Hg^{2+} will facilitate oxidation. In the absence of these, the potential range of [-0.73V, +1.07V] provides a guideline of the stability range. The valence and conduction band have to be within that range for stable p and n-type doping, respectively.

2.3.2 Proof of n-Doping

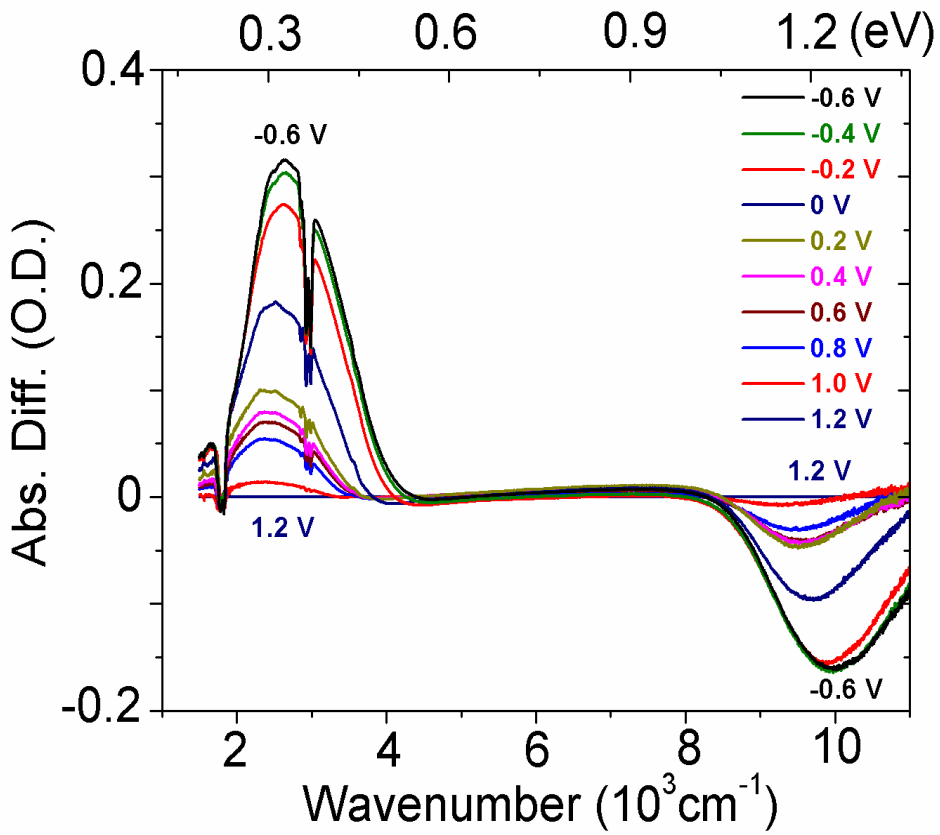

Figure 2-5 Difference spectra of a film HgS CQD under increasingly negative potential vs Ag/AgCl. The spectrum measured at +1.2 V is used as the reference.

For the spectroelectrochemistry experiment, HgS nanocrystals of different average sizes from ~3.5 to ~14 nm were deposited as a film on a Pt electrode. They were crosslinked by hexanedithiol to render them insoluble in the electrolyte and to improve electron transfer.[68] Figure 2-5 shows difference infrared spectra between various potentials and +1.2 V with respect to the pseudo reference electrode Ag/AgCl for the smallest sample of average size ~3.5 nm. As the potential is moved to the negative direction, the mid-IR absorption starts around 2350 cm^{-1}, and gains strength as it moves towards 2600 cm^{-1} at the most negative potential, -0.6 V. At the same time, the near-IR shows a bleach that increases for the more negative potentials. The transfer of oscillator strength is similar to the observations described above for the layer by layer modification in solution and

typical of previous spectroelectrochemical studies on strongly confined quantum dots. The fact that the intraband transition appears for negative potential allows its assignment to the conduction band and the doping as n-type.

2.3.3 Verification of quantum confinement

To determine the extent to which the carriers are quantum confined, we investigated the tuning of the energy of the spectral features. By taking difference spectra every 100 mV, the mid-IR absorption and near-IR bleach show well defined Gaussian peaks. Figure 2-6 shows the complete set of the peaks of mid-IR absorption as a function the peaks of the NIR bleach. The NIR bleach blueshifts with smaller sizes, covering a range of more than 0.6 eV. This is the evidence that the HgS nanocrystals are strongly quantum confined.

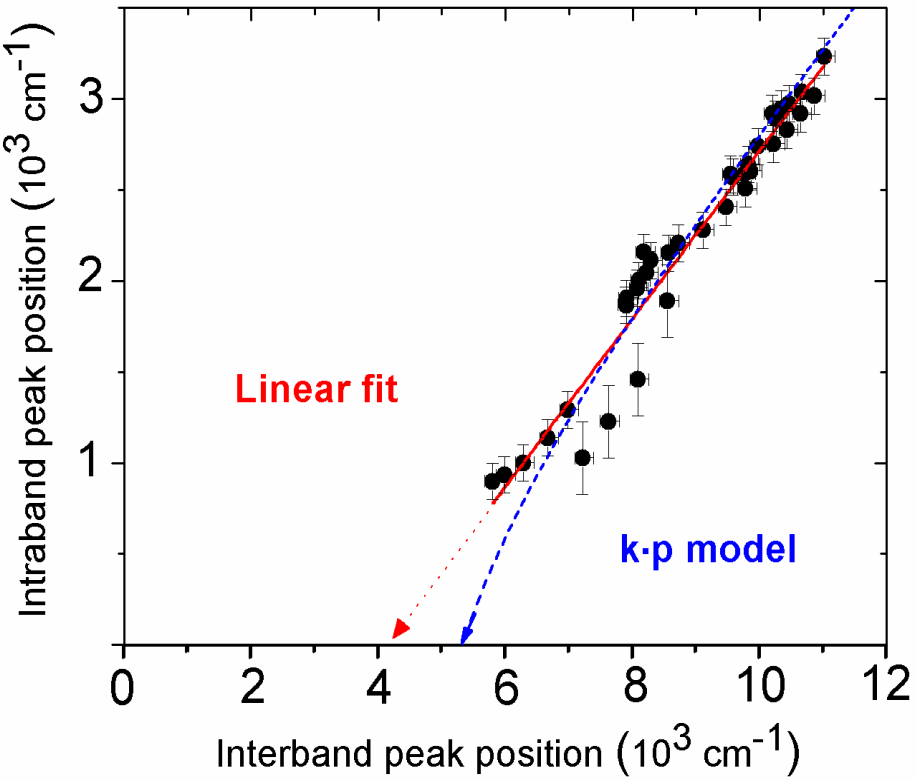

Figure 2-6 Mid-IR peak vs Near-IR peak energies. The red line is a linear fit and the blue line is the k•p prediction.

2.3.4 Determination of the bandgap

As shown in Figure 2-6, a linear extrapolation of the intraband energy to zero would give a bandgap of 0.51 ± 0.04 eV. A linear extrapolation would be justified only in the effective mass approximation but assigning the intraband absorption to the $1S_e$-$1P_e$ electronic transition for a spherical dot gives a slope of ~1, which fails to describe the data. The non-parabolic approximation, specifically a two band k·p model, captures the data better with no other parameter than the bandgap value of 0.66 eV. We note that the bulk bandgap of β-HgS is very uncertain in the literature with experimental values between -0.5 eV and +0.5 eV[70]. Weller and coworkers synthesized β-HgS in aqueous solutions, with absorption and luminescence in the near-infrared[59] and stated a bulk bandgap of +0.5 eV[71] while Kuno and coworkers synthesized smaller particles in organic solvents with fluorescence in the visible[60] and stated the band gap as negative, but neither reports measured the bulk gap. There is theoretical interest in β-HgS as well as a topological insulator[72] but the calculated bulk gaps also range from negative to positive values. The band gap of ~ 0.6 eV measured here is similar to the value stated by Weller and coworkers.[71]

2.3.5 Mechanism of N-Doping and Its Sensitivity to Surface Treatment

The mechanism of how the n-type CQDs are air-stable and created by the surface exposure to Hg^{2+} is now discussed. The n-type doping of HgS CQD cannot be explained by charge transfer from the adsorbate, or by the electronegativity of the adsorbate since the electronegative sulfide (S^{2-}) instead removes the electrons from the dots as indicated by the bleach of the intraband absorption shown in Figure 2-4. An alternative possibility is that the surface introduces an energy shift of the nanocrystal states with respect to the environment, stabilizing the doping. The surface can indeed affect the reduction potential of quantum dots by changing the electrostatic potential.

For example, changes in transport of CdSe nanowire FETs after exposure to solutions of sulfide or metal ions and subsequent thermal processing have been reported and it has been proposed that the surface composition plays an important role in doping.[73] The use of surface ligands to optimize the *p-n* junction in nanocrystal films has been reported as well.[74]

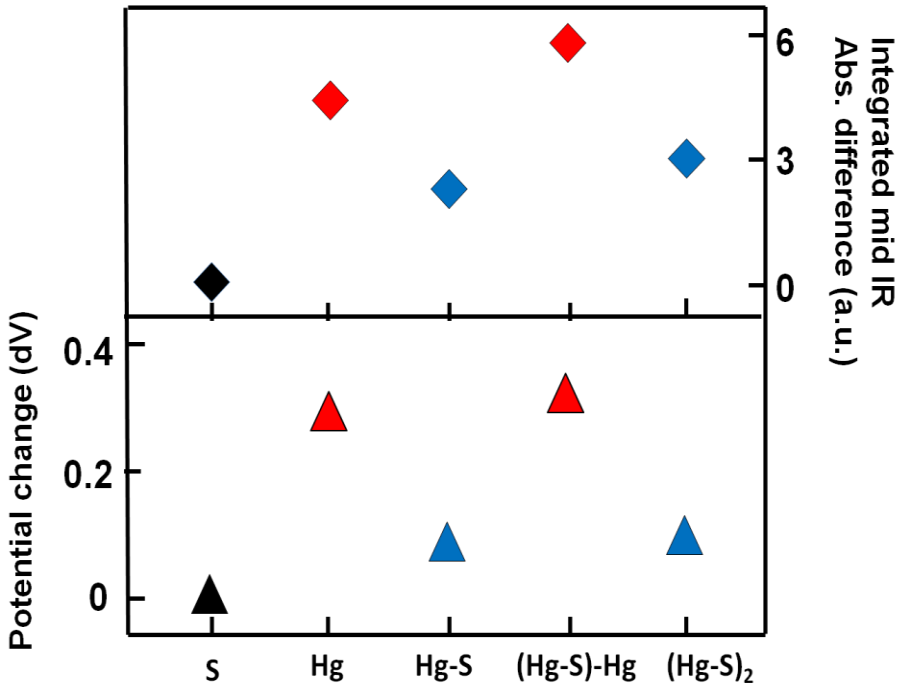

Figure 2-7 Resting potential difference and integrated mid-infrared absorption of a HgS CQD film after alternate exposure to Hg^{2+} and S^{2-} ions. The results are relative to the first measurement of the ethanedithiol crosslinked HgS CQD film. The resting potential is measured 40 seconds after immersion in the electrolyte.

To investigate if the potential of the dots changes with surface modifications, the resting potential of an ethanedithiol cross-linked HgS CQD film on a Pt wire was measured with respect to an Ag/AgCl pseudoreference in a formamide/tetrabutylammonium perchlorate electrolyte. The wire was alternately exposed to mercury or sulfide ions solutions, rinsed and dried. The data in Figure 2-7 show alternating resting potentials between ~ 0 and ~ +300 mV with the positive potentials after mercury ions exposure. On films deposited on an IR transparent CaF_2 substrate

but processed in the same manner, the strength of the intraband absorption of the film also alternates with the mercury and sulfide treatment. Unlike the spectra for the colloidal solutions in Figure 2-4, the intraband absorption in the film is not as completely quenched by sulfur as shown in Figure 2-8, which is tentatively attributed to the different environment (polar electrolyte vs nonpolar solvent) and accessibility in the film but the trends are similar.

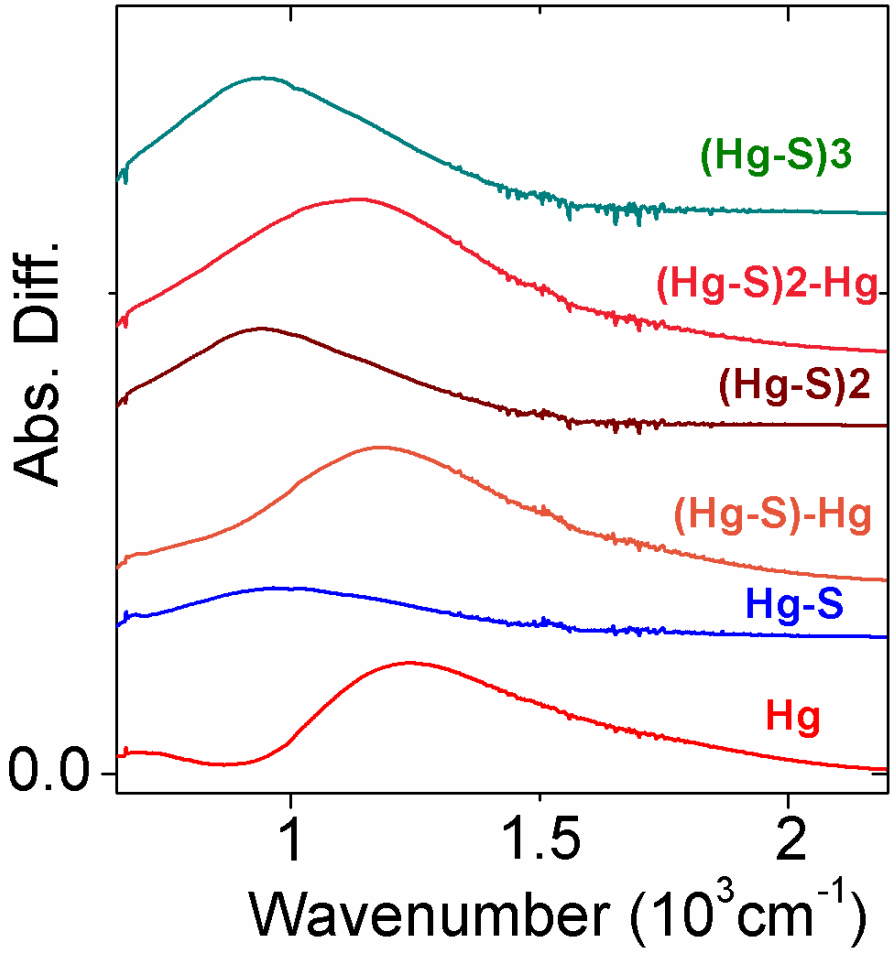

Figure 2-8 Absorption spectra of HgS CQD film with alternating Hg^{2+} and S^{2-} exposure. The intraband absorption is sensitive to surface treatment. The trend of its respective increase and decrease by Hg^{2+} and S^{2-} treatment is similar to the result of HgS in solution but the intraband absorption is not fully quenched by sulfur treatment in films.

Figure 2-7 shows the strong correlation of both measurements as a function of the surface exposure. Therefore, these measurements confirm the idea that the surface moves the energy levels with respect to the environment rather than serves as a dopant. Effectively, the surface tunes the redox potential of the nanocrystals.[75] Campbell *et al.* showed how a work function can shift by 1 V in air with dipolar self-assembled monolayers.[76] As shown in Figure 2-9, a surface dipole pointing inward (positive end on the surface) raises the electric potential inside (+ V) which stabilizes the electron (- eV) and increases the work function. For a sphere with a radius much larger than the dipole layer thickness, the energy shift is $\Delta E_f = \sigma_d/\varepsilon\varepsilon_0$ (eV) where σ_d is the surface dipole density with the positive direction towards outside and ε is the dielectric constant in the dipole layer. The effect can be large. Assuming that the surface dipole due to the ions alternates between +1 D and -1 D pointing outside the particle, and that each ion occupies a surface of 20 $Å^2$, as an estimated surface coverage of ions on the (111) plane, using the smallest screening with ε=1, the energy shift is ~ ±1.8 eV.

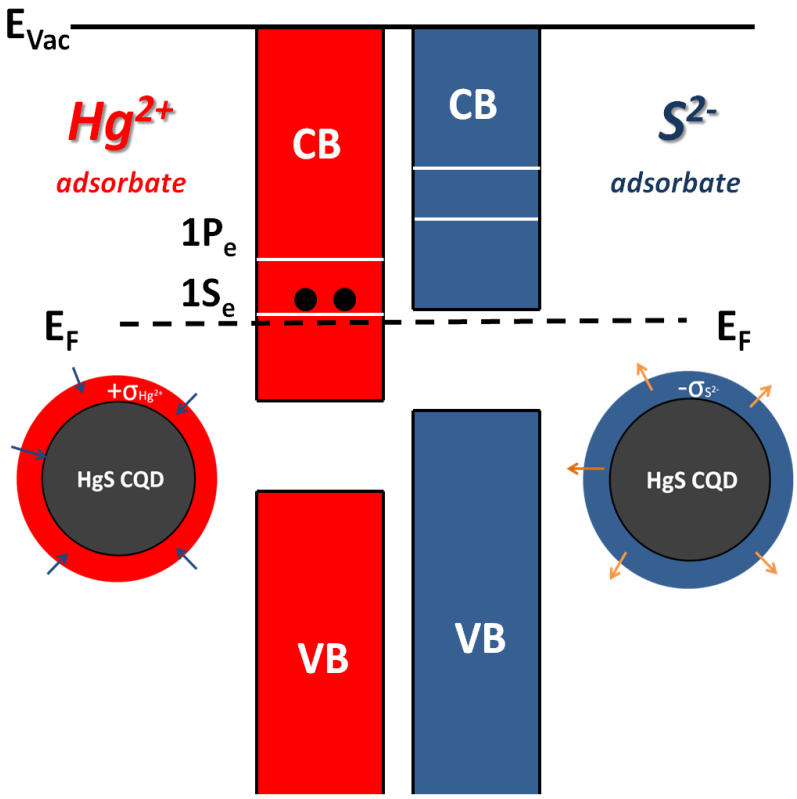

Figure 2-9 Schematic energy diagrams of the Hg^{2+} doped and the S^{2-} treated HgS CQDs.

The alternating Hg^{2+} and S^{2-} additions lead to surface dipole layers of varying magnitude or polarity. A dipole pointing from the ligands to Hg^{2+} lowers the quantum dot states with respect to the outside, while the dipole from S^{2-} to the ligands raises them (Figure 2-9). The occupation of the electronic states is determined by the Fermi level of the environment and shifting the dot electron state quantum state above (S^{2-}) and below (Hg^{2+}) leads to the doping observed. The electrostatic shift captures the essence of the mechanism of the sensitivity of the doping to the surface of nanocrystals.

2.3.6 Conductance and Surface Treatment

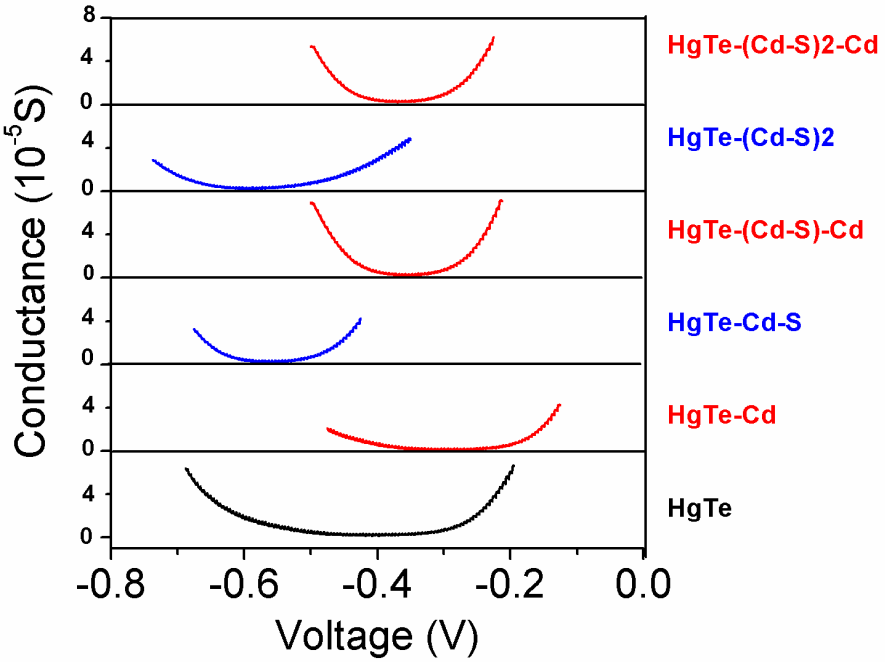

Figure 2-10 Shift of the conductance curve for HgTe CQD films with alternating exposure to Cd^{2+} and S^{2-}.

To test the effect of surface treatment, we also applied similar treatment on HgTe CQDs, another material studied in our group. We found that this approach can also modify the n and p-type character of ambipolar HgTe. Figure 2-10 shows how the electrical conductance of HgTe CQD films is shifted n or p (with respect to an arbitrary potential) by the surface treatment with cadmium and sulfide ions, and it is noteworthy that the shift is of the order of the bulk bandgap.

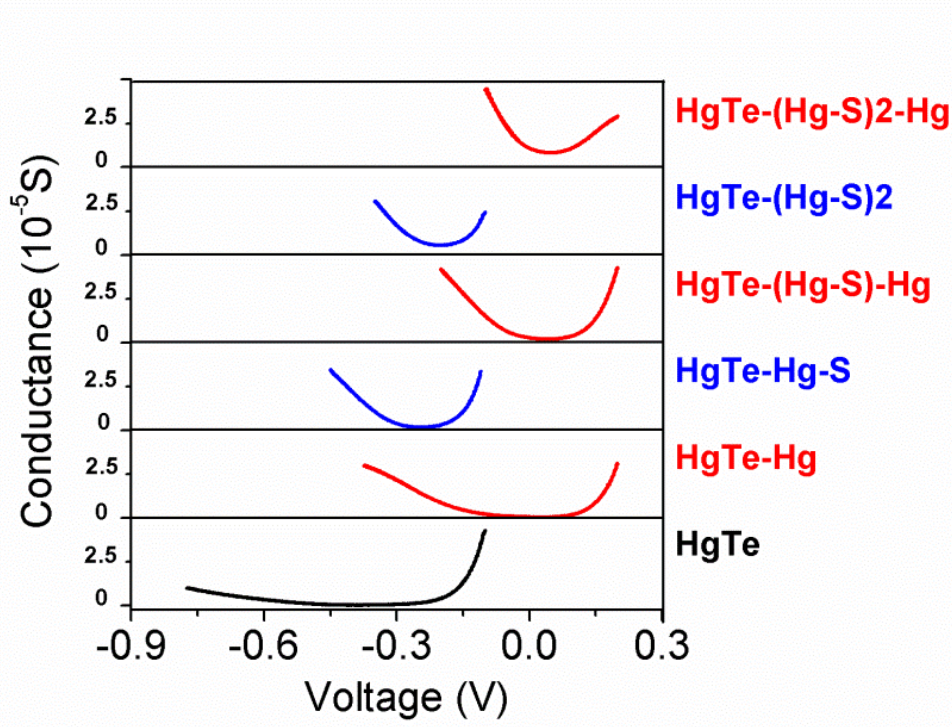

Figure 2-11 Conductance of HgTe CQD films with alternating Hg^{2+} and S^{2-} treatment.

Similar effects on HgTe CQD film were observed with Hg^{2+} and S^{2-} treatment in Figure 2-11. The Hg^{2+} doping shifts the electron reduction potential in the positive direction whereas the S^{2-} doping shifts in the negative direction. However, unlike Cd^{2+} and S^{2-} treatment, the energy difference between electron and hole injection into the HgTe CQD solid gradually decreases while iterating the surface doping process and this is attributed to narrowing, or maybe closing of the HgTe quantum dot gap with HgS shell growth.

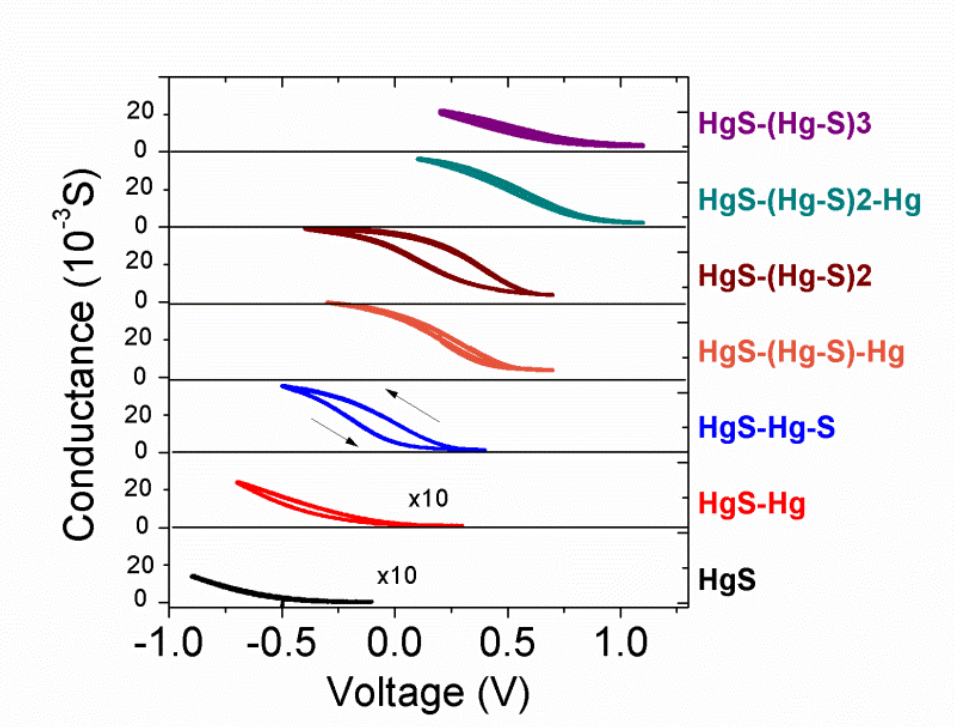

Figure 2-12 Conductance of HgS CQD films with alternating Hg^{2+} and S^{2-} exposure.

Figure 2-12 shows the conductivity change of HgS CQD film by Hg^{2+} and S^{2-} exposure using Fc/Fc^{+} reference electrode. The conductivity is only observed n-type. Mercury exposure moves the redox potential in the positive direction. Sulfide exposure makes the reduction potential more negative or unchanged, and shows a hysteresis which we tentatively attribute to the irreversible oxidation of sulfides to polysulfides at such positive potentials. Unlike HgTe, where potentials are kept small, there is a net gradual positive shift of the electron injection potential to large positive values (~ 1V) which is consistent with the air-stable intraband absorption in Figure 2-8.

The ambient stability of doping of a solvated quantum dot is first determined by the Fermi level of the environment. In humid air, this is likely determined by the oxygen/water equilibrium, around +0.81 V/NHE (= +0.58 V vs Ag/AgCl = +0.17 V vs Fc/Fc^{+}) at neutral pH. Electrons above this potential are unstable to oxidation. As shown in Figure 2-5, the HgS films are easily electron doped at this potential, and therefore air stability is indeed established. However, the absence of p-doping

is limited by the oxidative decomposition of HgS.[69] Therefore, at a potential just above where electrons are injected, hole injection would already lead to oxidative decomposition. This may explain why HgS CQDs are not ambipolar, unlike HgTe CQDs. For dots in a film, in contrast to dots in solution, the spatial extent of the electrostatic potential can be much larger and the doping stability is determined by the diffusion of oxidizing or reducing species such that films could still be n or p- type even though the isolated dots may be unstable.

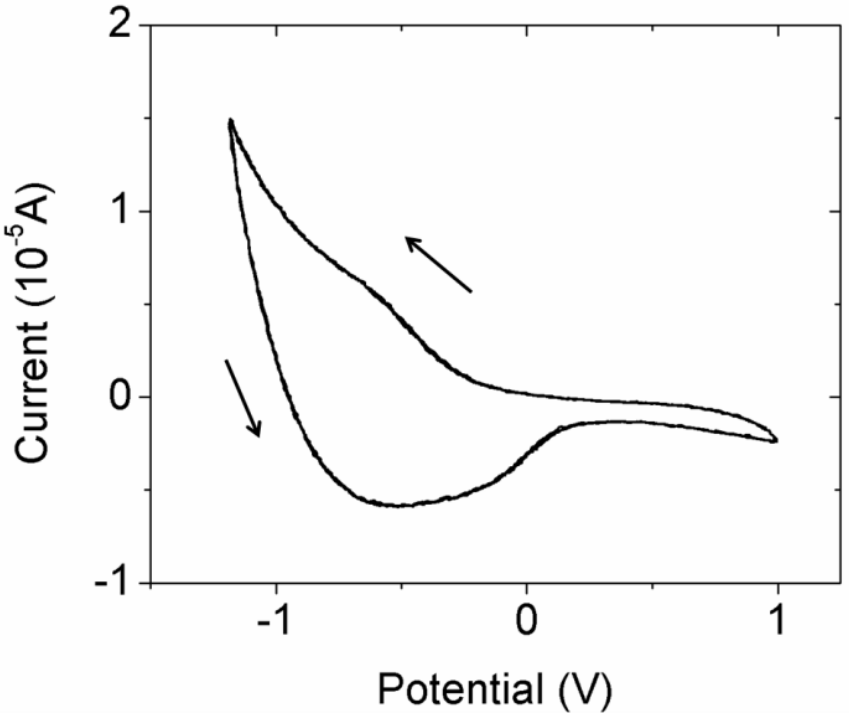

Figure 2-13 Cyclic voltammogram of HgS CQD solid film.

Using interdigitated electrodes, the electrochemistry also confirms that the injected electrons are conductive as expected from many prior studies on other quantum dot solids, while cyclic voltammetry **(**Figure 2-13**)** shows the typical waveform expected for nearly reversible charge injection. It is noted that no electrochromic effects and no conductivity are obtained in the oxidizing direction, indicating that p-type HgS CQDs are not stable, most likely because holes oxidize the surface. Thus, unlike HgTe, HgS is not ambipolar.

2.4 Intraband PL and Photodetection

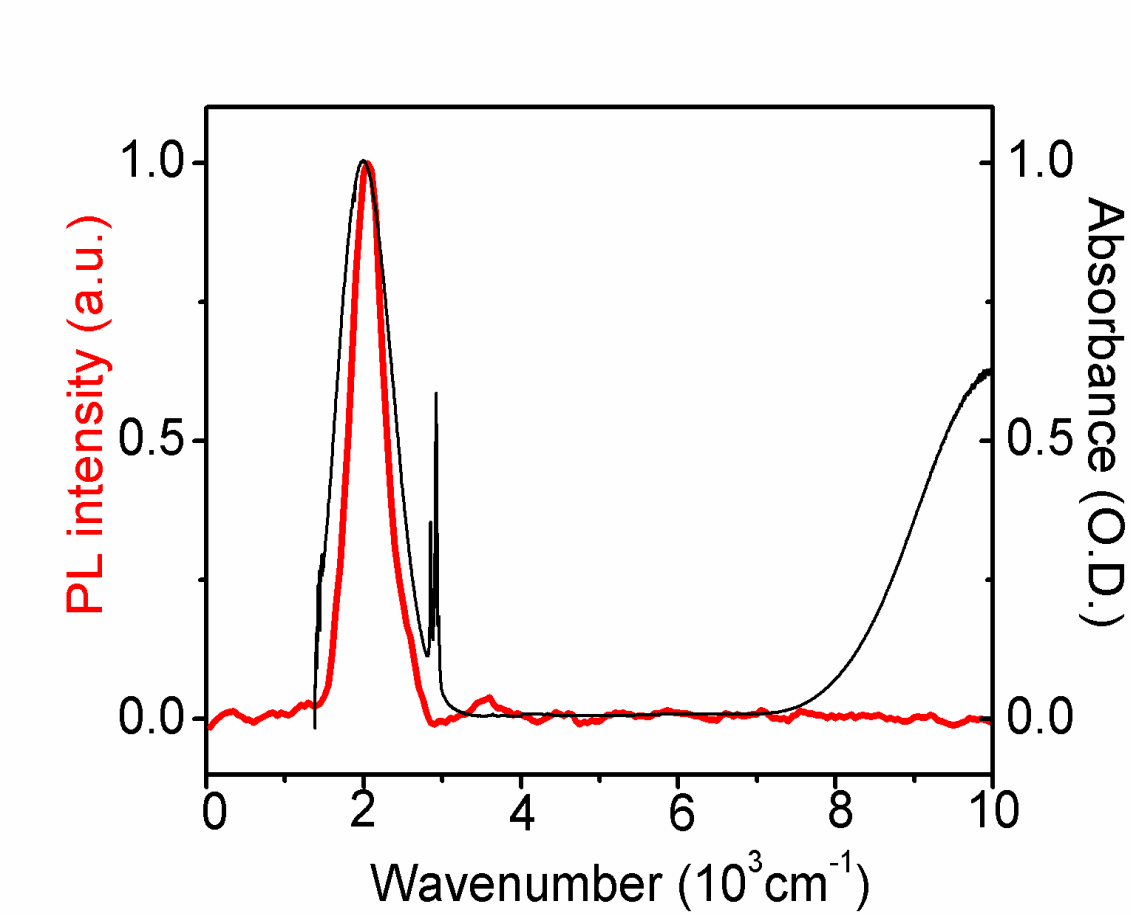

Figure 2-14 Intraband PL emission (red) from the $1S_e$-$1P_e$ transition of ambient n-type HgS nanocrystals after photoexcitation at 808 nm. The absorption is the black curve.

Returning to the possibility of using the intraband transitions, the consequence of the stable doping is that it transforms the "wide" gap β-HgS (0.6 eV as shown earlier) to a narrow gap semiconductor where the gap is now between the two first electronic states, $1S_e$ and $1P_e$, in spherical dots. This opens up the possibility of photophysical investigation of devices based on the permanently stable intraband absorption. One striking observation is the first observation of the intraband PL of HgS CQD. In Figure 2-14**,** the PL emission overlaps the intraband absorption peak. The quantum yield is small, estimated at ~ 10^{-3}-10^{-4}, but it is similar to HgTe quantum dots with

the same interband emission energy.[77] Intraband PL is easily seen in the β-HgS nanocrystals of varying sizes. As shown in Figure 2-15, the PL intensity depends strongly on the surface doping. The S^{2-} treatment quenches the intraband PL, while the Hg^{2+} exposure recovers the PL with a red shift.

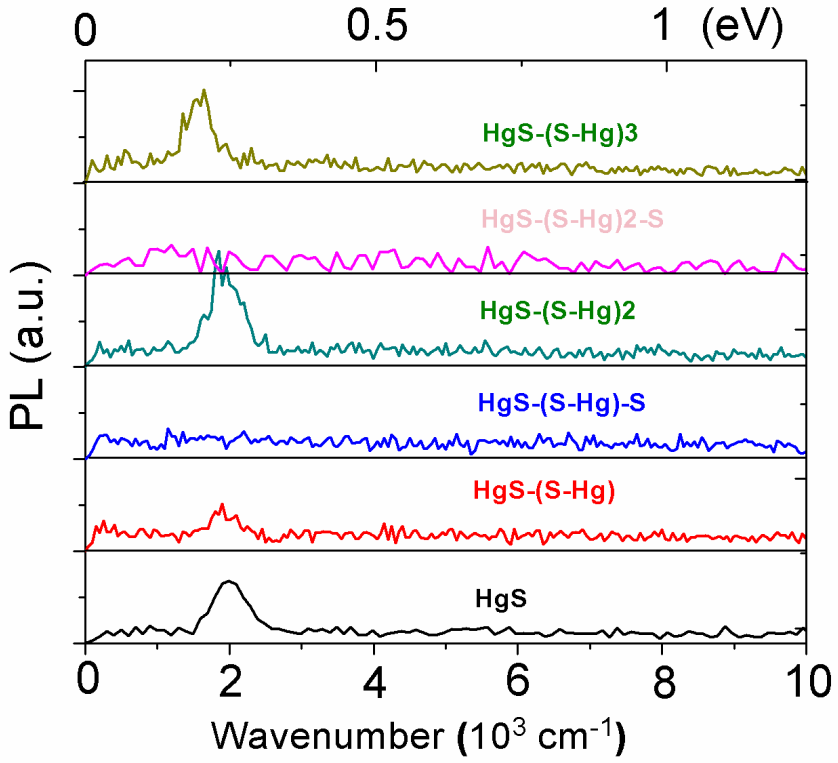

Figure 2-15 Intraband PL is sensitive to surface exposure of Hg^{2+} or S^{2-} solutions. The S and Hg represent the S^{2-} or Hg^{2+} treatment, respectively. The black line corresponds to the PL spectrum of the HgS CQDs before any treatment. The red line corresponds to the Hg^{2+} treated HgS-S, indicating that the intraband transition is recovered and slightly red-shifted. The consecutive sulfur treatment quenches the intraband PL, and then the mercury exposure results in a red-shifted intraband PL (green). The reversible feature of the disappearance and appearance of intraband PL by sulfur and mercury treatment continues.

Interband PL has not been observed with either S^{2-} or Hg^{2+} exposure but only after the growth of a CdS shell. The lack of interband PL with sulfide exposure may be attributed to hole traps (filled electron states above the valence band states). This is the case for other semiconductors

such as CdSe after sulfide treatment. With Hg^{2+} exposure, the $1S_e$ electrons should lead to 2-electron-1-hole Auger processes to also quench the interband PL.

More importantly, intraband photoconduction was realized with HgS CQDs during our study on the HgSe CQDs, which will be discussed in detail in Chapter 3.

2.5 Exclusion of Plasmonic Transitions

It is noted that heavily doped nanocrystals that are not in the strong confinement regime exhibit infrared absorptions that are plasmons.[78] This applies to non-stoichiometric copper chalcogenides,[79] heavily doped Al:ZnO nanocrystals[80] and phosphorous-doped silicon nanocrystals.[81] These plasmonic transitions exhibit no quantum confinement, no clear transfer of oscillator strength, no extensive size tuning, and no luminescence, unlike the intraband transitions and therefore cannot explain the observations on β-HgS nanocrystals studied here, which are strongly confined quantum dots and not in the heavily doped regime. It is also noted that the effects reported here cannot be assigned to some trap state unless such trap states would have many novel properties described above including optical absorption strength on par with interband transitions.

Recently, Shen *et al*[82] in our group developed new dual-phase synthesis of HgS CQDs with an extended size range of 3 – 15 nm, and surface plasmon was observed with larger dots as the intraband absorption peaks shift to as far as 10 μ m and exhibit Lorentzian line shapes. For the smaller ones they behave just like the HgS discussed in this chapter.

2.6 Conclusion

In summary, we have developed a novel and reliable synthesis of β-HgS colloidal quantum dots. This study on β-HgS showed the first CQDs with stable electron occupation in the lowest quantum

state and the first observation of stable intraband luminescence of CQDs in ambient conditions. The surface control of doping is demonstrated by optical, spectroelectrochemical and conductivity studies. This study shows a clear example where the large surface-to-volume ratio in nanomaterials is used advantageously to control the carrier doping. The strong modulation of the doping with alternating anions and cations via layer-by-layer deposition is assigned primarily to energy level shifts of the quantum dot due to a surface dipolar layer.

This stable doping of CQDs is an initial step towards the utilization of their intraband transitions. The observation of intraband PL indicates that the relaxation of $1P_e$ to $1S_e$ is not too fast to be used for infrared photodetection. Later, we successfully demonstrated intraband photodetection with β-HgS CQDs during our study on HgSe, which will be covered in more detail in the following chapter.

Chapter 3 HgSe Colloidal Quantum Dots and Intraband Photodetection

Following the previous work on mercury chalcogenides, HgSe colloidal quantum dots were synthesized, showing similar air-stable n-doping property but with improved monodispersity. In this chapter, we introduce the first application of the intraband transition of doped colloidal quantum dots by demonstrating photoconductivity in the mid-infrared using the $1S_e$-$1P_e$ transition of n-doped HgSe quantum dots.

3.1 HgSe CQD Synthesis and Characterization

HgSe is a bulk semi-metal which has been synthesized before as nanocrystals.[83] In 2003, Kuno *et al*[84] prepared small HgSe clusters at room temperature utilizing a colloidal method involving the phase separation of mercury and selenium precursor in the presence of strong Hg (II) coordinating ligands. The sizes varied between 2 and 3 nm and showed clear excitonic absorption and emission in the visible region. In 2008, Howes *et al*[85] synthesized HgSe quantum dots at room temperature by injecting the TOPSe solution to the mixture of mercury acetate ($Hg(OAc)_2$) and tri-octylphosphine oxide (TOPO) dissolved with ethanol. The HgSe dots vary between 4.9 nm and 6 nm, but they have an aggregation problem at smaller sizes and evolve to tetrahedral at larger sizes. The absorption spectrum was very broad with a featureless tail extending approximately from 2.5 eV to 0.8 eV.

The new synthesis developed in our group is optimized for larger HgSe CQDs. The sizes of HgSe vary between 5-14 nm in diameter and they could exhibit intraband absorption in the 3-6.5 μm range with different reaction time, while the 5-7 nm range gives better size dispersion.

3.1.1 Experimental

HgSe CQD synthesis

12.6 mg of selenourea (0.1 mmol, Aldrich, 98%) was dissolved in 1 ml of oleylamine (Aldrich, 70%) by heating at 180 °C for 2 hours under nitrogen in the glove box, yielding a clear, light brown solution. In the meantime, 27.2 mg of mercury (II) chloride, $HgCl_2$ (0.1 mmol, Aldrich, 99.999%,) was added to 4 ml of oleylamine, and the mixture was heated at 110 °C for about 30 minutes to dissolve the $HgCl_2$ crystal, forming a clear solution. Then the selenourea/oleylamine solution was injected quickly into the mixture, and the mixture turned black immediately. The particles were quite stable in the reaction, even after growing for 12 hours. The final particle size could be controlled by varying the reaction time. To stop the reaction, 8 ml of a "quench solution", which was made of 5% TOP, 10% dodecanethiol and 85% TCE, was added to the reaction mixture. The quenched mixture was precipitated with methanol or ethanol, centrifuged, and the precipitate was cleaned with ethanol, dried in vacuum before it was redispersed in TCE. The product TCE solution was stable and could be stored for months without aggregation.

Sulfide deposition using c-ALD

1 mL of formamide, 50 μL of oleylamine and 150 μL of 0.1 M $(NH_4)_2S$ were added to 1 mL of HgSe CQD solution in tetrachloroethylene. This mixture was stirred for about 5 minutes, and then the HgSe dots were washed twice with formamide to remove excess $(NH_4)_2S$. Then the HgSe CQD solution was ready for the FTIR and other measurements.

Photoluminescence measurement

The cleaned HgSe CQD solution in TCE are transferred into a liquid cell and photo-excited by 808 nm continuous laser chopped at 70 kHz. The photoluminescence is measured with a step-scan FTIR with an MCT detector and a lock-in amplifier. The reported spectra are not corrected for the spectrometer and detector response. Quantum yields are measured with an integrating sphere following reference.[83]

3.1.2 Results and Discussion

All the HgSe CQDs discussed in this chapter are capped with dodecanethiol (DDT) and some OAm and TOP. Later, we found out that HgSe CQDs could also be prepared with good quality without using a quench solution, which yields HgSe dots with only OAm ligands.

During the reaction, several aliquots of different reaction times could be extracted using a syringe with a long steel needle. Here we reported three samples extracted at 1, 4, and 16 minutes after the injection of selenourea into the $HgCl_2$ mixture, denoted as 1 min, 4 min, and 16 min sample, respectively. In that order of increasing that reaction time, the particles have average diameters of 5.5 nm, 5.9 nm and 6.2 nm, respectively. They are all spherical with a narrow size dispersion, as shown in the TEM image in Figure 3-1, which is that of the 16 min sample. The XRD in Figure 3-2 shows that they have the zinc blende crystal structure.

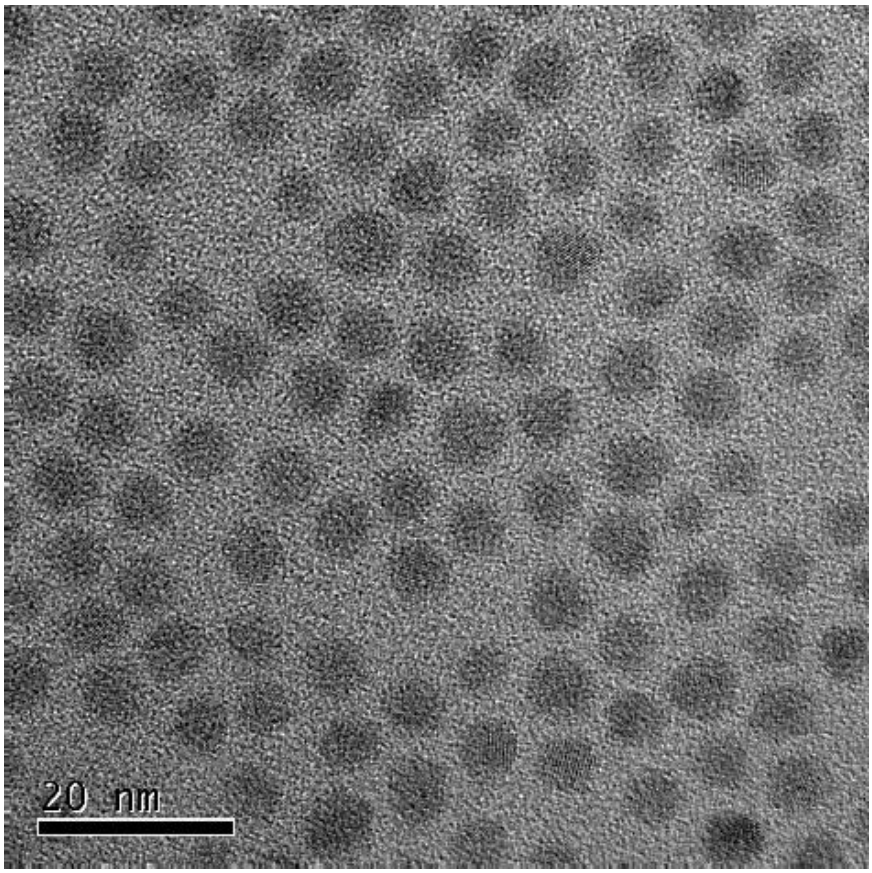

Figure 3-1 TEM image of HgSe CQDs. The average diameter of the particles is 6.2 nm with a standard deviation of 0.76 nm.

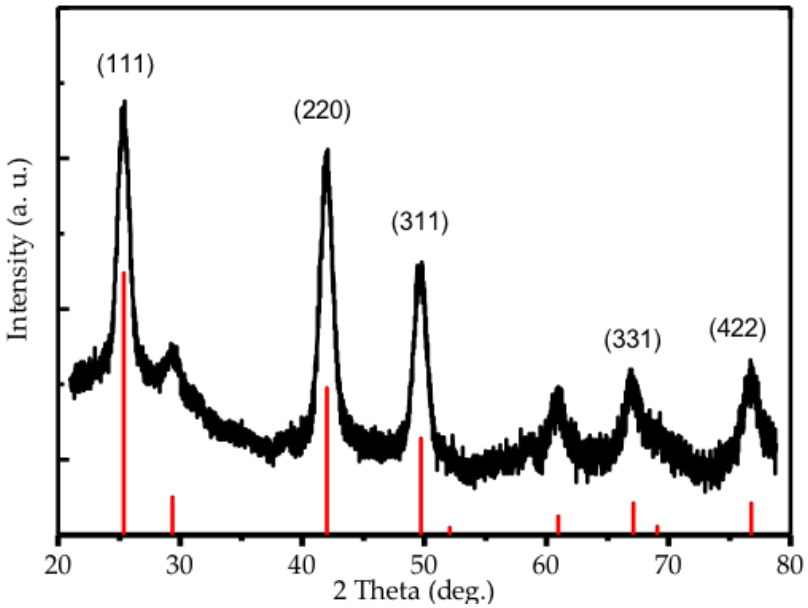

Figure 3-2 The XRD data shows the peaks corresponding to zinc blende HgSe.

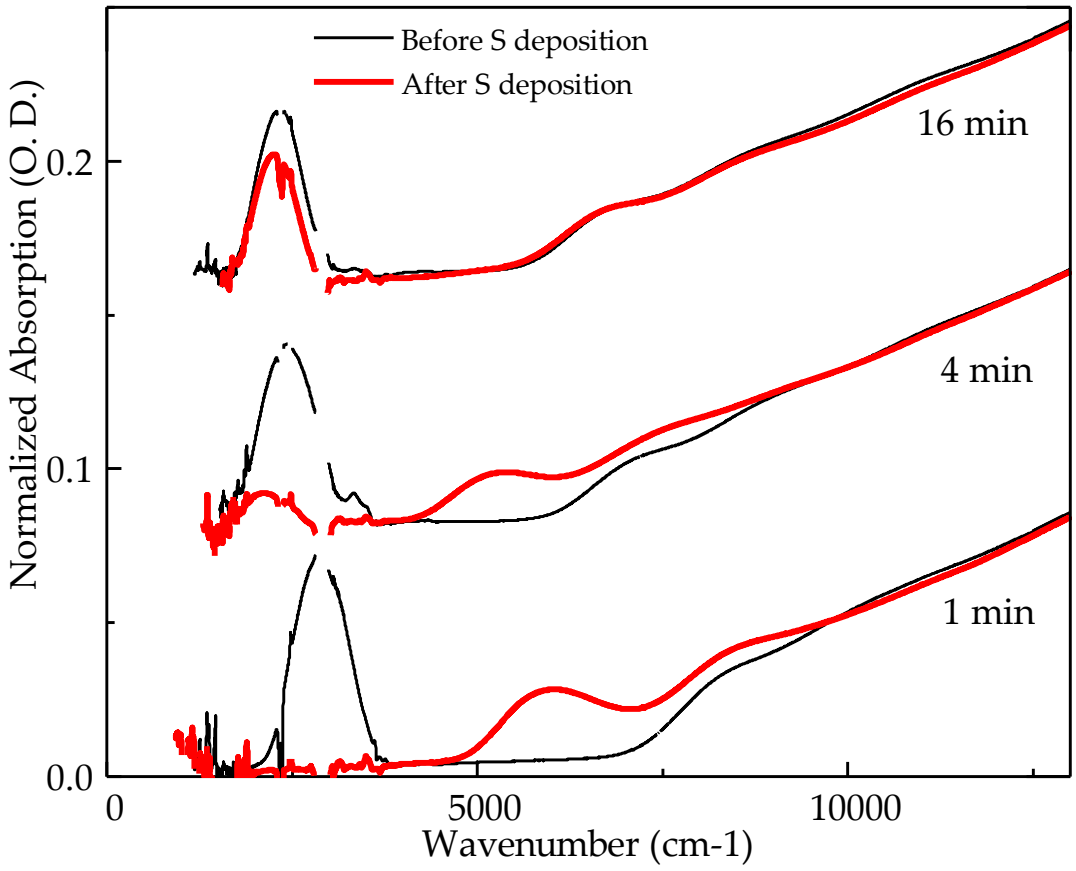

Figure 3-3 Absorption spectra of three samples of different reaction times in TCE, before and after sulfide deposition. The intraband absorptions are around 2500 cm^{-1}, red shifting with longer growth time. The sizes are in order of increasing growth time, 5.5 nm, 5.9 nm and 6.2nm with a standard deviation of ~ 0.7 nm.

The absorption spectra of HgSe CQDs during the course of the reaction are shown in Figure 3-3**.** As prepared, they show the intraband absorption peak around 2000-3000 cm^{-1} indicating stable doping, as well as interband absorption at higher energy. A two-band k·p model gives an intraband energy of 2500 cm^{-1} and an interband energy of 5000 cm^{-1} for 6 nm diameter HgSe quantum dot, which is in good agreement with the spectra and size in Figure 3-3**.**

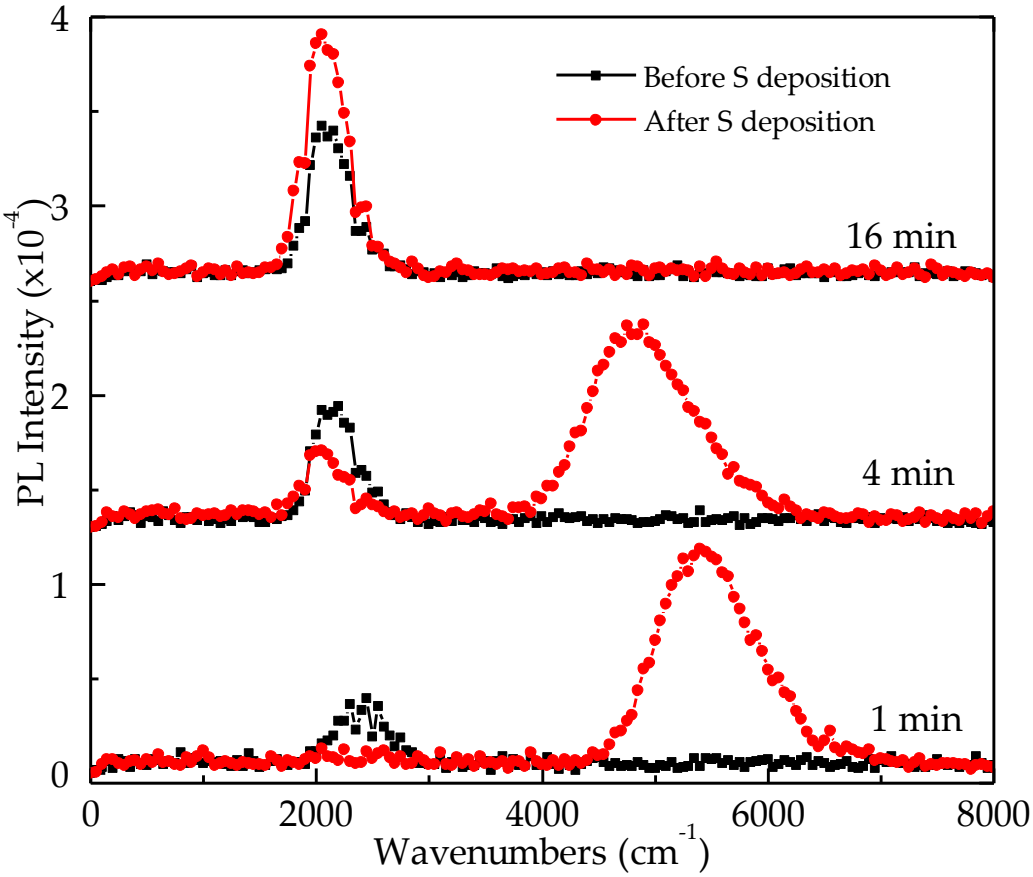

Figure 3-4 Photoluminescence of the samples, before and after sulfide deposition. The interband emission is around 5000 cm-1.

The relative intensities of the intraband and interband absorption vary with different reaction time, indicating different doping levels. It has become appreciated that the surface composition and the ligands of the CQDs allow to tune the absolute energy of the levels and the doping in a given environment.[57, 86-87] The adsorption of sulfide ions,[65] which was previously shown to change the doping level in HgS CQDs,[57] affects the doping of the HgSe CQDs to varying degrees as shown in Figure 3-3. The "1 min" sample starts out with a partially filled $1S_e$ as seen by the small interband absorption at ~5000 cm^{-1} therefore $n < 2$. For the small-sized dots from short reaction time, the sulfides quench fully the intraband absorption, $n = 0$, and the first interband excitonic peak appears. The well-resolved exciton peak reflects the good size control of the HgSe samples.

The "4 min" sample shows no interband absorption around 5000 cm^{-1} so that the $1S_e$ state is full, but it can only be partially un-doped by sulfides as seen by the remaining intraband absorption. The "16 min" sample also has a filled $1S_e$ state but the sulfide has a weaker effect on the intraband and interband absorption suggesting n > 2. This shows that the synthesis produces dodecanethiol-capped HgSe CQDs with a range of doping around n ~ 2. The reproducibility of the synthesis is excellent, and the doping level of sample solutions is stable for weeks in ambient conditions. The systematic investigation of the effects of surface composition and size on the doping level will be a future direction to precisely control the doping.

Figure 3-4 shows the PL of the HgSe samples. The intraband PL is observed around 2500 cm^{-1} in accord with the absorption in Figure 3-3**.** The observation of the intraband PL is significant since it indicates that the $1P_e$ lifetime is not so short. As mentioned earlier, a sub-ps $1P_e$ state lifetime had been obtained in early measurements in CdSe CQDs.[43, 88] The ultrafast relaxation was attributed to an electron-hole Auger relaxation.[89] Later experiments achieved intraband lifetimes as long as 1 ns by removing the hole and reducing the spectral and spatial overlap with ligand vibrations.[90]

Using an integrating sphere, the quantum yield is QY= 1~5 x 10^{-4} over a range of samples. With an estimated $1S_e$-$1P_e$ radiative lifetime of τ_r~ 0.6 microsecond in TCE, the $1P_e$ lifetime $\tau_1 = \tau_r QY$ is estimated to be between 60 and 300 ps. This is within the range of prior results on CdSe quantum dots with the same intraband energy.[90] We note that the quantum yield is similar for the interband PL of dodecanethiol-capped HgTe CQDs at the same energy[77] and this suggests that infrared interband and intraband relaxations in CQDs may be both limited by similar relaxation processes. The intraband emission should be explored further as a potential mid-IR light source. In particular,

under high excitation, it may exhibit lesser Auger quenching than interband emission due to the very sparse density of state.

The PL in Figure 3-4 is affected by the doping level and by electron-hole Auger processes since we used an interband excitation at 808 nm. We propose that at n = 0 ("1 min" sample after sulfide exposure), intraband PL is quenched due to the rapid ~ps electron hole Auger relaxation from $1P_e$ to $1S_e$ while subsequent recombination with the $1S_e$ electron leads to the interband PL. At n=2 ("4 min" sample before sulfide exposure, and "16 min" sample), it is the interband PL that is quenched by a fast trion Auger decay which moves the hole in $1S_e$, where it can radiatively recombine with a $1P_e$ electron to produce intraband PL. Simultaneous interband and intraband PL is sometimes seen, such as in the 4 min sample after sulfide. It is tentatively attributed to subpopulations with n= 0 and n = 2 rather than from dual emission by n = 1.

3.2 k·p model

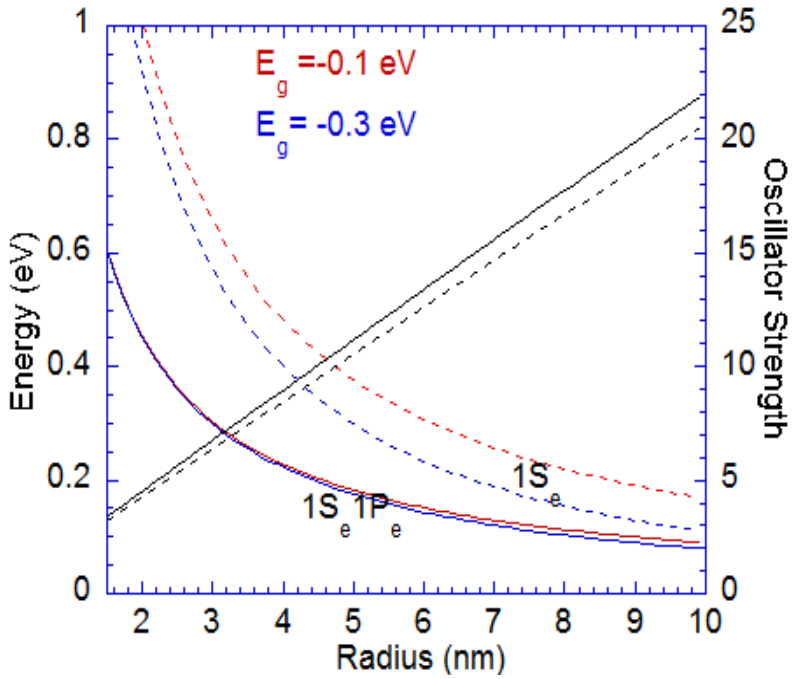

Figure 3-5 Two-band k•p results for the 1Se1Pe transition energy and the oscillator strength.

To investigate the energy vs size relationship for HgSe CQDs, a two-band k·p method[91] is used and the $1S_e1P_e$ transition energy results are shown in Figure 3-5.The Kane parameter is E_p=18 eV and the bulk gap is chosen to be either -0.1 eV (red lines, room temperature) or -0.3 eV (blue lines, low temperature). E_{1Se1Pe} (solid lines) and E_{1Se} (dashed lines) are shown for the two values of negative gap, which shows little effect on E_{1Se1Pe}. For a spherical particle of 6 nm diameter, the model predicts an intraband transition energy of 0.31 eV (~ 2500 cm^{-1}), in good agreement with the experimental result. The temperature dependence of E_{1Se1Pe} is however not explained by this simple model since the change of the gap has apparently little effect.

The oscillator strength of the $1S_e1P_e$ transition[92] (black solid line) is shown as well and it is comparable to that of the interband transition (black dashed line). The oscillator strength is calculated as $f = 2m_0\omega^2 Z_{1S1P}^2$, where m_0 is the free electron mass, ω is the intraband angular frequency, and Z_{1S1P} is the matrix element taken as ~ $<1S|z|1P_z>$ where 1S and $1P_z$ are the envelope functions of the particle in the spherical box. $Z_{1S1P} \sim 0.306R$ where R is the nanoparticle radius. For a 6 nm diameter HgSe QD, the oscillator strength is calculated as 6.7.

The radiative lifetime is estimated as $T_1^{-1} = 2e^2\omega_{1S1P}^2 f n L^2/3m_0c^2$ (CGS units), where here n is now the medium index of refraction (n ~ 1.5 for TCE) and L is the local field factor $L = 3\varepsilon/(\epsilon_{HgSe} + 2\varepsilon)$ where $\epsilon_{HgSe} \sim 15$ and $\varepsilon \sim 2.25$ for TCE. For a 6 nm diameter HgSe QD, the radiative lifetime is 640 ns in TCE.

3.3 Intraband Photodetection

3.3.1 Doping Requirement for Intraband Photoconduction

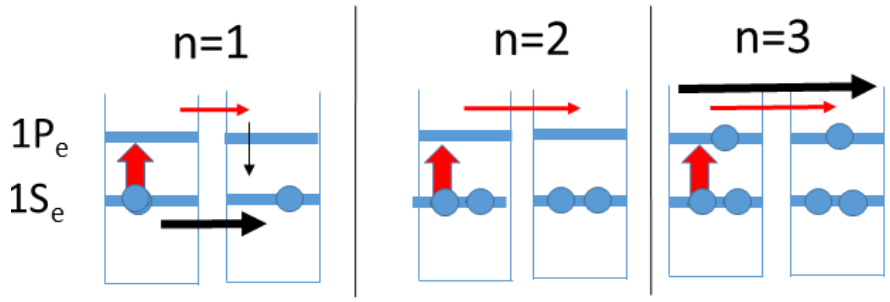

Figure 3-6 Doping requirement for intraband photoconduction. The number of electrons doped in a quantum dot is represented with n. The red horizontal arrow represents the photocurrent, and the black arrow is the dark current. A doping level of n=2 minimizes the dark current.

For photoconduction using the intraband transition between the first two conduction band states $1S_e$ and $1P_e$ of an ideal spherical quantum dot, the dots must be doped with two electrons as shown in the schematic in Figure 3-6. With a partially empty $1S_e$ state, the large dark current through the $1S_e$ states and rapid recombination of the electron in the $1P_e$ states with hole in the $1S_e$ states will prevent any measurable photoconduction. With $1S_e$ full and $1P_e$ partially filled, the large dark current through the $1P_e$ states will also overwhelm the photocurrent. n=2, where n is the doping level per dot, is the best condition as the dark current is minimized[18] and excited electrons in $1P_e$ have a lifetime limited by recombination with the photogenerated "holes" in the $1S_e$ states. In spite of this requirement, weak intraband photoconduction with CQDs has been reported using undoped CdSe nanocrystals dispersed in a conducting organic polymer[93] but the result has not been confirmed.

3.3.2 Experimental

Photoconductance spectra are measured with a standard Nicolet 550 FTIR. The internal light is sent through the external port and focused on the sample with a 5-cm effective focal length parabolic gold mirror. The samples are biased with a 9 V battery in series with a matched resistance. The voltage across the sample is sent to a SR560 AC voltage amplifier with a gain of 200 before being sent back to the FTIR input. A simple schematic of the setup is shown in Figure 3-7.

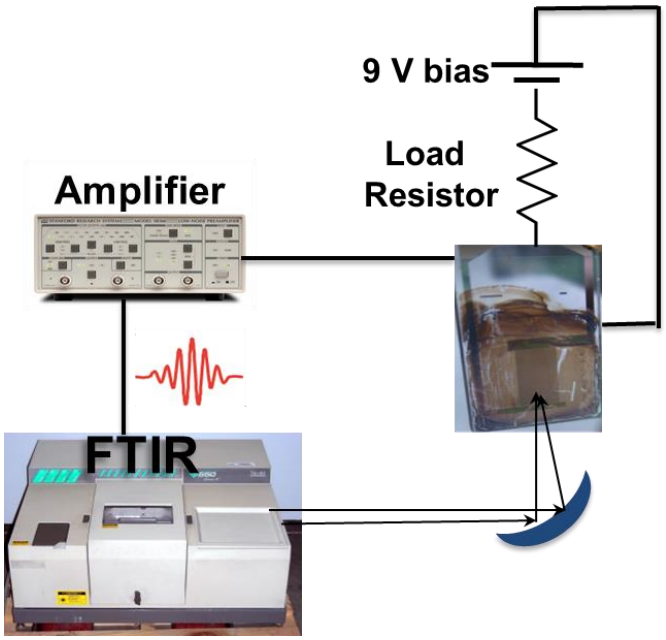

Figure 3-7 Schematic of the setup for photoconductance spectrum measurement.

The responsivity is measured using a calibrated blackbody source, Omega BB4A, at 873 K. A chopper modulates the light up to 600Hz. The sample is inside a cryostat behind a ZnSe uncoated window and ~140mm from the source. A bias of 10V is applied and the current is amplified with a Femto DLPCA-200 before the SR560AC voltage amplifier. The power on the sample is calculated by integrating from 2200 cm^{-1} to 2700 cm^{-1} the blackbody spectrum at 873K, using the

known size of 21 mm diameter of the source and the approximate distance to the sample. This should be accurate within a factor of 2.

For the detectivity, we used the responsivity determined above. For the current noise spectral density measurements, the sample is biased at 10V with the DC amplifier Femto DLPCA-200. The gain is adjusted so that the output is below the maximum output of the DLPCA-200 of 10V. The voltage is then amplified by the SR560AC voltage amplifier at gains between 1 and 100. The voltage noise spectral density $V/Hz^{1/2}$ is obtained directly with a spectrum analyzer, SR760 and its value at 500 Hz is recorded. The sample current noise spectral density is obtained from the voltage noise spectral density by dividing by the total gain.

3.3.3 Results and Discussion

With average ~2 electrons per dot doping level, rather long intraband relaxation, and a narrow size distribution, the HgSe CQDs allow for the first test of intraband photoconduction with doped CQDs.

HgSe CQDs are drop cast on interdigitated electrodes to make films. All the processing is done in air. The films are semi-transparent with an optical density of 0.05 to 0.5 at the intraband peak, and thicknesses between 0.1 and 1 μm. The dried films are insulating (> 40 MΩ) and the films are cross-linked[19, 24, 66] by ethanedithiol to render them conductive. Figure 3-8 shows that the cross-linking does not impact the doping strongly because it is an exchange of thiols. The drop casting and cross-linking are repeated a few times until the film resistance at room temperature is below 100 kΩ.

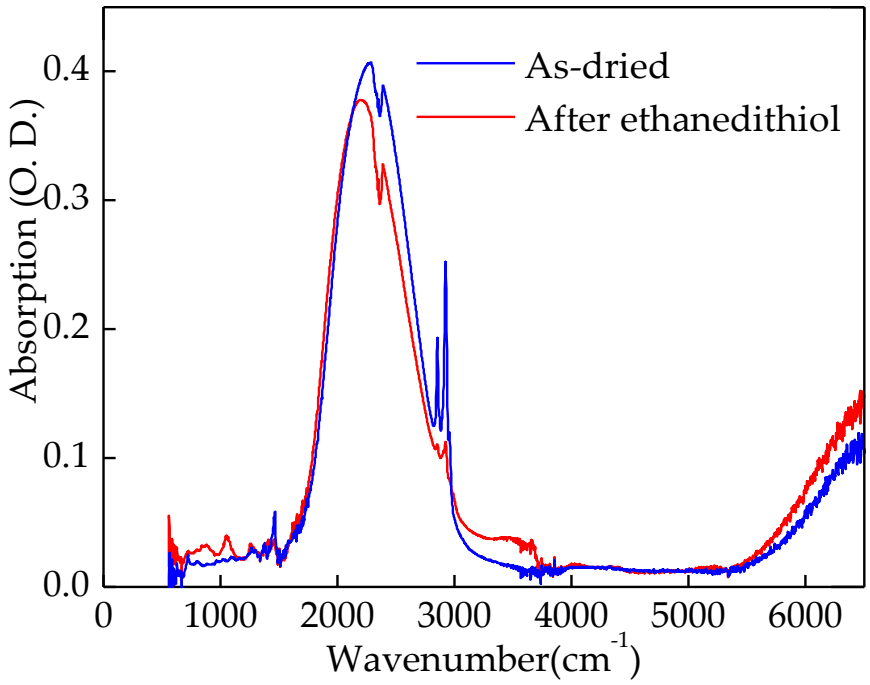

Figure 3-8 Absorption spectra of dodecanethiol-capped HgSe CQDs on a ZnSe ATR window, deposited from hexane: octane solution and dried (blue line), and after cross-linking with ethanedithiol (red line). The doping is only slightly decreased by this ligand exchange. Sharp features are molecular vibrations from CO_2 (2350 cm^{-1}) and H_2O (3600 cm^{-1}) in the beam path, and from CH stretch (2900 cm^{-1}) and bend modes (1500 cm^{-1}) of the ligands.

At 80K, photoconduction spectra are readily obtained. Figure 3-9 shows a photocurrent spectrum taken in ~ 1 second, with very good signal to noise ratio. Figure 3-9 also shows that the intraband photoconduction of HgSe CQDs is narrow compared with the interband response of HgTe CQDs. This narrow spectral response of intraband photodetection may eliminate the need for spectral filters and facilitate color selectivity of the pixels.

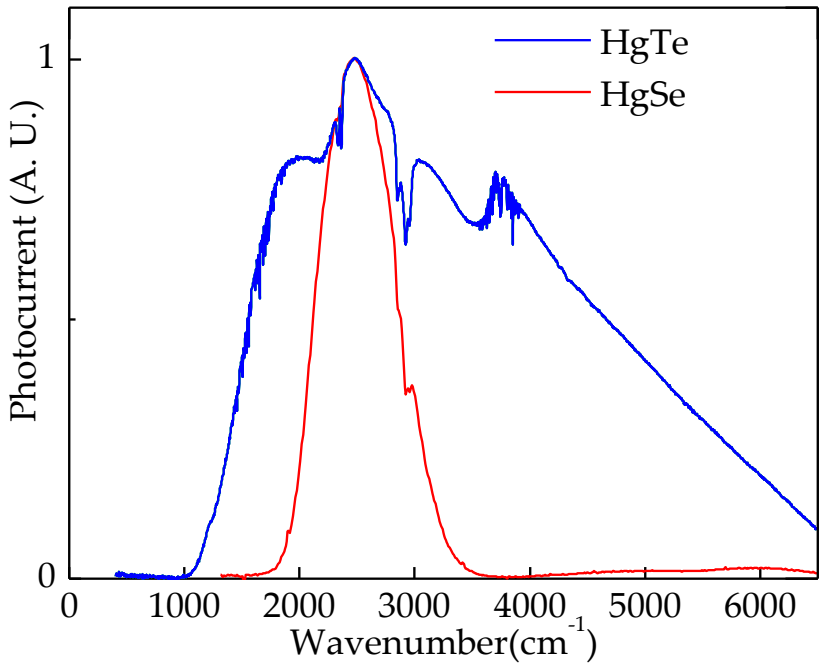

Figure 3-9 Photocurrent spectra of a HgSe film (red line) and a HgTe CQD film (blue line), both at 80K, highlighting the narrow response of the intraband HgSe detector in contrast to the broad response of the interband HgTe.

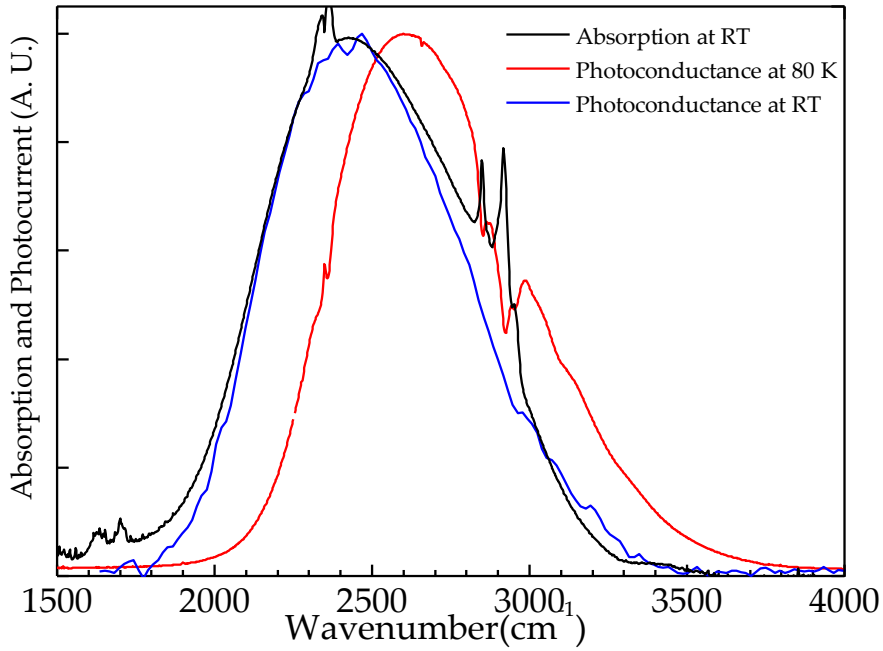

Figure 3-10 Normalized absorption (black line) and photocurrent (blue line) of a HgSe film at room temperature. The photocurrent spectrum at 80K (red line) shows a blue shift of 170 cm^{-1}.

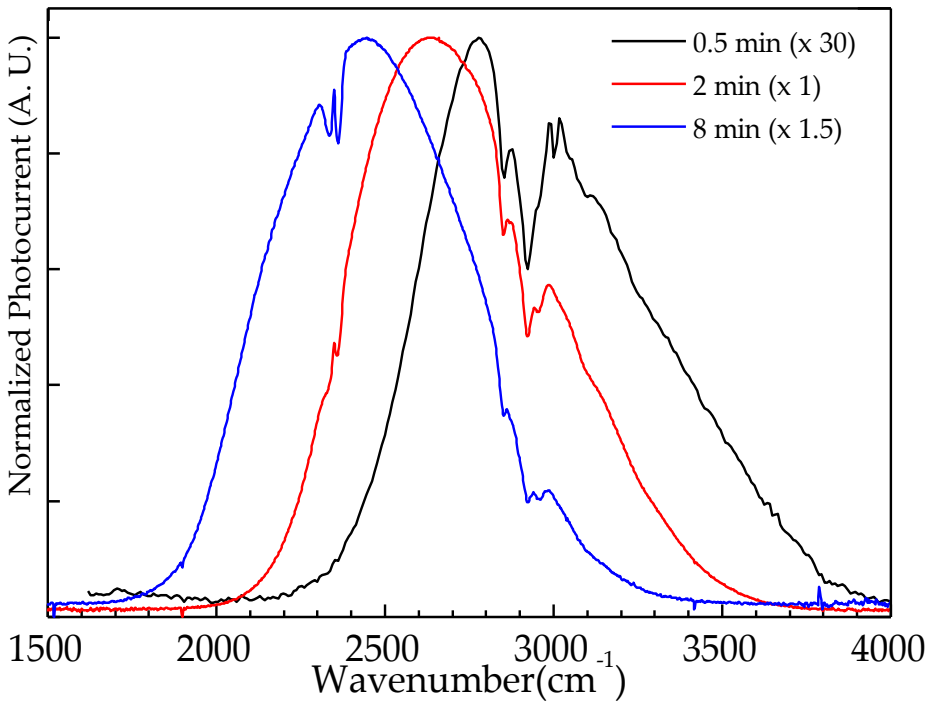

Figure 3-11 Photocurrent with films made with HgSe CQDs at different reaction times, 80K. Photocurrent spectra are measured with a 10V bias.

Figure 3-10 compares the absorption and photocurrent spectra of an HgSe film at room temperature. The absorption is taken with the same CQD sample but with a film made separately on a ZnSe plate and it shows a perfect match with the intraband photoconduction. Figure 3-10 also shows a 170 cm^{-1} blue shift of the intraband photoresponse at 80K. This is typical of all samples and it is interesting as it is opposite to interband HgTe CQDs at similar wavelength which show red-shifts upon cooling.[20] The gaps of bulk HgSe[94] and HgTe[95] become more negative as the temperature is decreased such that the energy of $1S_e$ decreases, and this partly explains the red shift of HgTe CQDs. However, since the $1P_e$ states also red shifts, it was not clear a priori in which direction the $1S_e1P_e$ energy would trend. A two-band k·p model discussed earlier in Section 3.2 predicts essentially no change in the $1S_e1P_e$ energy upon varying the band gap from -0.1 to -0.3

eV and therefore does not explain the blue shift**.** Instead, the temperature shift of the energy gap may be assigned to size-dependent electron-phonon effects.[96-97]

Figure 3-11 shows the photocurrent responses of samples at different reaction times, like those shown in Figure 3-3. Systematically, the best results are for samples in the middle of the size tuning range because those exhibit the lowest dark current. This is consistent with Figure 3-3, where the optimum doping of n ~ 2 is obtained with the "4 min" sample. The size also tunes the spectrum which will affect the energy transfer to the hydrocarbon ligands[90] as it approaches the CH stretch (2900 cm^{-1}) or bend vibrations (1500 cm^{-1}) of the remaining organics but this may be a smaller effect.

As we had synthesized β-HgS CQDs before, which also show n-doping in ambient conditions,[57] we tried to measure its photocurrent. The result was very good: intraband photoconduction was observed as well (Figure 3-12), but it exhibits a lower signal to noise level.

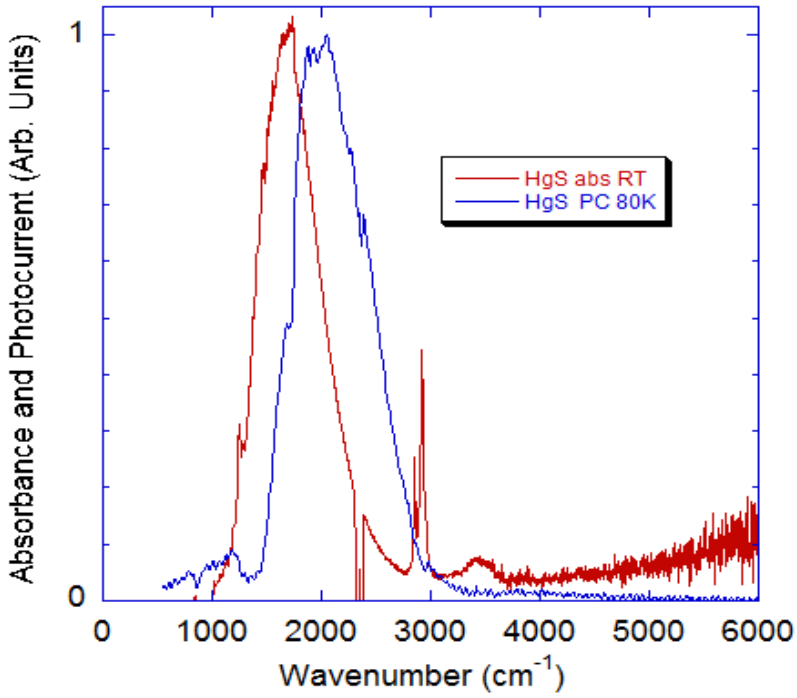

Figure 3-12 Absorption and photocurrent spectra of a HgS CQD film. The absorption spectrum (red line) was taken on a ZnSe ATR window at 300K and exhibits the strong intraband absorption. The photocurrent (PC) spectrum (blue line) was taken at 80K. The HgS samples also exhibited a blue shift of the 80K photocurrent compared to the 300 K absorption. The HgS sample was made by reacting $HgCl_2$ and thioacetamide in oleylamine at 35°C for 10min.

3.4 Electrochemistry

3.4.1 Experimental

For the spectroelectrochemical data shown in Figure 3-13, a hexanedithiol cross-linked HgSe CQD film was dried on a platinum disk for 30 minutes under vacuum and placed into an electrochemical cell. The spectroelectrochemical cell is comprised of three electrodes: an Ag pseudo reference electrode, the Pt working electrode and an Pt counter electrode. Tetrabutylammonium perchlorate (TBAP, 0.1 M) in anhydrous acetonitrile was injected into the electrochemical cell inside the glove box. The electrochemical cell was placed inside of the FTIR,

the Pt electrode was lightly pressed against a CaF_2 window to minimize solvent absorption, and the infrared light reflected from the Pt working electrode was collected by an MCT detector.

For the cyclic voltammetry and conductance data shown in Figure 3-15, the HgSe film were deposited on an interdigitated electrode (CH instruments. Inc. 10 μm width, 5 μm interval, 2 mm length) and cross-linked with ethanedithiol as described above. The samples were immersed in a 0.1 M tetrabutylammonium perchlorate (TBAP) in formamide. A silver wire pseudo-reference and a Pt counter electrode were used. The measurements are done in air. The hopping time is obtained using $\mu = ed^2/6\tau_h kT$ where d is the center to center particle distance taken to be 7 nm.

3.4.2 Results and Discussion

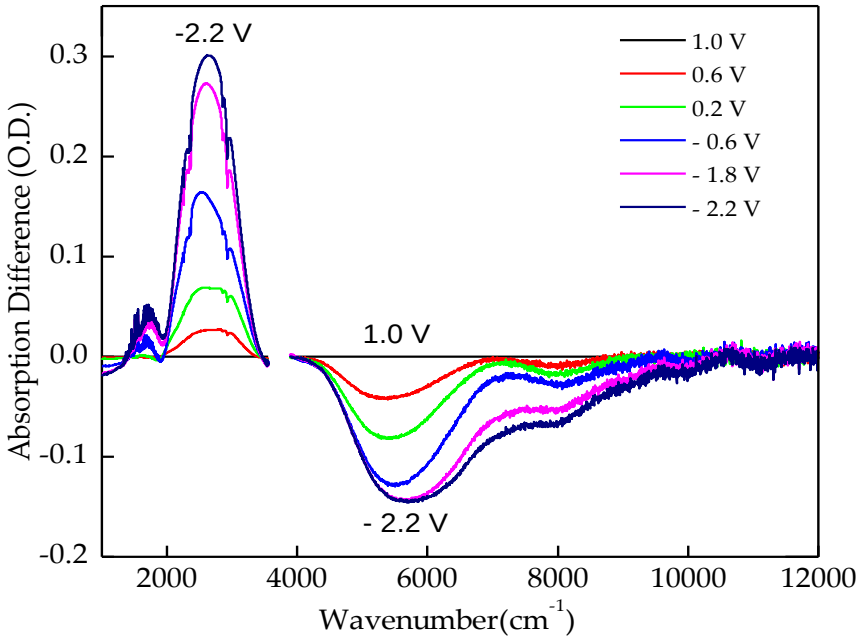

Figure 3-13 Difference absorption spectra of a HgSe CQD film on an evaporated gold slide under electrochemical potential, vs a Ag wire pseudo-reference.

Figure 3-13 shows the difference absorption spectra with the absorption spectrum at +1 V (most oxidizing potential, as the reference), at varying applied biases up to -2.2 V (most reducing). In the reducing direction, the interband absorption is increasingly bleached while the intraband absorption rises, confirming that the HgSe is doped n-type. At the more negative potential, the $1P_e$ state is charged as evidenced by the interband bleach around 8000 cm^{-1}.

The trend is very straightforward in Figure 3-14, where the intensity of the intraband absorption (~ 2650 cm^{-1}), 1Se absorption (~ 5800 cm^{-1}), and 1Pe absorption (~ 8000 cm^{-1}) are plotted against different electrochemical potentials applied.

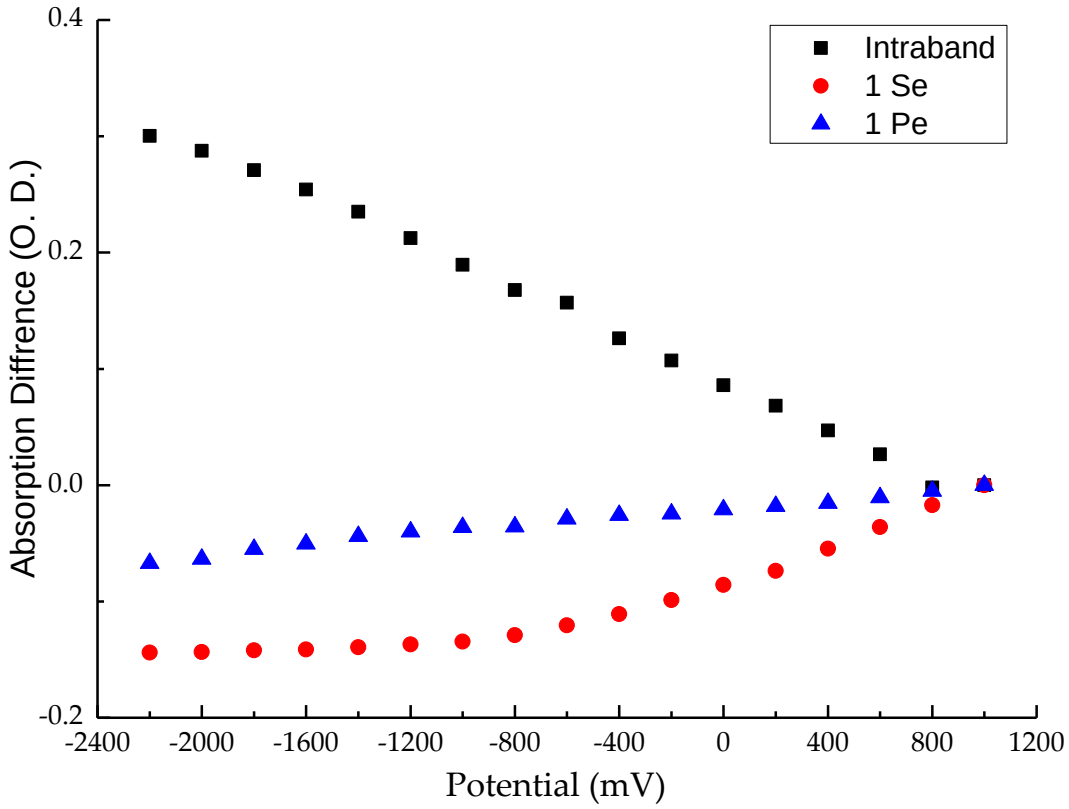

Figure 3-14 Intraband absorption, $1S_e$, and $1P_e$ absorption under different electrochemical potentials.

The mobility of carriers is an important parameter in the discussion of the detector properties. We use electrochemical gating since it can inject many more charges than solid state gating[24] and can separately give the mobility in the $1S_e$ and $1P_e$ states.[66] Figure 3-15 shows the cyclic voltammetry of a film of HgSe CQDs measured with a bipotentiostat. The sequential charging/discharging of the $1S_e$ and $1P_e$ levels appear as reversible peaks in the faradaic (charge injection) current. The conductivity gap between $1S_e$ and $1P_e$ is also clearly evidenced by the dip in the conduction current. A second conductivity gap is seen above $1P_e$ in Figure 3-15 which indicates that the state separation in the HgSe CQDs is very well-defined. The differential mobility gives a higher mobility for $1P_e$ compared to $1S_e$. This was reported for CdSe previously[66] and attributed to a larger density of state and smaller potential barrier. The differential mobility indicates a value of 6.0×10^{-4} cm^2/Vs for the $1P_e$ state. Using the Einstein's relation between mobility and diffusion, a hopping time[66] τ_h ~5 ns is estimated.

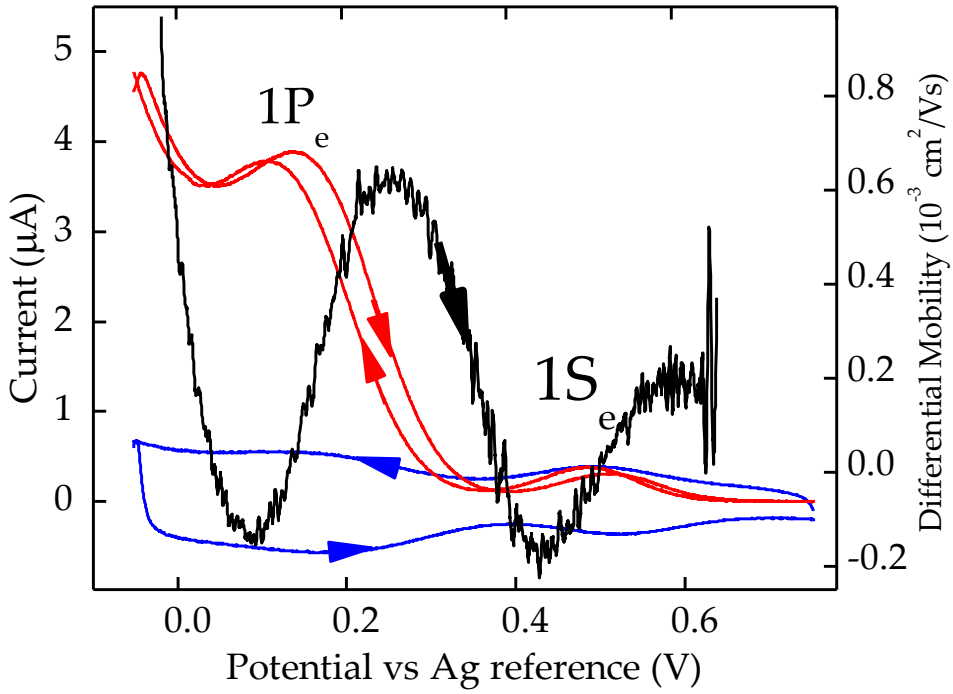

Figure 3-15 Faradaic current (blue line), conduction current (red line) with 10 mV bias, and differential mobility (black line and right axis) of a HgSe CQD film on a platinum interdigitated electrode. The scanning rate is 80mV/s and the electrolyte is formamide with tetrabutylammonium perchlorate (0.1M). The reversible reduction/oxidation peaks around 0.5 V and 0.15V correspond to electron injection into the $1S_e$ state and the $1P_e$ state, respectively. The conduction minimum at ~ 0.35 V occurs when the $1S_e$ state is filled. A second minimum at ~ 0 V is a conductivity gap between $1P_e$ and higher states. The arrows indicate the scanning direction.

3.5 Photodetector Properties

We measured the detecting properties of many films of HgSe CQDs in the middle of the size range. With thin films that are partially absorbing (10-20% at the peak) and with a 10V bias, the responsivity is typically around 5 x 10^{-4} A/W, flat between 50Hz and 600 Hz chopping frequency and changing by less than a factor of two between 300 K and 80 K.

Increasing the bias also increases the responsivity but increases the dark current even more, as the trend shown in Figure 3-16. At 94 V bias, the maximum responsivity obtained is ~ 5 x 10^{-3}A/W and then it starts to saturate, but the dark current increases nonlinearly. By including corrections

for the ZnSe window transmission 70%, and the masking by the electrodes, 60%, the maximum responsivity would be ~ 1.2 x 10^{-2}A/W.

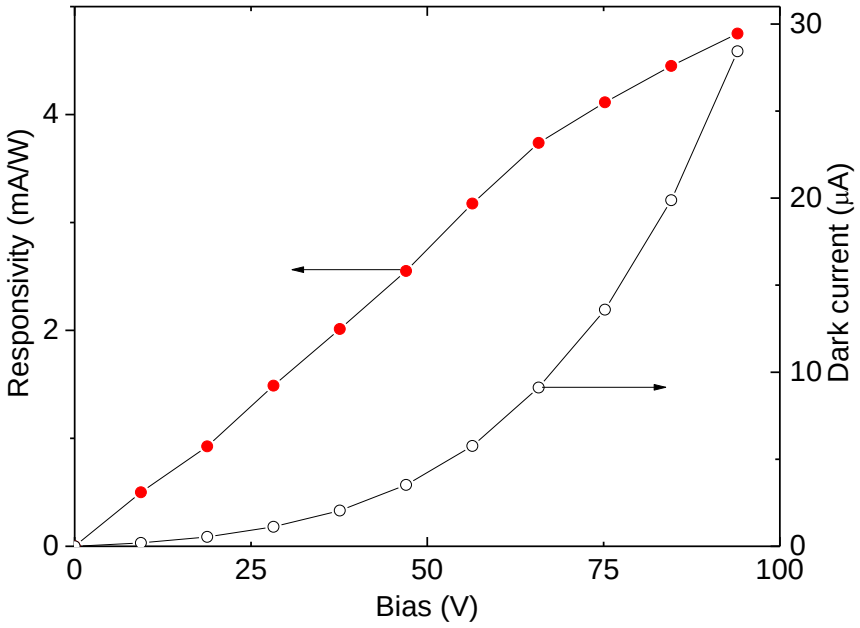

Figure 3-16 Responsivity and dark current for a HgSe CQD film under higher bias at 80K.

The responsivity of a detector is given by $R = \frac{current}{input\ power} = eg\eta/h\nu$ where e is the electron charge, g is the gain, η is defined as the quantum efficiency, h is Planck constant and ν is the light frequency. Assuming unity gain and quantum efficiency, the responsivity at 5 microns should be 2.5 A/W. The typical result of 5 x 10^{-4} A/W at 10 V bias gives η of 2 x 10^{-4} while the responsivity at the highest bias is only about 0.5 % of the ideal responsivity. Part of the reason must be the limited charge separation efficiency associated with the short 1Pe lifetime compared to the hopping time. An estimate of the charge separation efficiency is $\eta \sim \tau_h/(\tau_1 + \tau_h)$ ~ 2-10%. This is higher than measured and suggests that faster recombination centers are present, possibly as defective nanocrystals. Higher responsivity can be obtained by adding gain, but this will not increase the

detectivity. Instead, it will be necessary to investigate alternative cross-linking materials and ligands to increase the $1P_e$ state lifetime and reduce the hopping time.

The detectivity is more sample dependent due to variations in the dark current. The best detectivity at 80K was measured on a sample with a ~ 2250 cm^{-1} detection peak at 80K for which the dark current decreased by a factor of 3200 from 300K to 80K. At 80K and 500Hz, the measured current noise spectral density i_n = 44 $fAHz^{-1/2}$ and close to shot noise limited, while the responsivity was 0.38 mA/W. Using $D^*=A^{1/2}R/i_n$, where i_n is the current noise spectral density and A is the sample area of 1 mm^2, D^*= 8.5 x 10^8 Jones at 500Hz. Correcting for the masking by the electrode where only 60% of the area is active, and the transmission of the uncoated ZnSe window of 70%, leads to a D*=2 x 10^9 Jones with a partially absorbing film (10-20%). Commercial InSb bulk detectors operating at the same wavelength and temperature have D*~10^{11} Jones.

In the shot noise limit of the generation recombination current, the specific detectivity for photoconduction can be written as

$$D^* = \frac{\eta}{h\upsilon\sqrt{\frac{2n_{th}t}{\tau}}} \quad (1)$$

where n_{th} is the thermal carrier density, t is the sample thickness, and τ is the carrier lifetime.[10] It is assumed that the measurement frequency is high enough so that 1/f noise can be neglected. When the noise from the background thermal photon flux Φ dominates, the detector is in the background limited infrared photodetection (BLIP) condition. The BLIP limit is $D^* = \eta/h\upsilon\sqrt{\Phi}$.[10] At 77K, commercial InSb and HgCdTe (MCT) detectors operate close to the BLIP limit, therefore research is aimed at making cheaper detectors, operating at higher temperature, suitable for microfabrication and with higher uniformity from pixel to pixel. Above 77K, the detectivity of InSb and MCT detectors drops because of the increase of the thermal carrier density and also because the carrier lifetime shortens due to the onset of Auger processes.[98]

Using (1), we evaluate the expected D* for our samples. For the carrier density, we use $n_{th} = n'_{th}/V_{NC}$ where n'_{th} is the number of thermal carrier per nanocrystal and V_{NC} is the volume occupied per nanocrystals. At the ideal doping of n=2, n'_{th}= $(N_{1S}N_{1P})^{1/2}exp(-hv/2kT)$, where N_{1S}=2, N_{1P}=6 are the level degeneracy. Assuming purely geminate recombination, the carrier lifetime is $\tau = \tau_1/n'_{th}$, equation (1) becomes $D^* = \eta\sqrt{\tau_1 V_{NC}/2t}/hvn'_{th}$. We use a 5 μm detection wavelength, η= 2 x 10^{-4}, a thickness of 100 nm, τ_1 = 100 ps and V_{NC}= 1.4 x 10^{-18} cm^3. At 300K, n'_{th} = 2.5 x 10^{-2} and D^* = 7.6 x 10^6 Jones. This is in line with the lower signal level at room temperature but we note that, at 300K, the measured detectivity is lower because the noise is already dominated by 1/f noise at 500Hz. At 80K, the calculated carrier concentration per dot drops to 2.9 x 10^{-8} and D^* should correspondingly increase to 6.3 x 10^{11} Jones. This is 300 times better than the best measured value and above the BLIP limit. Part of the discrepancy is that the largest measured drop in the dark current was ~3000 instead of the expected 6 orders of magnitude, and this can be attributed to a deviation from the n = 2 doping. Thus, larger D^* should be possible even with the present materials.

3.6 Performance Perspective

Epitaxial quantum dots photodetectors have been much investigated previously.[12, 99-100] While their performances have improved significantly over the past decade[101-104] they still struggle to match the bulk MCT performances.[11] The first intraband detector demonstrated here with doped CQDs shows already very promising spectral response and operation at room temperature.

It is therefore instructive to evaluate the optimum performance achievable with CQD detectors as done previously for epitaxial quantum dots.[10] In principle, intraband CQDs will allow higher operating temperature because they can circumvent the Auger processes with their sparse density

of states.[10] Although the lifetime is presently limited by non-radiative processes giving rise to the low PL quantum yield discussed earlier, we can expect that future improvements will raise the lifetime. Choosing a detector thickness equal to the absorption length, Einstein's relation between absorption and radiative lifetime gives $\tau_r/t = \lambda^2/8\pi V_{NC}\Delta\nu$ where λ is the wavelength of light and Δν is the resonance width. In the radiative lifetime limit and in the intrinsic regime, the carrier lifetime is $\tau = \tau_r/n'_{th}$. The maximum detectivity becomes

$$D^*_{max} = \frac{c}{4h\nu^{5/2}n'_{th}\sqrt{\pi^{\Delta\nu}/_{\nu}}} \quad (2)$$

where c is the speed of light. The material dependence is only in the thermal carrier density per quantum dot, indicating that undoped interband and doped intraband (n=2) CQDs will have similar D^*_{max}. There may be practical differences in whether it is possible to approach the radiative limit, but the similar PLQY of HgTe interband and HgSe intraband CQDs for the same wavelengths do not yet indicate that this will the case.

Using η=1 and a bandwidth= 20%, the maximum detectivity of a 5 μm intraband CQD detector is then $D^*_{max} = 2.1 \text{ x } 10^{10}$ Jones at 300K which is about an order of magnitude better than microbolometers. CQDs have therefore the potential to be useful for room temperature detection while also allowing fast imaging, cheap fabrication and color specificity and this justifies further investigations of the CQD infrared detectors. The BLIP limit would be reached at ~215K allowing also to reduce the cooling requirements compared to existing semiconductor technology. With non-radiative processes and a non-unity quantum yield of charge separation, the detectivity becomes $D^* = \eta\sqrt{QY}D^*_{max}$. To increase the detectivity, the strategy will be to increase the photoluminescence quantum yield and the charge separation efficiency while maintaining the control on the doping level.

3.7 Conclusion

In summary, we developed a new synthetic method for air-stable n-doped HgSe quantum dots. Our demonstration of intraband photodetection is the first report of photoconduction based on the intraband transitions of doped colloidal quantum dots. So far, HgSe and HgS CQDs are the only ones known to have stable doping in ambient condition now, and they are zero gap or narrow gap, respectively. A broader application of the intraband transitions will require doping carriers in wider bang gap materials, a challenge that may be solved for some systems and in the proper chemical environment using impurity doping[48-50] or charge transfer doping.[53]

A growing interest in HgSe and intraband transitions could be seen. Recent progress in the synthesis of HgSe CQDs has also been reported by Lhuillier *et al*. [105] HgSe nanocrystals were synthesized with a larger size range between 5 and 40 nm, and the synthesis could be scaled up to > 10 g nanomaterials. So, the absorption extended from 3 μm in the mid-IR into the far-IR up to 20 μm. They also studied its performance for IR photodetection using a Wheatstone bridge configuration and achieved detectivity of the order of 10^8 Jones at room temperature, similar to our HgSe-based photodetector operated at liquid nitrogen temperature. The performance enhancement was attributed to the improvement of mobility after ligand exchange with As_2S_3.

Besides the application as photodetectors, HgSe CQDs may lead to an alternative approach to mid-IR light sources because they also exhibit intraband photoluminescence. This advance results from prior progress in the understanding of intraband relaxation, conductivity and doping of colloidal quantum dots, and opens new perspectives for colloidal quantum dots. In contrast to interband transitions of quantum dots, the intraband transition provides a selective spectral detection and it should broaden the range of materials in the search for high performance and affordable infrared detection.

Chapter 4 HgSe/CdS Core/Shell Colloidal Quantum Dots

As discussed in preceding chapters, both air-stable n-doped colloidal HgS[57] and HgSe[58] quantum dots were successfully synthesized in our lab, and they showed intraband optical absorption and photoluminescence in the mid-infrared, along with intraband photoconductivity.[58] Pursuing the development of the intraband transitions with colloidal quantum dots has the potential to significantly extend the candidate pool of solution based materials for high performance and affordable mid-infrared detection and emission. A key issue is that the intraband lifetime is limited by non-radiative processes which results in a low PL quantum yield. Core/shell semiconductor nanocrystals are well known to allow much improvements in PL,[106-109] as well as increased chemical and thermal stability.[110] In principle, in the type-I core/shell system, the photogenerated electron and hole will be confined in the core. In addition, the shell can passivate the surface states of the core and reduce non-radiative recombination pathways.[111] Core/shell structures have been studied extensively, and combinations of various cores and shells have been reported. In an attempt to improve the intraband luminescence of the HgSe core, a CdS shell was grown over the HgSe core. The choice of CdS is motivated by the stability of CdS and the expected type I alignment.[112]

In this Chapter, we report on the synthesis and characterization of these HgSe/CdS quantum dots and the effect of the shell on the n-doping of the original cores and on the optical properties.

4.1 Synthesis and Characterization

4.1.1 Experimental

Synthesis of HgSe Core

Highly monodispersed HgSe QDs were synthesized by slightly modifying a procedure previously described. [58] In a typical synthesis, 0.1 mmol of mercury (II) chloride ($HgCl_2$) was added to 4 mL of oleylamine, mixed and heated at 110 °C to dissolve the $HgCl_2$ crystal. Then a selenourea solution in oleylamine (containing 0.1 mmol of selenourea) was injected quickly into the mixture. The particle size could be controlled by varying the reaction time. The reaction was quenched in ~10 mL of TCE, without using any thiol. The HgSe QDs were cleaned by precipitation with methanol, dried in vacuum, and redispersed in TCE, ready for HgSe/CdS core/shell synthesis.

Synthesis of HgSe/CdS core/shell Quantum Dots

About a quarter of the previous HgSe QD solution in TCE was added to a three-neck round bottom flask, mixed with 4 mL of filtered oleylamine. The flask was then pumped down at 80 ℃ for 30 minutes to remove TCE and air from the system. Then the system was switched to N_2 flow and the reaction mixture was further heated to 100 ℃. H_2S and 0.2 M Cd (oleate) $_2$ were used as S and Cd precursors, respectively. These two precursors were added slowly to the HgSe QD solution alternatively to grow CdS shell. The H_2S was gradually injected above the reaction mixture to make it absorb slowly. The injection speed was also relatively slow to avoid independent nucleation. H_2S was injected every 5 minutes, 0.5 mL at a time. Cd (oleate) $_2$ was added one drop per 30 seconds, which is approximately 0.1 mL every 7 or 8 minutes. Experience showed that excess H_2S was necessary for successful core/shell growth, because not all the H_2S could be used in the reaction. To stop the reaction, a "quench solution" made of 10% oleic acid and 90% TCE,

was added to the reaction mixture. The quenched mixture was precipitated with methanol, centrifuged, and the precipitate was redispersed in TCE.

Optical Measurements

Mid-IR absorption spectra were measured on a Thermo Nicolet Nexus 670 FTIR spectrometer. Near IR spectra were obtained on an Agilent Cary 5000 spectrometer. A liquid cell was used for the colloidal sample. For the drop-cast films, they were deposited on a ZnSe window and their absorption spectra were taken using ATR (attenuated total reflection) method. The photoluminescence was measured with a step-scan FTIR with an MCT detector and a gated integrator. The samples were photoexcited by a 527 nm pulsed laser providing ~ 200 ns pulses at 1 kHz. The PL intensity at different wavelengths are normalized by taking the ratio of the signal from a blackbody source to the calculated blackbody spectrum at its temperature. The PL of different samples are normalized by the absorbed power of the visible laser.

Transmission Electron Microscopy

TEM images were taken on a TECNAI F30 transmission electron microscope with an acceleration voltage of 300 kV. The colloidal samples in TCE solution were deposited on Ted Pella Formvar film-coated copper grids.

X-Ray Powder Diffraction

XRD patterns were taken using a Bruker D8 Powder X-ray diffractometer. Samples were prepared by drop-casting the colloidal solution directly on a cleaned glass slide.

X-Ray Photoelectron Spectroscopy

XPS was obtained under high vacuum (10^{-9}-10^{-8} Torr) using monochromated Al Kα radiation on a KRATOS AXIS Nova X-ray Photoelectron Spectrometer. Thin drop-cast films of colloidal quantum dots were deposited on silicon wafers for measurement.

4.1.2 Discussion on the Synthesis

Our previous HgSe synthetic method included a step of quenching with a DDT solution. But it is difficult for the shell to grow because thiols bind to Hg very tightly. So, we got rid of the ligands other than oleylamine by using a TCE solution to quench the reaction. To grow the shell, the oleylamine-stabilized HgSe quantum dots were cleaned by precipitation, and re-dissolved in TCE.

For the core/shell synthesis, several cadmium precursors, including cadmium chloride, cadmium acetate and cadmium oleate, were tested. When $CdCl_2$ or $Cd(Ac)_2$ was used, no shell growth was observed. Shell growth was observed with $Cd(oleate)_2$. The likely reason is the reduced reactivity of $Cd(oleate)_2$ which prevents independent nucleation of CdS. For sulfur precursors, hydrogen sulfide, bis(trimethylsilyl) sulfide ($(TMS)_2S$), thiourea, thioacetamide were tested. All these four precursors could give core/shell growth when they were used together with $Cd(oleate)_2$ as the Cd precursor. The data shown here are for the core/shell structure grown with $Cd(oleate)_2$ and H_2S. These precursors were added alternatively into the reaction mixture to minimize independent nucleation of CdS.

A layer-by-layer method[65] to grow a CdS shell on HgSe QDs was also attempted, but it typically led to a foggy solution after two or three steps, failing to grow a CdS shell. However, while preparing the paper on the HgSe/CdS core/shell, we learned that Chiluka *et al* managed to grow a CdS shell on HgSe QDs using colloidal atomic layer deposition.[113]

4.1.3 Structure Characterization

Figure 4-1 shows TEM measurements of a core (sample A) and core/shell QDs with increasing shell thickness (samples B, C and D). The average diameter of the HgSe cores is 5.8 nm, and the average diameter of sample B, C and D are 6.8, 7.8 and 8.5 nm, corresponding to 1.8, 3.4 and 4.6

monolayers, respectively. The TEM images show that the lattice fringes extend throughout the whole particle, providing evidence that the growth is epitaxial for these shell thickness.

The core/shell structure is also supported by powder X-ray diffraction in Figure 4-2**.** The XRD patterns of the core/shells are similar to the HgSe cores, but the diffraction peaks gradually shift from zincblende HgSe to zincblende CdS as the shell thickness increases, as expected. The same trend was observed previously in other core/shell systems such as CdSe/CdS[109] and InAs/InP.[114]

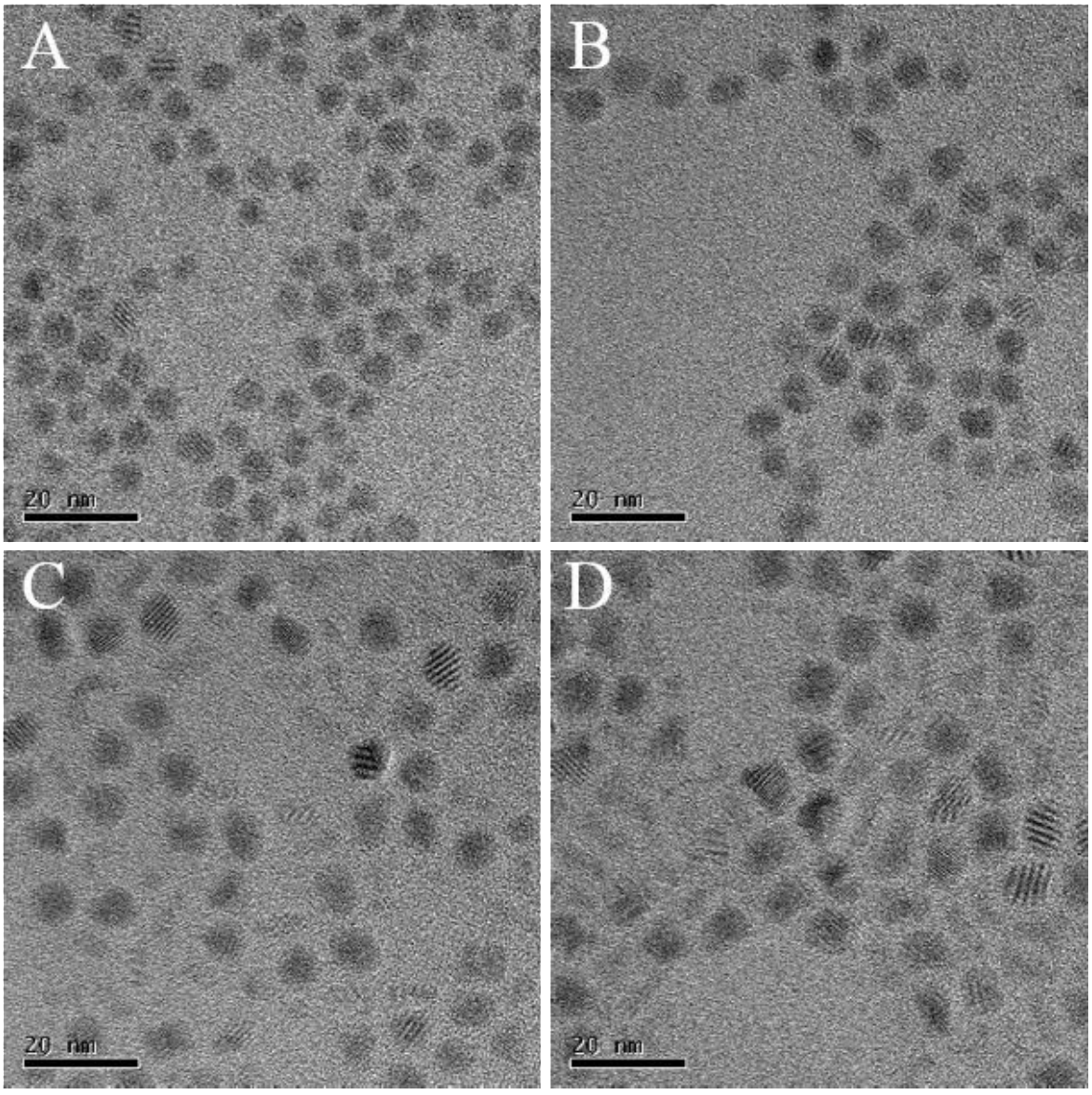

Figure 4-1 TEM images and XRD of HgSe core sample A, HgSe/CdS core/shell samples B, C and D.

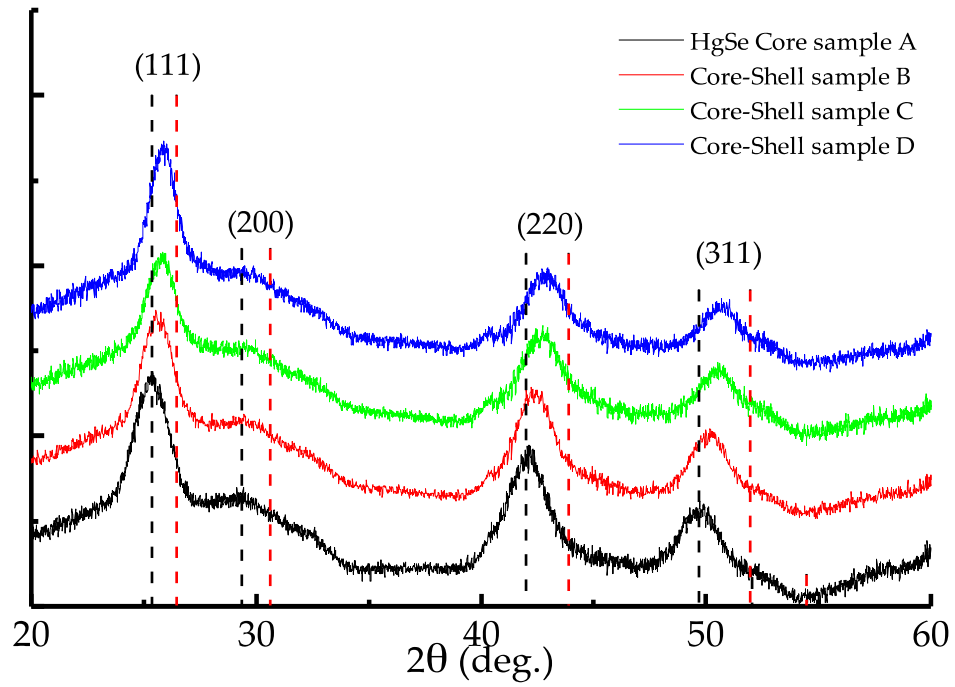

Figure 4-2 XRD of HgSe core sample A, HgSe/CdS core/shell samples B, C and D. The black and red dashed vertical lines represent the XRD pattern of bulk zincblende HgSe and CdS, respectively.

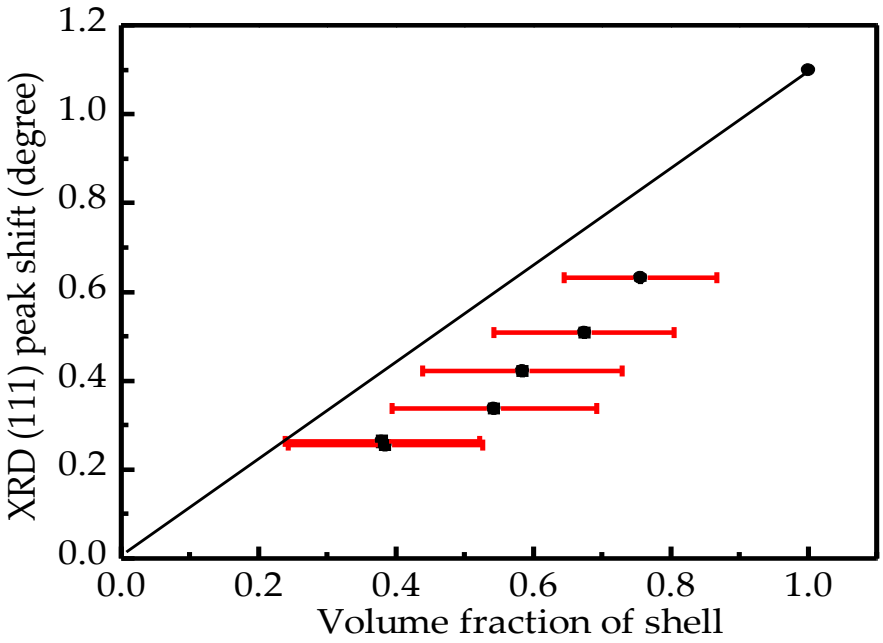

Figure 4-3 The (111) XRD peak shift of HgSe/CdS core/shell samples vs. corresponding volume fraction of the shell in the whole core/shell nanocrystal. Error bars are shown.

The positive correlation between the core/shell XRD pattern shifts and TEM size is shown in Figure 4-3. The (111) XRD peak shifts as the volume fraction of the CdS shells increases. A guide to the eye is provided by a linear volume scaling of the two bulk diffraction peak positions, neglecting strain effects.

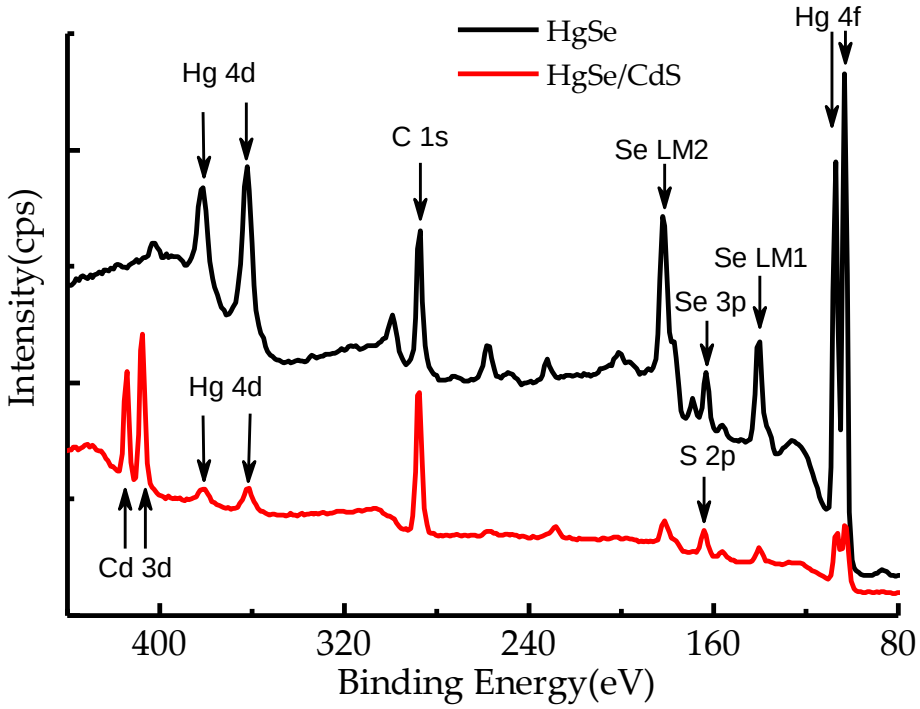

Figure 4-4 XPS spectra of thin drop-cast films of HgSe (black) and HgSe/CdS core/shell nanocrystals (red).

Additional evidence for the shell growth is provided by the X-ray photoelectron spectroscopy (XPS) in Figure 4-4. Data are shown for Samples A and C with diameters of 5.8 and 7.8 nm, respectively. The samples were prepared by drop-casting the colloidal solution directly on a cleaned Si wafer in air at room temperature. A simple comparison between the two spectra reveals the change of elemental composition: in the core/shell sample, both the Hg and Se peaks decrease

significantly, while peaks of Cd and S are clearly apparent where they were absent in the core sample.

When growing shells thicker than 4-5 monolayers, independent nucleation of CdS always occurred. This is likely due to the increased strain arising from the 4.3% lattice mismatch between HgSe and CdS. Thick shell systems with similar lattice mismatch, such as CdS/ZnS[115] and CdSe/CdS,[116] have been successfully grown, and it should therefore be possible to also obtain thicker shells with an improved protocol.

4.2 Optical Properties

The optical absorption spectra of the colloidal HgSe and HgSe/CdS are shown in Figure 4-5, corresponding to sample A and sample C in Figure 4-1**,** respectively. As discussed earlier, the HgSe cores exhibit an intraband transition,[58] shown here as the peak at 2600 cm^{-1}. The spectrum of the HgSe/CdS core/shell, is however very different, rather similar to those of the sulfide modified HgSe.[58] It shows the complete loss of the intraband peak and the recovery of the originally quenched interband absorption with a clearly defined exciton peak at 5300 cm^{-1}. Above that peak, the edge corresponding to the P exciton at ~ 6500 cm^{-1} is preserved and several excitonic structures are observed. The preservation of good optical spectra is consistent with a HgSe/CdS core/shell type I alignment and minimal ripening. As a control, particle growth by Ostwald ripening is observed when the H_2S addition is turned off or not enough H_2S is injected, and TEM images show increased sizes, but the XRD shifts little while the infrared spectra broaden and redshift.

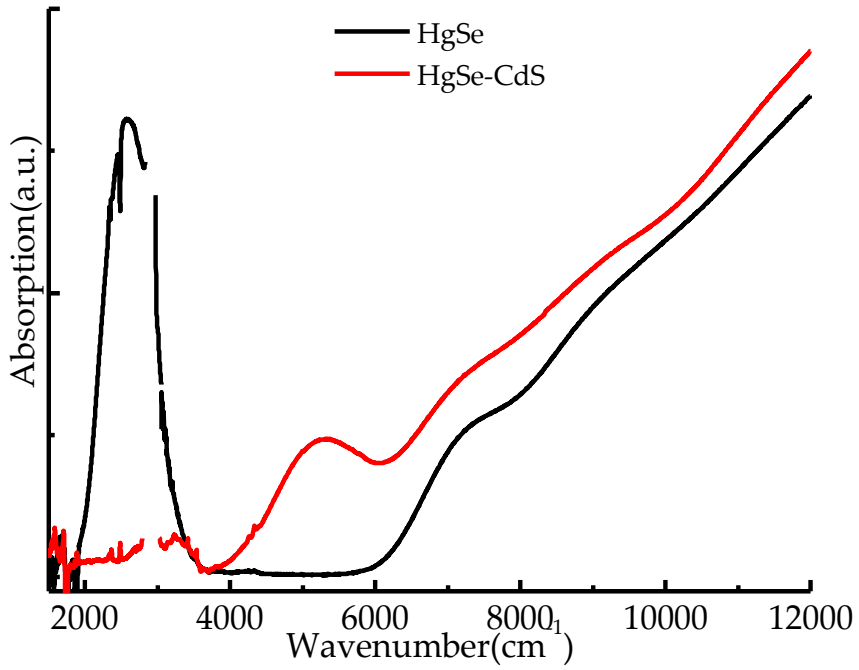

Figure 4-5 Absorption of HgSe colloidal QD cores (black) and HgSe/CdS core/shell nanocrystals (red).

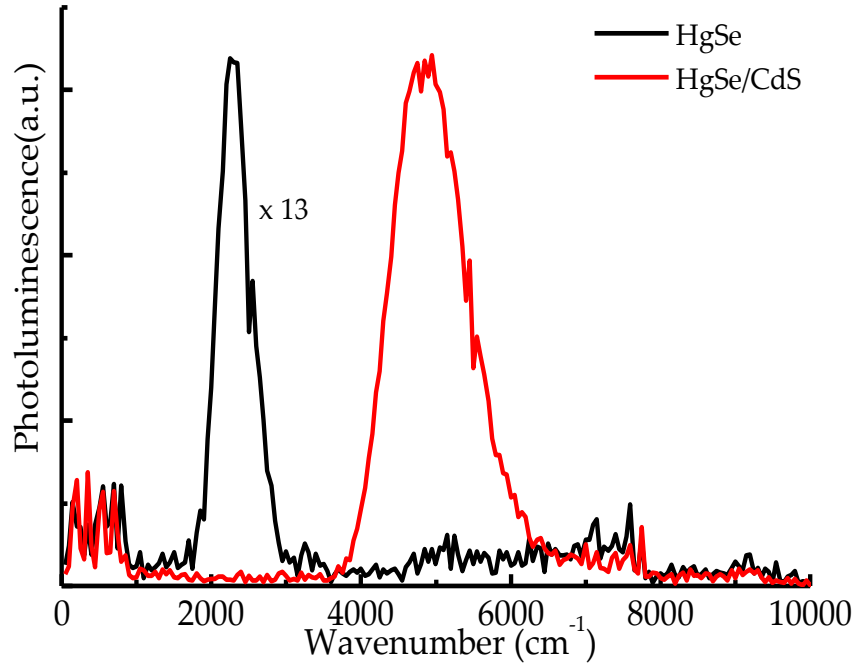

Figure 4-6 PL of HgSe colloidal QD cores (black) and HgSe/CdS core/shell nanocrystals (red).

Figure 4-6 shows that the intraband PL of the HgSe cores at 2300 cm^{-1} is quenched after the shell growth, replaced by a stronger (x13) interband PL peak at 4700 cm^{-1}. Both changes of the absorption and PL therefore indicate that the doping of the original HgSe cores is lost during the shell growth.

To explain the loss of n-doping after the shell growth, we propose two possible answers. The first proposal is from the perspective of chemical composition. Carrier doping in bulk materials is associated with impurities but carriers can be injected from outside for nanocrystals. For HgSe, it is naturally heavily n-doped in the bulk. The high electron densities of 10^{17}-10^{19} cm^{-3} that are achieved depend on the Hg pressure and annealing temperature, and this is attributed to doubly ionized Hg interstitials.[117] In the core HgSe CQDs, the electron concentration of ~ 2 electrons corresponds to a doping density of ~ 2 x 10^{19} cm^{-3}, which is on the high end of the typical doping level of HgSe bulk. When the addition of sulfide on the surface of HgSe CQDs removed the n-doping while the addition of Hg^{2+} led to a recovery of the doping,[58] it could be argued that the surface composition controls the existence of Hg interstitials. In this chemical picture, the loss of n-doping after the growth of the CdS shell could then be assigned to the depletion of the core in Hg interstitials, somehow such that only two electrons are removed which could be interpreted as requiring the removal of only one Hg interstitial.

Another model of doping in nanocrystals we propose is a physical "surface gating"[57] where the doping level is not due to core composition modifications but is affected by the electrostatic environment set up by the surface chemical composition. The following discussion reinforces the relevance of this surface gating.

4.3 Effect of Ligand Exchange and Annealing on Core/Shell Films

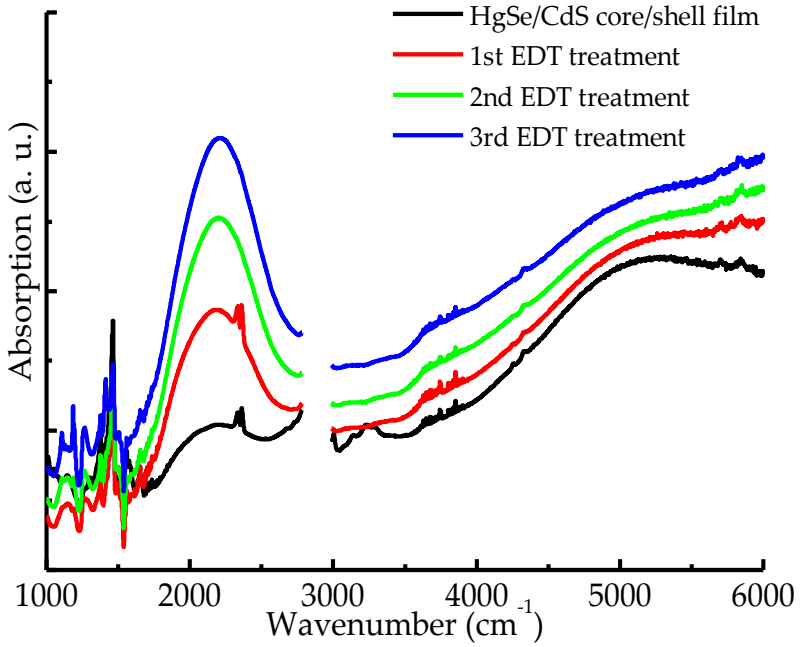

Figure 4-7 Effects of dithiol immersion on the absorption of HgSe/CdS core/shell films. The HgSe/CdS sample is from sample C.

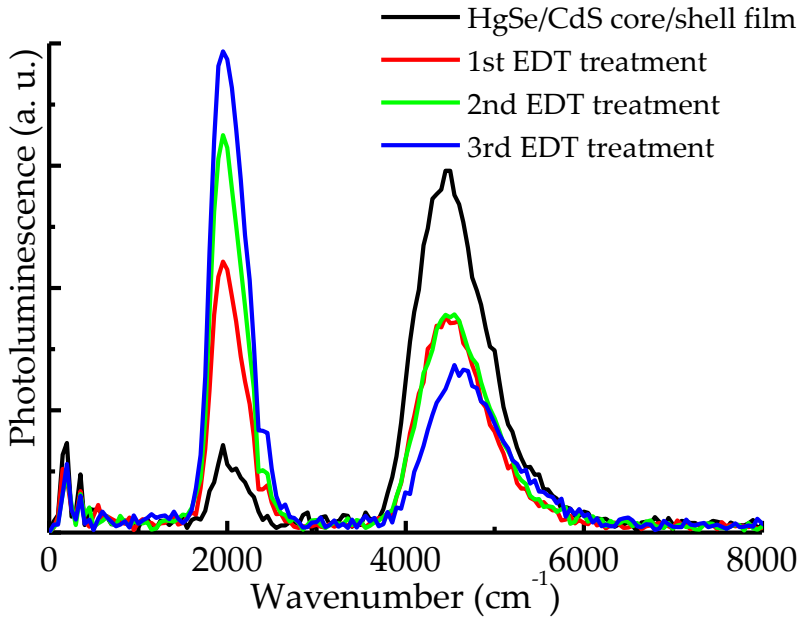

Figure 4-8 Effects of dithiol immersion on the PL of HgSe/CdS core/shell films. The HgSe/CdS sample is from sample C.

When the undoped HgSe/CdS colloids are simply dried as a film, the absorption (Figure 4-7) and PL (Figure 4-8) spectra readily show partial recovery of the n-doping. Upon further ligand exchange with an ethanedithiol (2% in ethanol) solution for 2 min, the recovery is even more significant. As shown in Figure 4-8, repeated immersion of the samples in the solution leads to increasing n-doping and intraband PL. Some of the exciton absorption remains at ~5000 cm^{-1} and the interband PL at 4600 cm^{-1} does not fully disappear, meaning the doping is not fully recovered. Considering that the film-drying or the dithiol/ethanol solution are unlikely to increase the Hg interstitial concentration of the core or to induce any internal modification of the core, surface gating provides a better explanation. We propose that the higher dielectric constant of films, compared to the nonpolar solutions, reduces the charging energy of electrons in the quantum dots, and therefore facilitates doping. As to the recovery of doping with the dithiol ligand, we propose that the Hg-thiolate dipole is pointing towards the core, and therefore stabilizes the electron. Both explanations are qualitative, but they could provide a purely physical starting point to understand the doping sensitivity to surface and environment.

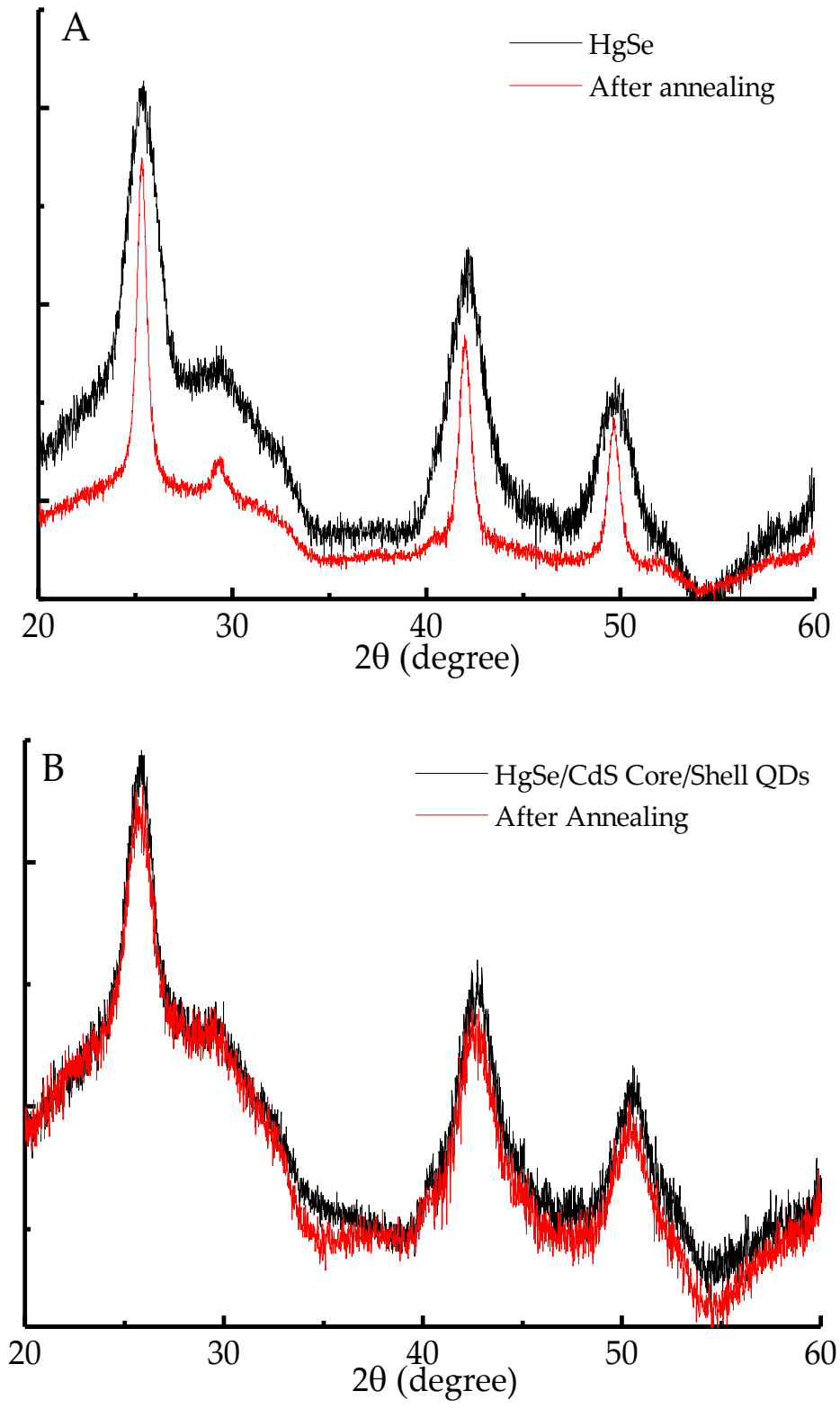

Figure 4-9 XRD patterns of HgSe QDs (A) and HgSe/CdS core/shell QDs (B) before and after annealing at 200 °C for 10 minutes.

Besides the TEM, XRD and XPS evidence presented above for the core/shell structure, a stringent test is the effect of annealing. XRD was measured before and after a thermal annealing at 200°C for the core and core/shell systems. As shown in Figure 4-9A, the peaks for the HgSe CQD film narrowed significantly after annealing, indicating grain growth. Using $0.9\lambda/\beta cos\theta$ for the grain size, the size determined from XRD increased from 4.5 nm to 12 nm, the initial value being close to the 5.8 nm measured by TEM. The facile sintering of the HgSe CQDs limits the temperature range of HgSe CQDs films for infrared applications as well as severely restricts processing conditions. However, as shown in Figure 4-9B, the XRD of the core/shell is unchanged after 14 min at 200°C. Grain growth can also be followed optically.

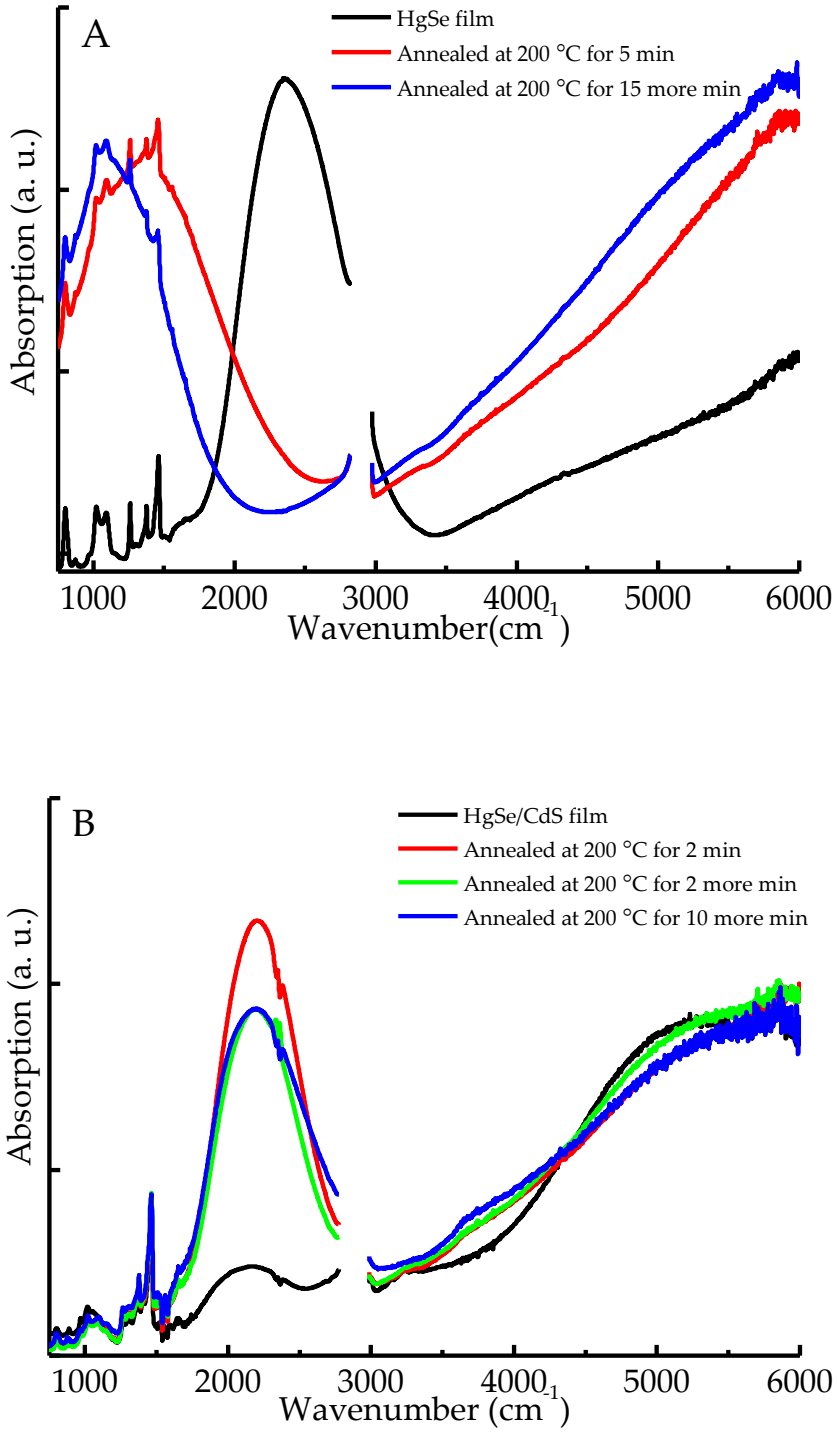

Figure 4-10 Absorption spectra of HgSe CQD film (A) and HgSe/CdS core/shell CQD film (B) before and after annealing. The black spectra represent the absorption or PL of the film before annealing treatment, and the colored spectra represent the absorption or PL after different time of annealing as indicated by the legends. (The HgSe QD is from Sample A, and the HgSe/CdS is from sample B).

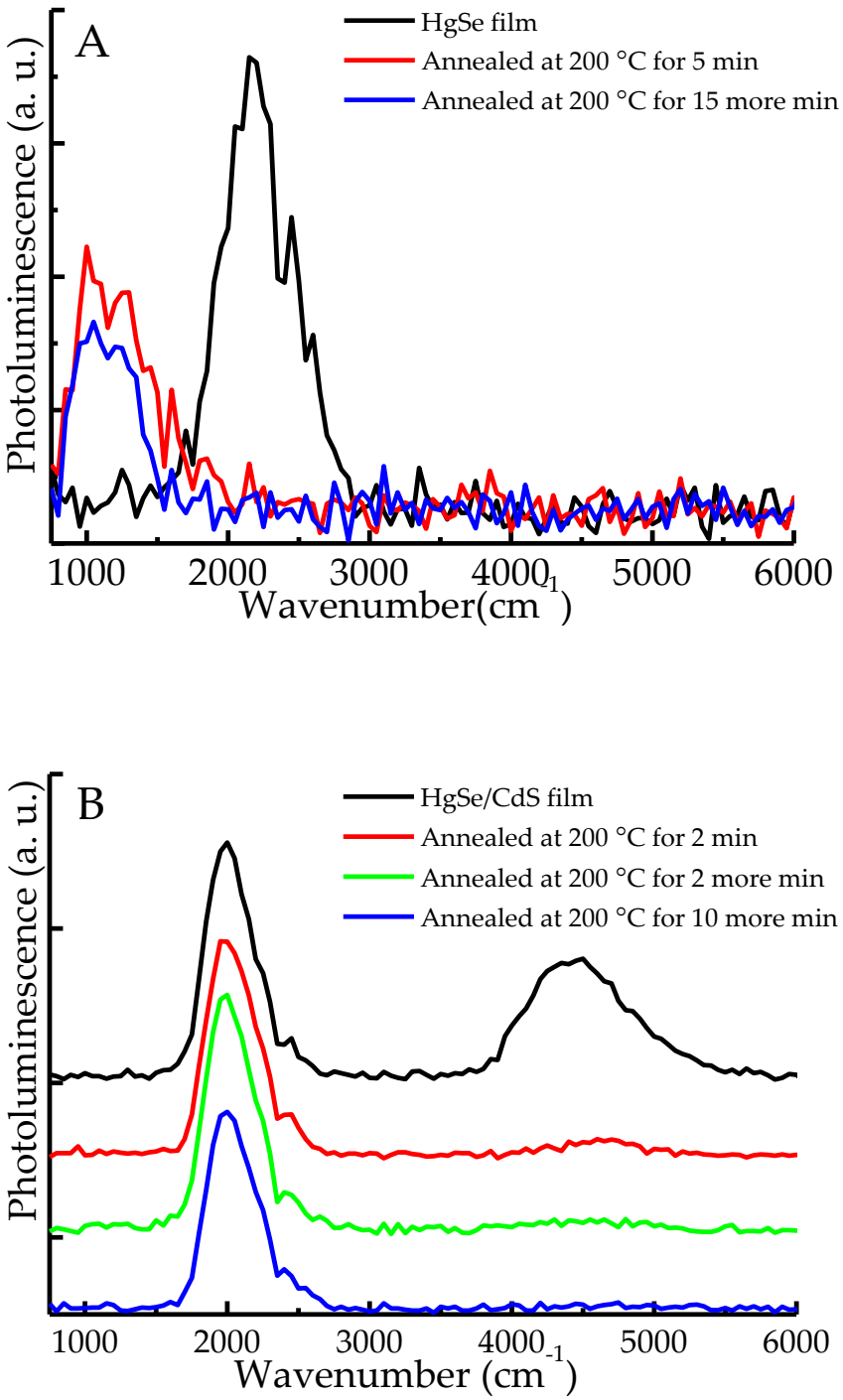

Figure 4-11 PL spectra of HgSe CQD film (A) and HgSe/CdS core/shell CQD film (B) before and after annealing. The black spectra represent the absorption or PL of the film before annealing treatment, and the colored spectra represent the absorption or PL after different time of annealing as indicated by the legends. (The HgSe QD is from Sample A and the HgSe/CdS is from sample B)

The optical spectra shown in Figure 4-10A show that upon heating the HgSe film at 200 ℃ for increasing length of times up to 15 min, the intraband absorption consistently red shifts, moving into the long-wave infrared below 1000 cm^{-1}. The red shift is consistent with the increase in grain size, confirming that HgSe CQD films that are heated for significant time lose quantum confinement, even though n-doping is preserved by the annealing. Figure 4-11A also shows emission appearing at longer wavelength up until the detector cut-off. The emission between 1000 and 1500 cm^{-1} is, however, not assigned to pure PL but instead to a thermal emission of the sample. This is due to the temperature increase induced by laser heating combined with the increased emissivity (= absorption) of the sample in the long wavelength.[118]

For the core/shell, Figure 4-10B shows instead that the intraband peak remains constant upon annealing while its intensity increases after a short annealing time and remain stable for longer annealing. After 14 min annealing at 200°C, the intraband PL retained its position and intensity, while the interband PL dropped to almost zero (Figure 4-11B). Thus, for the core/shell, n-doping is improved further upon annealing and quantum confinement is preserved. The optical properties of core/shell samples were further unchanged for up to 2 hours annealing time at 200°C but they started to show a slow degradation around 250°C.

The other advantage expected from the shell is improved PL. The solution PL, in Figure 4-6, shows an increase of the core/shell but it is not a meaningful comparison since the core/shell PL arises from interband transitions. However, in films, there is a noticeable improvement of the intraband PL with the core/shell. Films of HgSe, HgSe/CdS and HgTe were drop-cast at room temperature and the ligand was exchanged with ethanedithiol. The films had similar optical absorption (> 80%) at 527 nm. As shown in Figure 4-12, the intraband PL of HgSe/CdS films is improved about three folds over the HgSe cores. This improvement is smaller than for core/shell

in the visible spectral range but it is consistent with the expectation of the R^4 dependence for the nonradiative energy transfer rate to surface vibrations.[119] Thicker shell and better uniformity of core/shell should give more enhancement of the intraband PL. Recently, Dr. Jeong in our group observed intraband PL of photoexcited CdSe/ZnSe at 5 microns[120], and it was much stronger than that of CdSe cores, confirming that the intraband PL could indeed be improved by the core/shell strategy.

Lacking a standard IR emitting material at 5 microns, we compared the emission with a film of HgTe QDs.[77] Figure 4-12 shows that the intraband emission of a film of HgSe/CdS is brighter than the interband emission of a film of HgTe of similar optical density, both treated with ethanedithiol. This is reported since there is no prior comparison of interband and intraband emission efficiency in colloidal quantum dots at similar energies.

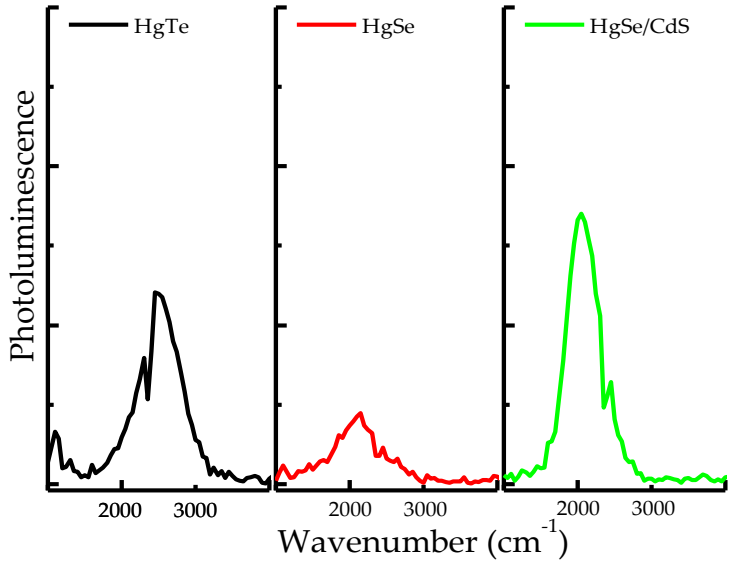

Figure 4-12 PL of HgTe, HgSe, and HgSe/CdS CQD films on CaF_2 substrates.

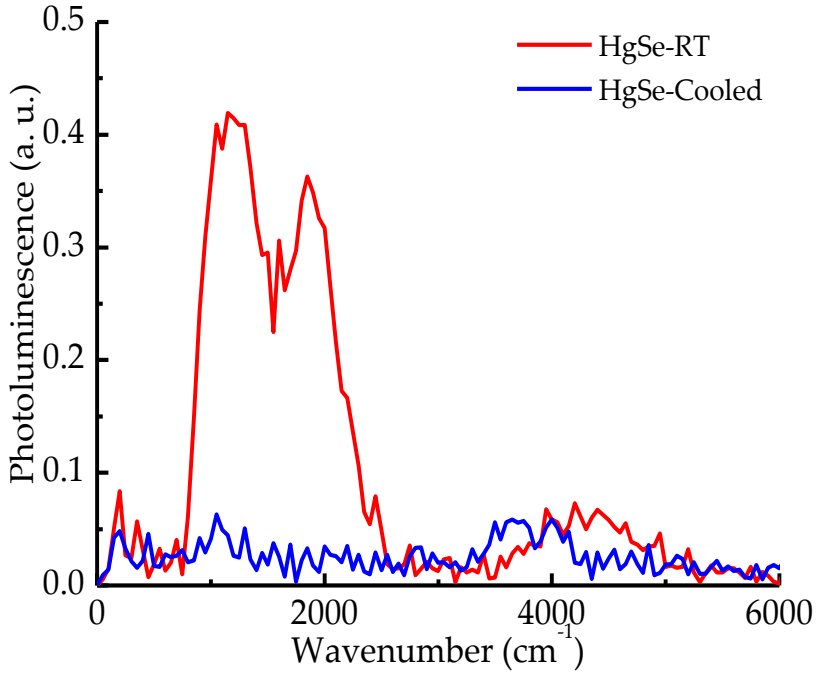

Figure 4-13 PL of annealed HgSe CQD films. The PL spectra were taken with the samples in a cryostat at room temperature (red lines) and at 83K (blue line), respectively. Both films absorbed most (>80%) of the 527 nm laser. The laser power was 67 mW over a spot of 0.5 mm.

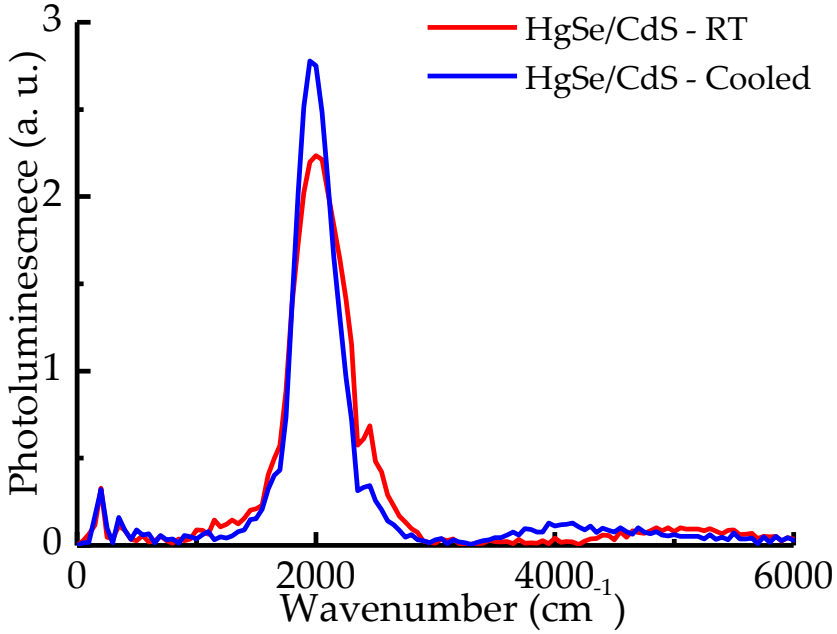

Figure 4-14 PL of annealed HgSe/CdS core/shell CQD films. The PL spectra were taken with the samples in a cryostat at room temperature (red lines) and at 83K (blue line), respectively.

Annealing has also very different effects on the PL spectra of HgSe and HgSe/CdS films. Figure 4-13 shows the emission of a HgSe CQD film after annealing with PL-like peaks from 1000 to 2500 cm^{-1} at room temperature. However, after the film was cooled by liquid nitrogen in a cryostat, the peak disappeared, indicating that they were in fact from thermal emission due to the laser heating. For the HgSe/CdS film after annealing, Figure 4-14 shows that the strong and narrow intraband PL remained strong after the film was cooled by liquid nitrogen, indicating that the emission was true PL. Upon cooling, the line shape narrowed slightly but it was not significantly shifted and its integrated intensity was unchanged. The lack of temperature dependence of the PL intensity indicates that the non-radiative processes have no activation energy. It is noted that there is a weak interband PL at 5000 cm^{-1} at room temperature and ~ 4000 cm^{-1} at low temperature. The large difference of the thermal shift of the interband and intraband transitions was previously discussed.[58] Incorporation of the core/shells in an inorganic matrix and annealing to remove all high frequency vibrational absorptions will be the next step to further improve the PL.

4.4 Conclusion

HgSe/CdS core/shell nanocrystals were synthesized using $Cd(oleate)_2$ and H_2S as Cd and S precursors, respectively. The narrow monodispersity of the cores was well preserved as evidenced by the excitonic features in the optical spectra of the core/shell. TEM, XRD and XPS confirmed the shell growth. The shell led to a small improvement of the PL efficiency and a vastly increased resistance to elevated temperatures where the cores showed no sintering up to 200°C. In the colloidal solution, the CdS shell completely removed the doping and the intraband luminescence, but both were recovered as films. The sensitivity of the doping to the processing justifies future studies taking control of the surface and environment to optimize the doping and intraband

luminescence. Using the core/shell HgSe/CdS, this work showed a first instance of films of n-doped colloidal quantum dots that emit from an intraband transition in a narrow spectral range at five microns, can be optically pumped in the near-IR, and are thermally robust. It can be expected that incorporation into an inorganic matrix will lead to brighter emission and that the mid-infrared intraband emission from such systems will lead to future investigations for mid-IR light source from phosphors to optically pumped lasers.

Chapter 5 Future Perspective

Over the past three decades, research on colloidal quantum dots has seen rapid and tremendous advancement in both theoretical and application study. Most of the research has been focused on their interband transitions, but their intraband transitions associated with bandgap engineering also have great potential and show striking beauty of the quantum confinement effect. The PGS lab started to work on the intraband topic 18 years ago[51] and has produced many influential milestone discoveries in the quantum dot field, including the invention of charge transfer doping,[53-54] the first realization of dot to dot conducting in CdSe CQDs,[66] and the understanding of the role of ligands in electron intraband relaxation[119] among many others. The ultimate goal is to understand the intraband transitions in CQDs and to make useful applications with them. Now, the successful synthesis of air-stable n-doped HgS and HgSe CQDs provides a great opportunity to study the intraband transitions and shows great promise for potential intraband infrared application. But there are still many challenges and problems to address before they can really come into actual use.

Core/shell heterostructure is an important and necessary approach to reduce nonradiative relaxation[106] and increase the thermal stability for the core colloidal quantum dots. As discussed in Chapter 4, I have synthesized HgSe/CdS core/shell CQDs, and it showed improvement of intraband PL compared to the HgSe cores (HgSe/CdSe core/shell was also prepared and it showed similar effect). In the future, the core/shell synthesis needs to be improved to obtain thicker shells and improved uniformity, which should promise more enhancement of the intraband PL.

Inorganic ligand exchange would be another powerful tool to remove the organic ligands and create an inorganic matrix for the HgSe and HgS CQDs. Many different inorganic ligands have been developed in the Talapin group,[121-123] creating a library for inorganic ligand exchange. As_2S_3 is an ideal inorganic matrix because of its infrared transparency. It has been demonstrated to improve the mid-IR detectivity of HgTe CQD photodetector in our group.[39] It has also been used to enhance the near infrared PL efficiency of PbS/CdS[124] core/shell CQDs. I have tried ligand exchange with As_2S_3 as well on both HgSe and HgSe/CdS core/shell, and I observed increased PL, too. It is an ongoing work with preliminary results, but it should be a promising direction.

As shown with mercury chalcogenides discussed in preceding chapters and reported previously,[73, 125] the surface of the CQD is very important and could affect the doping and/or electronic structure of quantum dots. Therefore, accurate and reliable characterization of the surface composition like XPS or EDX (energy dispersive X-ray) would be critical to get a better understanding of the surface and to utilize it to control the doping level of HgS or HgSe CQDs.

In addition, more in-depth optical study is necessary to understand the relaxation process of intraband transitions. The absolute photoluminescence quantum yield of the intraband transitions needs to be measured to understand the $1S_e1P_e$ lifetime and nonradiative relaxation in n-doped CQDs. Time-resolved measurement of the intraband lifetimes should also be carried out, which will give a more trustworthy lifetime compared to the estimated value using quantum yield discussed in Chapter 3. When discussing MCT detectors in Chapter 1, Auger relaxation is cited as the main reason why their performance drop quickly when temperature rises above the cryogenic. It may play an important role in the intraband relaxation in n-doped CQDs as well, even though their density of states is sparser.

References

1. Herschel, W., Experiments on the Refrangibility of the Invisible Rays of the Sun. *Philosophical Transactions of the Royal Society of London* **1800,** *90*, 9.

2. Rogalski, A., History of Infrared Detectors. *Opto-Electronics Review* **2012,** *20* (3).

3. Lhuillier, E.; Keuleyan, S.; Liu, H.; Guyot-Sionnest, P., Mid-IR Colloidal Nanocrystals. *Chemistry of Materials* **2013,** *25* (8), 1272-1282.

4. Rogalski, A., Recent Progress In Infrared Detector Technologies. *Infrared Physics & Technology* **2011,** *54* (3), 136-154.

5. Rogalski, A., HgCdTe Infrared Detector Material: History, Status And Outlook. *Reports on Progress in Physics* **2005,** *68* (10), 2267-2336.

6. Madelung, O., Rössler, U. & Schulz, M., In *II-VI -VII Compd. Semimagn. Compd.* , Vol. III/17B-22A-41B., pp 41B, 1–3.

7. Levine, B. F., Quantum-Well Infrared Photodetectors. *J. Appl. Phys.* **1993,** *74*, 1.

8. Schneider, H.; Liu, H. C., *Quantum Well Infrared Photodetectors: Physics and Applications*. 2006.

9. Levine, B. F.; Choi, K. K.; Bethea, C. G.; Walker, J.; Malik, R. J., New 10 μm Infrared Detector Using Intersubband Absorption In Resonant Tunneling GaAlAs Superlattices. *Applied Physics Letters* **1987,** *50* (16), 1092.

10. Phillips, J., Evaluation of The Fundamental Properties of Quantum Dot Infrared Detectors. *Journal of Applied Physics* **2002,** *91* (7), 4590-4594.

11. Martyniuk, P.; Rogalski, A., Quantum-Dot Infrared Photodetectors: Status and Outlook. *Prog. Quantum Electron.* **2008,** *32*, 89.

12. Pan, D.; Towe, E.; Kennerly, S., Normal-Incidence Intersubband (In, Ga)As/GaAs Quantum Dot Infrared Photodetectors. *Applied Physics Letters* **1998,** *73* (14), 1937-1939.

13. Smith, D. L.; Mailhiot, C., Proposal for Strained Type-II Superlattice Infrared Detectors. *Journal of Applied Physics* **1987,** *62* (6), 2545-2548.

14. Wei, Y.; Gin, A.; Razeghi, M.; Brown, G. J., Advanced InAs/GaSb superlattice Photovoltaic Detectors for Very Long Wavelength Infrared Applications. *Applied Physics Letters* **2002,** *80* (18), 3262-3264.

15. Cervera, C.; Ribet-Mohamed, I.; Taalat, R.; Perez, J. P.; Christol, P.; Rodriguez, J. B., Dark Current and Noise Measurements of an InAs/GaSb Superlattice Photodiode Operating in the Midwave Infrared Domain. *J Electron Mater* **2012,** *41* (10), 2714-2718.

16. Bhattacharya, P.; Ghosh, S.; Stiff-Roberts, A. D., Quantum Dot Opto-Electronic Devices. *Annu. Rev. Mater. Res.* **2004,** *34*, 1.

17. Benisty, H.; Sotomayor-Torres, C. M.; Weisbuch, C., Intrinsic Mechanism for The Poor Luminescence Properties Of Quantum-Box Systems. *Phys Rev B Condens Matter* **1991,** *44* (19), 10945-10948.

18. Rauch, T.; Böberl, M.; Tedde, S. F.; Fürst, J.; Kovalenko, M. V.; Hesser, G.; Lemmer, U.; Heiss, W.; Hayden, O., Near-Infrared Imaging with Quantum-Dot-Sensitized Organic Photodiodes. *Nat. Photonics* **2009,** *3*, 332.

19. Konstantatos, G.; Sargent, E. H., Colloidal Quantum Dot Photodetectors. *Infrared Phys. Technol.* **2011,** *54*, 278.

20. Keuleyan, S.; Lhuillier, E.; Brajuskovic, V.; Guyot-Sionnest, P., Mid-Infrared HgTe Colloidal Quantum Dot Photodetectors. *Nature Photonics* **2011,** *5* (8), 489-493.

21. Ekimov, A. I.; Onushchenko, A. A., Quantum Size Effect in 3-Dimensional Microscopic Semiconductor Crystals. *Jetp Lett+* **1981,** *34* (6), 345-349.

22. Efros, A. L.; Efros, A. L., Interband Absorption of Light in a Semiconductor Sphere. *Sov Phys Semicond+* **1982,** *16* (7), 772-775.

23. Brus, L. E., A Simple-Model for the Ionization-Potential, Electron-Affinity, and Aqueous Redox Potentials of Small Semiconductor Crystallites. *J Chem Phys* **1983,** *79* (11), 5566-5571.

24. Talapin, D. V.; Lee, J.-S.; Kovalenko, M. V.; Shevchenko, E. V., Prospects of Colloidal Nanocrystals for Electronic and Optoelectronic Applications. *Chemical Reviews* **2010,** *110* (1), 389-458.

25. Klimov, V. I., *Nanocrystal Quantum Dots*. 2009.

26. Kovalenko, M. V.; Manna, L.; Cabot, A.; Hens, Z.; Talapin, D. V.; Kagan, C. R.; Klimov, X. V. I.; Rogach, A. L.; Reiss, P.; Milliron, D. J.; Guyot-Sionnest, P.; Konstantatos, G.; Parak, W. J.; Hyeon, T.; Korgel, B. A.; Murray, C. B.; Heiss, W., Prospects of Nanoscience with Nanocrystals. *ACS Nano* **2015,** *9*, 1012.

27. Murray, C. B.; Norris, D. J.; Bawendi, M. G., Synthesis and Characterization of Nearly Monodisperse Cde (E = S, Se, Te) Semiconductor Nanocrystallites. *Journal of the American Chemical Society* **1993,** *115* (19), 8706-8715.

28. Murray, C. B.; Sun, S. H.; Gaschler, W.; Doyle, H.; Betley, T. A.; Kagan, C. R., Colloidal Synthesis of Nanocrystals and Nanocrystal Superlattices. *IBM J. Res. Dev.* **2001,** *45*, 47.

29. Wehrenberg, B. L.; Wang, C. J.; Guyot-Sionnest, P., Interband and Intraband Optical Studies Of PbSe Colloidal Quantum Dots. *J Phys Chem B* **2002,** *106* (41), 10634-10640.

30. Du, H.; Chen, C. L.; Krishnan, R.; Krauss, T. D.; Harbold, J. M.; Wise, F. W.; Thomas, M. G.; Silcox, J., Optical Properties of Colloidal Pbse Nanocrystals. *Nano Letters* **2002,** *2* (11), 1321-1324.

31. Koleilat, G. I.; Levina, L.; Shukla, H.; Myrskog, S. H.; Hinds, S.; Pattantyus-Abraham, A. G.; Sargent, E. H., Efficient, Stable Infrared Photovoltaics Based on Solution-Cast Colloidal Quantum Dots. *Acs Nano* **2008,** *2* (5), 833-840.

32. Wise, F. W., Lead Salt Quantum Dots: The Limit of Strong Quantum Confinement. *Acc. Chem. Res.* **2000,** *33,* 773.

33. Pietryga, J. M.; Schaller, R. D.; Werder, D.; Stewart, M. H.; Klimov, V. I.; Hollingsworth, J. A., Pushing the band gap envelope: Mid-Infrared Emitting Colloidal PbSe Quantum Dots. *Journal of the American Chemical Society* **2004,** *126* (38), 11752-11753.

34. Rogach, A.; Kershaw, S.; Burt, M.; Harrison, M.; Kornowski, A.; Eychmuller, A.; Weller, H., Colloidally prepared HgTe Nanocrystals with Strong Room-Temperature Infrared Luminescence. *Advanced Materials* **1999,** *11* (7), 552.

35. Rogach, A. L.; Harrison, M. T.; Kershaw, S. V.; Kornowski, A.; Burt, M. G.; Eychmuller, A.; Weller, H., Colloidally Prepared CdHgTe and HgTe Quantum Dots with Strong Near-Infrared Luminescence. *Physica Status Solidi B-Basic Research* **2001,** *224* (1), 153-158.

36. Harrison, M. T.; Kershaw, S. V.; Rogach, A. L.; Kornowski, A.; Eychmuller, A.; Weller, H., Wet Chemical Synthesis of Highly Luminescent HgTe/CdS Core/Shell Nanocrystals. *Advanced Materials* **2000,** *12* (2), 123-125.

37. Kovalenko, M. V.; Kaufmann, E.; Pachinger, D.; Roither, J.; Huber, M.; Stangl, J.; Hesser, G.; Schaffler, F.; Heiss, W., Colloidal HgTe Nanocrystals with Widely Tunable Narrow Band Gap Energies: From Telecommunications to Molecular Vibrations. *J. Am. Chem. Soc.* **2006,** *128*, 3516.

38. Keuleyan, S. E.; Guyot-Sionnest, P.; Delerue, C.; Allan, G., Mercury Telluride Colloidal Quantum Dots: Electronic Structure, Size-Dependent Spectra, and Photocurrent Detection up to 12 μm. *ACS Nano* **2014,** *8*, 8676.

39. Lhuillier, E.; Keuleyan, S.; Zolotavin, P.; Guyot-Sionnest, P., Mid-infrared HgTe/As2S3 field effect transistors and photodetectors. *Adv Mater* **2013,** *25* (1), 137-41.

40. Faist, J., *Quantum Cascade Lasers*. Oxford University Press: Oxford, 2013.

41. West, L. C.; Eglash, S. J., First Observation of an Extremely Large-Dipole Infrared Transition Within the Conduction Band Of a GaAs Quantum Well. *Applied Physics Letters* **1985,** *46* (12), 1156-1158.

42. Faist, J.; Capasso, F.; Sivco, D. L.; Sirtori, C.; Hutchinson, A. L.; Cho, A. Y., Quantum cascade laser. *Science* **1994,** *264* (5158), 553-6.

43. Klimov, V. I.; McBranch, D. W., Femtosecond 1P-to-1S Electron Relaxation in Strongly Confined Semiconductor Nanocrystals. *Physical Review Letters* **1998,** *80* (18), 4028-4031.

44. Kambhampati, P., Hot Exciton Relaxation Dynamics in Semiconductor Quantum dots: Radiationless Transitions on the Nanoscale. *J. Phys. Chem. C* **2011,** *115*, 22089.

45. Sambur, J. B.; Novet, T.; Parkinson, B. A., Multiple Exciton Collection in a Sensitized Photovoltaic System. *Science* **2010,** *330*, 63.

46. Semonin, O. E.; Luther, J. M.; Choi, S.; Chen, H. Y.; Gao, J.; Nozik, A. J.; Beard, M. C., Peak External Photocurrent Quantum Efficiency Exceeding 100% via MEG in a Quantum Dot Solar Cell. *Science* **2011,** *334*, 1530.

47. Peterson, M. D.; Cass, L. C.; Harris, R. D.; Edme, K.; Sung, K.; Weiss, E. A., The Role of Ligands in Determining the Exciton Relaxation Dynamics in Semiconductor Quantum Dots. *Annu. Rev. Phys. Chem.* **2014,** *65*, 317.

48. Norris, D. J.; Efros, A. L.; Erwin, S. C., Doped Nanocrystals. *Science* **2008,** *319*, 1776.

49. Mocatta, D.; Cohen, G.; Schattner, J.; Millo, O.; Rabani, E.; Banin, U., Heavily Doped Semiconductor Nanocrystal Quantum Dots. *Science* **2011,** *332* (6025), 77.

50. Sahu, A.; Kang, M. S.; Kompch, A.; Notthoff, C.; Wills, A. W.; Deng, D.; Winterer, M.; Frisbie, C. D.; Norris, D. J., Electronic Impurity Doping in CdSe Nanocrystals. *Nano Lett.* **2012,** *12*, 2587.

51. Guyot-Sionnest, P.; Hines, M. A., Intraband Transitions in Semiconductor Nanocrystals. *Appl. Phys. Lett.* **1998,** *72*, 686.

52. Shim, M.; Shilov, S. V.; Braiman, M. S.; Guyot-Sionnest, P., Long-Lived Delocalized Electron States in Quantum Dots: A Step-Scan Fourier Transform Infrared Study. *J Phys Chem B* **2000,** *104* (7), 1494-1496.

53. Shim, M.; Guyot-Sionnest, P., N-type Colloidal Semiconductor Nanocrystals. *Nature* **2000,** *407*, 981.

54. Wang, C.; Shim, M.; Guyot-Sionnest, P., Electrochromic Nanocrystal Quantum Dots. *Science* **2001,** *291* (5512), 2390-2.

55. Wang, C.; Shim, M.; Guyot-Sionnest, P., Electrochromic Semiconductor Nanocrystal Films. *Applied Physics Letters* **2002,** *80* (1), 4.

56. Mikulec, F. V.; Kuno, M.; Bennati, M.; Hall, D. A.; Griffin, R. G.; Bawendi, M. G., Organometallic Synthesis and Spectroscopic Characterization of Manganese-Doped CdSe Nanocrystals. *Journal of the American Chemical Society* **2000,** *122* (11), 2532-2540.

57. Jeong, K. S.; Deng, Z.; Keuleyan, S.; Liu, H.; Guyot-Sionnest, P., Air-Stable n-Doped Colloidal HgS Quantum Dots. *The Journal of Physical Chemistry Letters* **2014,** *5* (7), 1139-1143.

58. Deng, Z.; Jeong, K. S.; Guyot-Sionnest, P., Colloidal Quantum Dots Intraband Photodetectors. *ACS Nano* **2014,** *8* (11), 11707-11714.

59. Eychmuller, A.; Hasselbarth, A.; Weller, H., Quantum-Sized HgS in Contact with Quantum-Sized CdS Colloids. *Journal of Luminescence* **1992,** *53* (1-6), 113-115.

60. Higginson, K. A.; Kuno, M.; Bonevich, J.; Qadri, S. B.; Yousuf, M.; Mattoussi, H., Synthesis and Characterization of Colloidal β-HgS Quantum Dots. *J. Phys. Chem. B* **2002,** *106,* 9982.

61. Keuleyan, S. Mid-Infrared Mercury Chalcogenide Colloidal Quantum Dots. The University of Chicago, Chicago, Illinois, 2013.

62. Joo, J.; Pietryga, J. M.; McGuire, J. A.; Jeon, S. H.; Williams, D. J.; Wang, H. L.; Klimov, V. I., A Reduction Pathway in the Synthesis of PbSe Nanocrystal Quantum Dots. *Journal of the American Chemical Society* **2009,** *131* (30), 10620-10628.

63. Keuleyan, S.; Lhuillier, E.; Guyot-Sionnest, P., Synthesis of Colloidal HgTe Quantum Dots for Narrow Mid-IR Emission and Detection. *J Am Chem Soc* **2011,** *133* (41), 16422-4.

64. Pourret, A.; Guyot-Sionnest, P.; Elam, J. W., Atomic Layer Deposition of ZnO in Quantum Dot Thin Films. *Advanced Materials* **2009,** *21* (2), 232-235.

65. Ithurria, S.; Talapin, D. V., Colloidal Atomic Layer Deposition (C-Ald) Using Self-Limiting Reactions At Nanocrystal Surface Coupled To Phase Transfer Between Polar And Nonpolar Media. *J Am Chem Soc* **2012,** *134* (45), 18585-90.

66. Yu, D.; Wang, C.; Guyot-Sionnest, P., N-Type Conducting Cdse Nanocrystal Solids. *Science* **2003,** *300* (5623), 1277-80.

67. Shim, M.; Guyot-Sionnest, P., Intraband Hole Burning of Colloidal Quantum Dots. *Physical Review B* **2001,** *64* (24).

68. Liu, H.; Keuleyan, S.; Guyot-Sionnest, P., N- and p-type HgTe Quantum Dot Films. *J. Phys. Chem. C* **2012,** *116*, 1344.

69. Gerischer, H., On the Stability of Semiconductor Electrodes against Photodecomposition. *J. Electroanal. Chem.* **1977,** *82*, 133.

70. Madelung, O., *Semiconductors Basic Data*. 2003.

71. Schooss, D.; Mews, A.; Eychmuller, A.; Weller, H., Quantum-Dot Quantum Well CdS/HgS/CdS: Theory and Experiment. *Phys Rev B Condens Matter* **1994,** *49* (24), 17072-17078.

72. Virot, F.; Hayn, R.; Richter, M.; Van den Brink, J., Engineering Topological Surface States: HgS, HgSe, and HgTe. *Phys. Rev. Lett.* **2013,** *111*, 146803.

73. Kim, D. K.; Fafarman, A. T.; Diroll, B. T.; Chan, S. H.; Gordon, T. R.; Murray, C. B.; Kagan, C. R., Solution-Based Stoichiometric Control over Charge Transport in Nanocrystalline CdSe Devices. *ACS Nano* **2013,** *7*, 8760.

74. Yuan, M.; Zhitomirsky, D.; Adinolfi, V.; Voznyy, O.; Kemp, K. W.; Ning, Z.; Lan, X.; Xu, J.; Kim, J. Y.; Dong, H.; Sargent, E. H., Doping Control Via Moleculary Engineered Surface Ligand Coordination. *Adv. Mater.* **2013,** *25*, 5586.

75. Kim, D. K.; Vemulkar, T. R.; Oh, S. J.; Koh, W. K.; Murray, C. B.; Kagan, C. R., Ambipolar and Unipolar PbSe Nanowire Field-Effect Transistors. *ACS Nano* **2011,** *5*, 3230.

76. Campbell, I. H.; Rubin, S.; Zawodzinski, T. A.; Kress, J. D.; Martin, R. L.; Smith, D. L.; Barashkov, N. N.; Ferraris, J. P., Controlling Schottky Energy Barriers in Organic Electronic Devices Using Self-Assembled Monolayers. *Physical Review B* **1996,** *54* (20), 14321-14324.

77. Keuleyan, S.; Kohler, J.; Guyot-Sionnest, P., Photoluminescence of Mid-Infrared HgTe Colloidal Quantum Dots. *J. Phys. Chem. C* **2014,** *118*, 2749.

78. Scotognella, F.; Della Valle, G.; Kandada, A. R. S.; Zavelani-Rossi, M.; Longhi, S.; Lanzani, G.; Tassone, F., Plasmonics in Heavily-Doped Semiconductor Nanocrystals. *European Physical Journal B* **2013,** *86* (4), 154.

79. Zhao, Y.; Pan, H.; Lou, Y.; Qiu, X.; Zhu, J.; Burda, C., Plasmonic Cu2–xS Nanocrystals: Optical and Structural Properties of Copper-Deficient Copper (I) Sulfides. *J. Am. Chem. Soc.* **2009,** *131*, 4253.

80. Buonsanti, R.; Llordes, A.; Aloni, S.; Helms, B. A.; Milliron, D. J., Tunable Infrared Absorption and Visible Transparency of Colloidal Aluminum-Doped Zinc Oxide Nanocrystals. *Nano Lett.* **2011,** *11*, 4706.

81. Rowe, D. J.; Jeong, J. S.; Mkhoyan, K. A.; Kortshagen, U. R., Phosphorus-Doped Silicon Nanocrystals Exhibiting Mid-Infrared Localized Surface Plasmon Resonance. *Nano Lett.* **2013,** *13*, 1317.

82. Shen, G.; Guyot-Sionnest, P., HgS and HgS/CdS Colloidal Quantum Dots with Infrared Intraband Transitions and Emergence of a Surface Plasmon. *The Journal of Physical Chemistry C* **2016,** *120* (21), 11744-11753.

83. Kershaw, S. V.; Susha, A. S.; Rogach, A. L., Narrow Bandgap Colloidal Metal Chalcogenide Quantum Dots: Synthetic Methods, Heterostructures, Assemblies, Electronic and Infrared Optical Properties. *Chem Soc Rev* **2013,** *42* (7), 3033-87.

84. Kuno, M.; Higginson, K. A.; Qadri, S. B.; Yousuf, M.; Lee, S. H.; Davis, B. L.; Mattoussi, H., Molecular Clusters of Binary and Ternary Mercury Chalcogenides: Colloidal Synthesis, Characterization, and Optical Spectra. *J. Phys. Chem. B* **2003,** *107* (24), 5758.

85. Howes, P.; Green, M.; Johnston, C.; Crossley, A., Synthesis and Shape Control of Mercury Selenide (HgSe) Quantum Dots. *Journal of Materials Chemistry* **2008,** *18* (29), 3474-3480.

86. Oh, S. J.; Berry, N. E.; Choi, J. H.; Gaulding, E. A.; Paik, T.; Hong, S. H.; Murray, C. B.; Kagan, C. R., Stoichiometric Control of Lead Chalcogenide Nanocrystal Solids to Enhance Their Electronic and Optoelectronic Device Performance. *ACS Nano* **2013,** *3*, 2413.

87. Brown, P. R.; Kim, D.; Lunt, R. R.; Zhao, N.; Bawendi, M. G.; Grossman, J. C.; Bulovic, V., Energy Level Modification in Lead Sulfide Quantum Dot Thin Films through Ligand Exchange. *ACS Nano* **2014,** *8*, 5863.

88. Guyot-Sionnest, P.; Shim, M.; Matranga, C.; Hines, M., Intraband Relaxation In Cdse Quantum Dots. *Physical Review B* **1999,** *60* (4), R2181-R2184.

89. Efros, A. L.; Kharchenko, V. A.; Rosen, M., Breaking the Phonon Bottleneck in Nanometer Quantum Dots: Role of Auger-Like Processes. *Solid State Commun.* **1995,** *93* (4), 281.

90. Pandey, A.; Guyot-Sionnest, P., Slow Electron Cooling in Colloidal Quantum Dots. *Science* **2008,** *322*, 929.

91. Lhuillier, E.; Keuleyan, S.; Guyot-Sionnest, P., Optical Properties of HgTe Colloidal Quantum Dots. *Nanotechnology* **2012,** *23* (17), 175705.

92. Khurgin, J., Comparative-Analysis of the Intersubband Versus Band-to-Band Transitions in Quantum-Wells. *Applied Physics Letters* **1993,** *62* (12), 1390-1392.

93. Stiff-Roberts, A. D.; Lantz, K. R.; Pate, R., Room-Temperature, Mid-Infrared Photodetection in Colloidal Quantum Dot/Conjugated Polymer Hybrid Nanocomposites: A New Approach to Quantum Dot Infrared Photodetectors. *J. Phys. D: Appl. Phys.* **2009,** *42*, 234004.

94. Dobrowolska, M.; Dobrowolski, W.; Mycielski, A., Temperature Study of Interband Γ6 →Γ8 Magnetoabsorption in HgSe. *Solid State Commun.* **1980,** *34*, 441.

95. Man, P.; Pan, D. S., Infrared Absorption in HgTe. *Phys Rev B Condens Matter* **1991,** *44* (16), 8745-8758.

96. Olkhovets, A.; Hsu, R. C.; Lipovskii, A.; Wise, F. W., Size-dependent temperature variation of the energy gap in lead-salt quantum dots. *Physical Review Letters* **1998,** *81* (16), 3539-3542.

97. Dey, P.; Paul, J.; Bylsmaa, J.; Karaiskaj, D.; Luther, J. M.; Beard, M. C.; Romero, A. H., Origin of the Temperature Dependence of the Band Gap of Pbs and Pbse Quantum Dots. *Solid State Commun.* **2013,** *165*, 49.

98. Chang, Y.; Grein, C. H.; Zhao, J.; Sivananthan, S.; Flatte, M. E.; Liao, P. K.; Aqariden, F., Carrier Recombination Lifetime Characterization of MBE-Grown HgCdTe. *Appl. Phys. Lett.* **2008,** *93*, 192111.

99. Berryman, K. W.; Lyon, S. A.; Segev, M., Mid-Infrared Photoconductivity in InAs Quantum Dots. *Applied Physics Letters* **1997,** *70* (14), 1861-1863.

100. Sauvage, S.; Boucaud, P.; Brunhes, T.; Immer, V.; Finkman, E.; Gerard, J. M., Midinfrared Absorption and Photocurrent Spectroscopy of InAs/GaAs Self-Assembled Quantum Dots. *Appl. Phys. Lett.* **2001,** *78*, 2327.

101. Stiff, A. D.; Krishna, S.; Bhattacharya, P.; Kennerly, S. W., Normal-Incidence, High-Temperature, Mid-Infrared, InAs-GaAs Vertical Quantum-Dot Infrared Photodetector. *IEEE J. Quantum Electron.* **2001,** *37*, 1412.

102. Chakrabarti, S.; Stiff-Roberts, A. D.; Su, X. H.; Bhattacharya, P.; Ariyawansa, G.; Perera, A. G. U., High-Performance Mid-Infrared Quantum Dot Infrared Photodetectors. *J. Phys. D: Appl. Phys.* **2005,** *38*, 2135.

103. Lim, H.; Tsao, S.; Zhang, W.; Razeghi, M., High-Performance Quantum-Dot Infrared Photodetectors Grown on InP Substrate Operating at Room Temperature. *Appl. Phys. Lett.* **2007,** *90*, 131112.

104. Wu, J.; Shao, D. L.; Dorogan, V. G.; Li, A. Z.; Li, S. B.; DeCuir, E. A.; Manasreh, M. O.; Wang, Z. M.; Mazur, Y. I.; Salamo, G. J., Intersublevel Infrared Photodetector with Strain-Free GaAs Quantum Dot Pairs Grown by High-Temperature Droplet Epitaxy. *Nano Lett.* **2010,** *10*, 1512.

105. Lhuillier, E.; Scarafagio, M.; Hease, P.; Nadal, B.; Aubin, H.; Xu, X. Z.; Lequeux, N.; Patriarche, G.; Ithurria, S.; Dubertret, B., Infrared Photodetection Based on Colloidal Quantum-Dot Films with High Mobility and Optical Absorption up to THz. *Nano. Lett.* **2016,** *16* (2), 1282-6.

106. Hines, M. A.; Guyot-Sionnest, P., Synthesis and Characterization of Strongly Luminescing ZnS-Capped CdSe Nanocrystals. *Journal of Physical Chemistry* **1996,** *100* (2), 468-471.

107. Cao, Y. W.; Banin, U., Growth and Properties of Semiconductor Core/Shell Nanocrystals with InAs Cores. *J. Am. Chem. Soc.* **2000,** *122*, 9692.

108. Cumberland, S. L.; Hanif, K. M.; Javier, A.; Khitrov, G. A.; Strouse, G. F.; Woessner, S. M.; Yun, C. S., Inorganic Clusters as Single-Source Precursors for Preparation of CdSe, ZnSe, and CdSe/ZnS Nanomaterials. *Chem. Mater.* **2002,** *14*, 1576.

109. Reiss, P.; Bleuse, J.; Pron, A., Highly Luminescent CdSe/ZnSe Core/Shell Nanocrystals of Low Size Dispersion. *Nano Lett.* **2002,** *2*, 781.

110. Guo, W.; Li, J. J.; Wang, Y. A.; Peng, X., Luminescent CdSe/CdS Core/Shell Nanocrystals in Dendron Boxes: Superior Chemical, Photochemical and Thermal Stability. *J. Am. Chem. Soc.* **2003,** *125*, 3901.

111. Reiss, P.; Protière, M.; Li, L., Core/Shell Semiconductor Nanocrystals. *Small* **2009,** *5*, 154.

112. Nethercot, A. H., Prediction of Fermi Energies and Photoelectric Thresholds Based on Electronegativity Concepts. *Physical Review Letters* **1974,** *33* (18), 1088-1091.

113. Chiluka, L. K. S. G., P.; Walravens, W.; Hens, Z. In *Core-Shell Nanocrystals by C-ALD Approach in the Infra-Red*, International Conference on Fundamental Processes in Semiconductor Nanocrystals, Santiago de Compostela, Spain, Santiago de Compostela, Spain, 2015.

114. Cao, Y. W.; Banin, U., Synthesis and Characterization of InAs/InP and InAs/CdSe Core/Shell Nanocrystals. *Angew Chem Int Ed Engl* **1999,** *38* (24), 3692-3694.

115. Yang, Y.; Chen, O.; Angerhofer, A.; Cao, Y. C., Radial-Position-Controlled Doping in CdS/ZnS Core/Shell Nanocrystals. *J. Am. Chem. Soc.* **2006,** *128*, 12428.

116. Mahler, B.; Lequeux, N.; Dubertret, B., Ligand-Controlled Polytypism of Thick-Shell CdSe/CdS Nanocrystals. *J. Am. Chem. Soc.* **2010,** *132*, 953.

117. Kumazaki, K.; Matsushima, E.; Odajima, A., Point Defects and Non-Stoichiometry in HgSe. *Phys. status solidi* **1976,** *37*, 579.

118. Jeong, K. S.; Guyot-Sionnest, P., Mid-Intraband Photoluminescence of CdS and CdSe Colloidal Quantum Dots. *ACS Nano* **2016**.

119. Guyot-Sionnest, P.; Wehrenberg, B.; Yu, D., Intraband Relaxation in CdSe Nanocrystals and the Strong Influence of the Surface Ligands. *J. Chem. Phys.* **2005,** *123*, 74709.

120. Jeong, K. S.; Guyot-Sionnest, P., Mid-Infrared Photoluminescence of CdS and CdSe Colloidal Quantum Dots. *ACS Nano* **2016,** *10* (2), 2225-2231.

121. Kovalenko, M. V.; Scheele, M.; Talapin, D. V., Colloidal Nanocrystals with Molecular Metal Chalcogenide Surface Ligands. *Science* **2009,** *324* (5933), 1417-20.

122. Nag, A.; Kovalenko, M. V.; Lee, J. S.; Liu, W. Y.; Spokoyny, B.; Talapin, D. V., Metal-free Inorganic Ligands for Colloidal Nanocrystals: S^{2-}, HS^{-}, Se^{2}-, HSe^{-}, Te^{2-}, HTe^{-}, $TeS3^{2-}$, OH^{-}, and NH^{2-} as Surface Ligands. *J. Am. Chem. Soc.* **2011,** *133*, 10612.

123. Zhang, H.; Jang, J.; Liu, W.; Talapin, D. V., Colloidal Nanocrystals with Inorganic Halide, Pseudohalide, and Halometallate Ligands. *ACS Nano* **2014**, 7359.

124. Kovalenko, M. V.; Schaller, R. D.; Jarzab, D.; Loi, M. A.; Talapin, D. V., Inorganically Functionalized PbS–CdS Colloidal Nanocrystals: Integration into Amorphous Chalcogenide Glass and Luminescent Properties. *J. Am. Chem. Soc.* **2012,** *134*, 2457.

125. Kim, D.; Kim, D. H.; Lee, J. H.; Grossman, J. C., Impact of Stoichiometry on the Electronic Structure of PbS Quantum Dots. *Phys. Rev. Lett.* **2013,** *110*, 196802.